Improving Char Combustion Models Using Micro-CT, Automated Image Analysis, and Pore-Resolving Simulations

Dongyu Liang
Marquette University

Recommended Citation

Liang, Dongyu, "Improving Char Combustion Models Using Micro-CT, Automated Image Analysis, and Pore-Resolving Simulations" (2022). *Dissertations (1934 -)*. 2035.
https://epublications.marquette.edu/dissertations_mu/2035

IMPROVING CHAR COMBUSTION MODELS USING MICRO-CT, AUTOMATED IMAGE ANALYSIS, AND PORE-RESOLVING SIMULATIONS

by
Dongyu Liang, B.E., M.S.

A Dissertation submitted to the Faculty of the Graduate School,
Marquette University,
in Partial Fulfillment of the Requirements for
the Degree of Doctor of Philosophy

Milwaukee, Wisconsin
December 2022

ABSTRACT

IMPROVING CHAR COMBUSTION MODELS USING MICRO-CT, AUTOMATED IMAGE ANALYSIS, AND PORE-RESOLVING SIMULATIONS

Dongyu Liang, B.E., M.S.

George Washington University, 2018

Combustion of pulverized coal and biomass in furnaces and boilers involves millions of particles with a distribution of sizes and morphologies. Because char particles typically react under zone II conditions, in which pore-diffusion and heterogenous reaction both influence the rate of conversion, the morphology of the porous particles affects reactor-scale outputs. To understand the impacts of complex morphology, 3-D pore-resolving simulations employing real char geometries obtained from high-resolution X-ray microtomography are first used to study combustion of 150 coal char particles and 30 biomass char particles. Localized reactant penetration into the innermost regions of the particles is observed, facilitated by the presence of large macropores connected to the external surface, resulting in non-monotonic and non-uniform reactant distributions. In contrast, temperature distributions are nearly spatially uniform throughout both the large pores and microporous char regions.

Existing analytical effectiveness factor models, which are often used as sub-models in reactor-scale simulations, are then assessed by comparison to the effectiveness factors obtained from the 3-D geometrically-faithful simulations. Conventional, frequently used uniform sphere and cylinder models significantly underpredict effectiveness factors for real coal and biomass char particles, whereas an accessible hollow cylinder model achieves good accuracy for the biomass char. Low connectivity coal char particles can be reasonably modeled using an inaccessible hollow sphere model, while combustion of coal char particles with higher connectivity can be well-represented with an accessible hollow sphere model.

To facilitate modeling large distributions of particles in reactor-scale codes, machine learning algorithms are trained to classify highly porous char particles according to their expected combustion behavior and to apply an appropriate, computationally efficient, analytical particle-scale combustion model. Whereas existing approaches have classified particles solely according to their morphology and used 2-D measurements based on particle cross-sections, the present approach classifies particles according to their *combustion behavior*, using 3-D morphology data as input and 3-D pore-resolving simulation data for classifier training. Finally, to facilitate application of the workflow to other highly porous char particles, an automated 3-D image analysis routine is developed to segment carbonaceous regions from resolved pores and to measure the morphological parameters required by the classifiers.

ACKNOWLEDGMENTS

Dongyu Liang, B.E., M.S.

Do I regret to spend years in academia as student while my friends, in my age, have already been successful in career and personal life? I am not sure. But one thing I am certain is that I have gone through a unique experience that makes me think, work, and learn independently. I am very thankful for what I have gained these years.

However, none of my achievements can be done by myself along. Many people here support me to overcome the difficulties during this special time. Therefore, I would like to sincerely thank my advisor, Prof. Simcha Singer, for the opportunity to be involved in his research projects. Without his guidance and continued support, I would not enjoy my research with clear direction and get over the tough time when I was stuck. In no particular order, I would also thank my committee members, Prof. Casey Allen, Prof. Adam Dempsey, Prof. Taly Gilat-Schmidt and Prof. Somesh Roy for their encouraging and valuable suggestions.

I appreciate the Department of Mechanical Engineering at Marquette University and National Science Foundation for their financial support. I like to thank Scott Jorgensen for spending the time in helping me get familiar with various software and fundamental knowledge when I just started. Additionally, I would like to thank Prof. Le Zhou and Prof. Dinc Erdeniz who have helped me as teaching assistant supervisors to understand the basic ideals of material science lab.

I would like to thank my parents, HuiLi Yang and Jie Liang, for their support throughout my time aboard, especially during the COVID-19 pandemic. Special thanks to my girlfriend, Yin Yang, whose emotional, instrumental, and informational support has helped me a lot. Also, I would like to thank all the Chinese restaurants in Milwaukee area for not letting me lose weight.

Finally, to my beloved grandma who had left us in 2021, sorry I was not able to come back for the last time and wish you could see my graduation.

TABLE OF CONTENTS

LIST OF TABLES

LIST OF FIGURES

Chapter 1. Introduction

1.1 Solid fuel gasification and combustion

Solid fuels like coal and biomass account for a large share of electricity generation and chemicals production. In 2020, coal accounted for 27.2% of total primary energy consumption globally, which is higher than natural gas (24.7%) and only below that of oil (31.2%)[1]. Coal utilization contributed 19.6% (844.1 TWh) of electricity generation in the United States and over 57% (7386.4 TWh) in the Asia Pacific [1]. Coal is projected to remain 23% of total energy supply until 2030 according to the prediction of World Energy Council [2]. Biomass, along with solar, wind, hydro, and geothermal, on the other hand, contributed 14.1% of the world's primary energy supply. Biomass was the third largest renewable electricity generating source, with 655 TWh of production in 2019. However, demand for biomass is growing rapidly. Electricity generated globally from biomass has increased fourfold from the year 2000 [3]. The remaining high demand for coal and the increasing demand for biomass imply that the utilization of these solid fuels should be optimized for efficiency and environmental concerns.

The most common utilization processes for solid fuels are combustion and gasification, which involve numerous chemical and physical processes. The two main steps of combustion or gasification are: 1) devolatilization (or pyrolysis for non-reactive environments), and 2) char conversion. For instance, when a pulverized coal particle reaches a temperature of 300-600 °C, light gases (volatiles) and heavier gases (tar) are released from the particle [4], and subsequently react in the gas phase. While the volatiles and tar are emitted, the carbonized residue (char) derived from the original particle forms an irregular porous solid due to the escaping gases. During this process, the structure of the particle is significantly altered [5, 6]. For entrained flow reactors, furnaces, and boilers, the entire process of devolatilization is typically completed in a few milliseconds, During char conversion, the porous solid char is converted into product gases by reacting with O_2, CO_2, H_2, etc., depending on the environment. Char gasification or combustion typically occurs within the particle, to a large degree, on the internal pore surfaces [7]. The char conversion process is slower than devolatilization, therefore modeling and experimental measurements often focus on char conversion, as it is the rate limiting step.

During gasification and combustion, carbon dioxide (a contributor to global warming) [7], particulate matter (PM2.5) [8], nitrogen oxides (NOx), sulfur dioxide (SO2) [9] and other harmful byproducts are released, resulting in environmental and health concerns. According to the world energy outlook, around 45% of CO_2 emissions worldwide due to combustion activities were from coal in 2020 [10]. Many efforts have been directed to developing more environmentally-friendly technologies for solid fuel utilization. For example, integrated gasification combined cycle (IGCC) and co-firing coal with biomass have been investigated to reduce pollutant emissions. To further design and optimize solid fuel gasification and combustion processes, a fundamental understanding of the conversion behavior is essential.

1.2 Reactor-scale CFD simulation

Many types of reactors are in use for solid fuel gasification and combustion. Gasifiers, for example, can be divided into three basic designs: fixed bed, fluidized bed, and entrained flow gasifiers. Their differences involve how the feedstock is treated and introduced, the oxidant(s) used, the operating temperatures and pressures, and the heating method [11]. The height of large-scale gasifiers is usually over 10 meters, depending on specific requirements, with the temperature and pressure are typically 1000-1500 °C [12], and from atmospheric pressure to 7 MPa, respectively [13].

Computational fluid dynamics (CFD) is helpful for optimizing and designing reactors for combustion and gasification, given the expense and difficulty of experimental data collection in such harsh environments [14] CFD makes it possible to obtain deep insights into solid fuel combustion and gasification at a variety of scales, from single particles, to groups of particles, and finally to the reactor-scale (pilot- or industrial-scale). However, the predictive capability and utility of a CFD model depends on how well the physical and chemical processes have been understood and represented.

Many reactor-scale CFD simulations have been developed to investigate different aspects of solid fuel combustion and gasification [15,16,17,18,19]. The first step is to convert the reactor into a computational domain for solution of the discretized governing conservation equations, as shown in Fig. 1-1. The grid spacing is typically *at least* one order of magnitude larger than the size of particles.

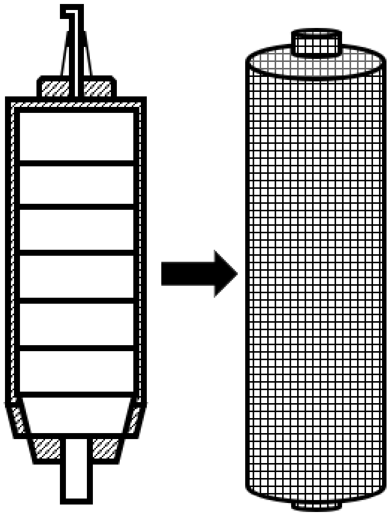

Fig. 1-1 Realistic reactor (adapted from [20] (Left)) and simplified computational reactor (adapted from [15] (Right)).

As noted above, all phenomena occurring during combustion and gasification should be well understood and considered in reactor-scale CFD simulations for accurate prediction. Therefore, the second step is coupling semi-empirical or fundamental submodels in the CFD simulation to describe the phenomena of drying, devolatilization, char conversion, and ash behavior, among others [21,22,23,24]. The quality of the submodels affects the performance of reactor-scale CFD simulations significantly. As one example, the particle drag relation has been shown to significantly impact the accuracy of numerical simulations [25,26].

1.3 Importance of particle-scale submodels

The energy and species source terms in a combustion or gasification process originate from the small solid fuel particles. Therefore, it is not surprising that the behavior and modeling of individual char particles influences outputs at the reactor-scale. This has been demonstrated in many works using modified submodels implanted in CFD simulations at reactor-scale, with experimental validation. An intrinsic-based submodel, which accounts for species transport within the particle from the surface, was coupled in a CFD gasifier simulation indicating that the kinetics submodel developed from the single particle can affect the carbon conversion at reactor-scale [16]. A set of submodels representing devolatilization, volatile combustion, char combustion and radiation have been employed in a large eddy simulation of a pilot scale furnace. It was found that the char combustion model overpredicts the char combustion rate leading to a temperature difference observed in a large-scale simulation [27]. A modified intrinsic char combustion model which accounts for particle structural parameters (diameter, density, porosity) and ash formation was developed and used in an entrained flow simulation with superior performance, indicating the importance of the particles' structure on model accuracy [15]. The shape (spherical, cylindrical, discs and slabs) and size of biomass char particles and their internal thermal gradients were also investigated and their impact on the temperature and residence time was observed to be non-negligible [28].

Fundamental particle-scale studies thus play a key role in improving reactor-scale CFD simulations. Therefore, detailed, particle-scale CFD simulations should be considered to develop the simpler, single particle models that are embedded in reactor-scale CFD simulations. The relationship between experiments and CFD simulation at different scales is shown in Fig. 1-2.

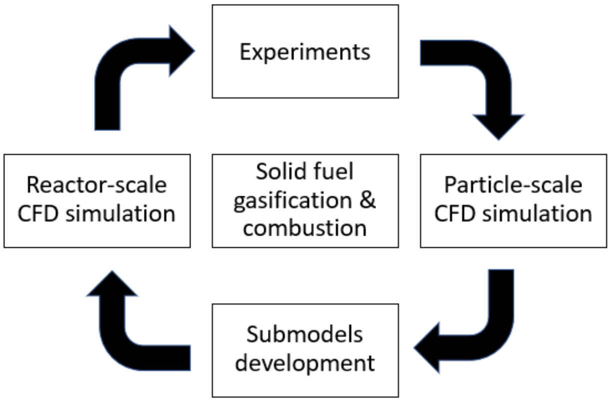

Fig. 1-2 Principal scheme of study strategy.

1.4 Types of particle-scale models

Many particle-scale models have been developed to describe the physical and chemical processes that occur during char conversion. Since solid fuel particles are porous, the models must capture diffusion of reactant gases to the particle's external surface from the bulk, diffusion of reactant gases within the porous particles, and reaction within the particles. Depending on the operating conditions, one of the steps (reaction or diffusion) may be much slower than others and becomes the rate-limiting step. Based on this, three regimes have been classified: zones I, II and III, indicating, respectively, that the conversion process is controlled by chemical reaction only, by both reaction and diffusion, and by external diffusion only [29]. More detailed information about the concept of regimes (zones) is discussed in the Chapter 2. Nonetheless, the approach of particle-scale models and their fidelity depend on the regime. Three general modeling approaches for char particle conversion are discussed next.

1.4.1 Global models

Global models lump all intra-particle processes (reaction and diffusion) into the parameters of a global reaction rate, which is considered to occur on the particle's external surface. This type of model may be predictive for zone III conditions, in which the reaction is confined to the external surface, but otherwise, this type of model is only valid when used under the same temperature and pressure conditions and particle types for which its parameters were fitted. Many such models, often together with models for boundary layer transport [30], have been developed. For example, the shrinking core model is a common model that may be accurate at high reaction rates under zone III condition [31]. However, like other global models, such as the "kinetics/diffusion fixed-core model" [32] and the "multiple surface reaction model" [33], they all consider reaction occurring on the external surface and use lumped parameters to account for the intrinsic reactivity, which requires experimental knowledge. The advantage of global models is simplicity (explicit algebraic expressions) that can be easily integrated into large-scale CFD simulations, where tens of thousands of particles need to be tracked. However, the limitation is that the lumped parameters are restricted to certain conditions.

1.4.2 Effectiveness factor models

Effectiveness factor models account for diffusion within the porous particles in a simplified manner, using an analytical solution to a simplified reaction-diffusion equation. The effectiveness factor (η), is a nondimensional number representing the ratio of the *actual* reaction rate integrated over the entire porous particle, which is limited by diffusion, to the ideal reaction rate in the absence of any diffusion limitations [34]. The effectiveness factor, η_i, modifies reaction rate *i* for the particle to account for the presence of diffusion limitations in Zone II. For a common nth order reaction rate expression [35,36,37]

$$R_i = \eta_i S k_i P_i^n \qquad (1-1)$$

$$k_i = A_{s,i} \exp\left(\frac{-E_i}{R_u T_p}\right) \qquad (1-2)$$

where R_i is the reaction rate that is modified by effectiveness factor (η_i), and is proportional to the specific internal surface area of the char particle (S), the intrinsic rate constant (k_i), and the partial pressure (P_i^n) for species i with reaction order of n. The intrinsic rate constant is expressed in Arrhenius form and depends on particle temperature (T_p), an overall activation energy (E_i), and specific pre-exponential factor ($A_{s,i}$) for species i. R_u is the gas constant.

Using the effectiveness factor, the overall reaction rate considering intraparticle diffusion can be determined using information about the reactant concentration at the particle surface. The effectiveness factor approach can also be readily integrated into reactor-scale CFD simulations. Because the reaction rate terms can be measured in lab-scale experiments, the methods to calculate effectiveness factors (which account for pore diffusion effects) become a key factor requiring specification, and effectiveness factor calculation require accuracy in parameters associated with diffusion in the porous particles. Since a portion of the present works involves effectiveness factor model evaluation, the calculation and classification of effectiveness factor models will be detailed in Chapter 2 and Chapter 4.

1.4.3 Models based on spatially resolved conservation equations

Models based on conservation equations solve partial differential equations for mass, momentum, species, and energy over the entire computational domain. Due to the complexity of the actual structure of particles with irregular pores, most conservation equation approaches have been developed as effective continuum models [38], with pore resolving models being recently developed [26]. Unlike global models and effectiveness factor models, profiles of all species and temperature distributions are available inside and outside the particle. More detailed information about these two approaches are presented in Chapter 2. Since models based on conservation equations solve multiple partial or ordinary differential equations numerically, the submodels that describe phenomena occurring within the porous particle during the gasification and combustion process can be implemented flexibly. Furthermore, this type of model can be implemented in 1-D, 2-D, or 3-D. However, this type of model is computationally expensive. Therefore, while models based on conservation equations are good for fundamental study at the particle-scale, they are impractical for incorporation into reactor-scale CFD simulations. On the other hand, this modeling approach can be used to assess simpler models that are able to be employed in reactor-scale CFD simulations.

1.5 Thesis outline

This thesis seeks to understand the impacts of realistic char particle morphologies on particle conversion for industrially-relevant zone II conditions and to provide a means to incorporate these fundamental insights into reactor-scale CFD codes. In Chapter 2, a literature review is presented for char particle combustion and gasification processes, single particle simulations, including effectiveness factor models, and approaches to characterize of char morphology. In Chapter 3, a three-dimensional, pore-resolving simulation approach based on real char particles with morphologies obtained using micro-CT will be employed to study the behavior of intraparticle diffusion and reaction for a distribution of coal and biomass char particles. The accuracy of several existing effectiveness factor models will be assessed for coal and biomass char in Chapter 4. In Chapter 5, machine learning algorithms are trained to classify particles according to their expected combustion behavior and to select accurate, computationally efficient analytical (effectiveness factor) particle-scale combustion models for *distributions* of morphologies in reactor-scale CFD. Finally, in Chapter 6, to facilitate application of the workflow to other highly porous coal chars, an automated image analysis routine is developed to filter and segment particles and to measure their morphological parameters. Conclusions are provided in Chapter 7.

Chapter 2. Background and Literature Review

Relevant background regarding char particle combustion, effectiveness factor models, spatially resolved simulation approaches, and char particle morphology characterization will be reviewed in this chapter. Based on the literature, the limitations of current approaches and the objectives of this work will be described.

2.1 Char particle combustion

2.1.1 Particle conversion process

Conversion behavior at the scale of char particles can influence reactor-scale outputs during coal combustion, such as carbon residence time, temperature, and ignition [16,27,39]. Therefore, reactor-scale CFD codes require predictive char particle submodels to accurately represent the behaviors at the reactor-scale. These submodels require fundamental knowledge of the reaction and diffusion behavior, which has not yet been examined for realistic, complex, irregular char particle structures.

There are many physical and chemical processes involved in char conversion [40], but the basic process can be summarized with the following steps, shown in Fig. 2-1:

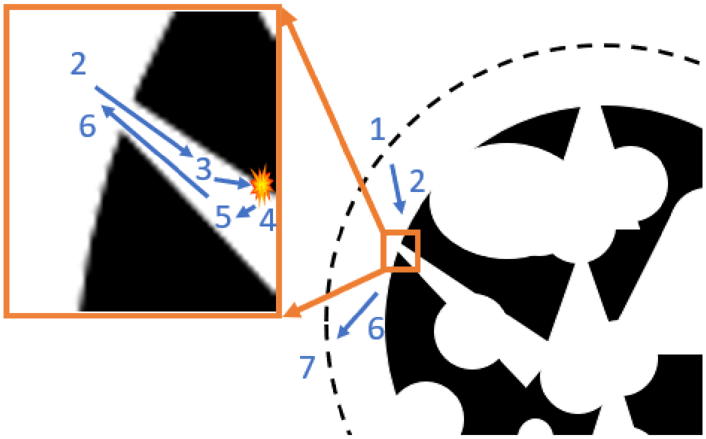

Fig. 2-1 Char particle conversion steps.

The first step is diffusion of reactant gases through the boundary layer (dash line outside of the particle) to the char particle's external surface (1-2), which is called "bulk," "external," or "film" diffusion. In the second step, reactant gases are transported, primarily via diffusion, into the porous particle ("pore diffusion", 2-3), while some of the reactant gases react with carbon at the particle external surface. However, the fraction of reactant which fails to penetrate the particle to any degree is small, due to the vastly larger surface area inside the particle's pores compared to the outer surface of the particle. In the pores, the remaining reactant gases experience absorption (3-4), chemical reaction (4) and desorption (5-6) as products. Finally, the product gases diffuse and convect from the porous particle to the surroundings (6-7). Due to the heterogeneous chemical reactions, the increased gas volume (number of moles) inside the particle causes a convective flux called "Stefan flow" away from the particle. In many cases, Stefan flow is negligible, bulk diffusion is relatively fast, and char conversion rate is controlled by pore diffusion and heterogeneous reaction [41,42]. The steps shown above indicate that char particle conversion is highly dependent on the rate of chemical reactions and the ability of the reactants species to diffuse within the particle structure.

2.1.2 Reaction regimes

As the chemical reactions and the species diffusion dominate char particle consumption, one or both of them, based on the char properties and operating conditions, can be the rate-limit factor(s) controlling the overall consumption rate, as noted in Chapter 1. Therefore, depending on which constrains the overall consumption rate, the phenomenon is often classified into three regimes (zones) [29]. The evolving density and size of char particles are also affected by the regimes [43]. Fig. 2-2 shows the distribution of reactant concentration from the surroundings to the center of a porous particle when the process is controlled by reaction, reaction and diffusion, and external diffusion, respectively. The relationship between the temperature and the reaction rate is displayed in the Fig. 2-2 as well.

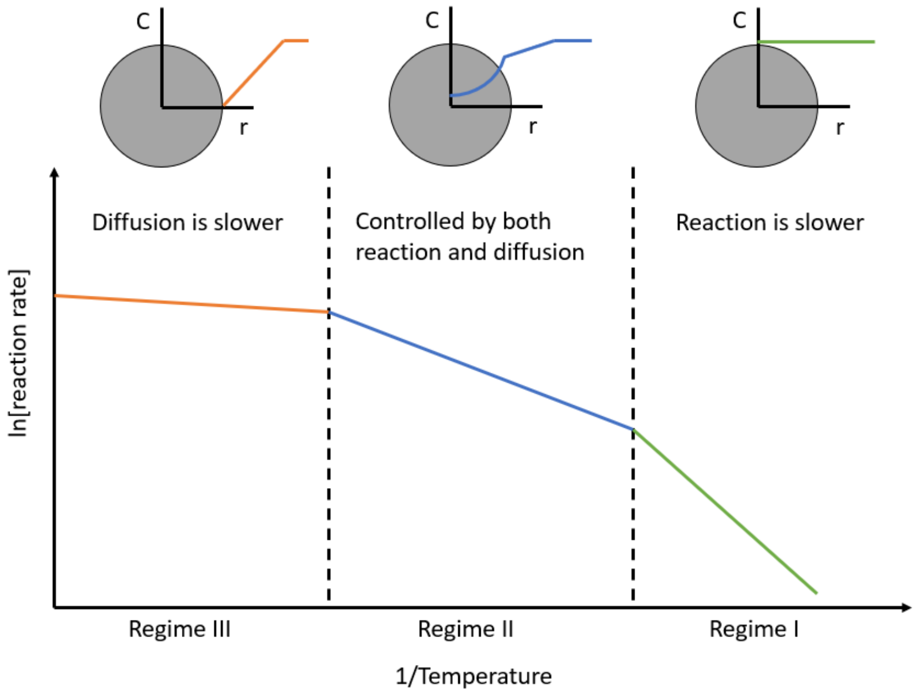

Fig. 2-2 Regimes of char conversion illustrated in the Arrhenius plot.

Regime I, also known as the chemical reaction control regime, is the regime appearing at relatively low temperatures. The overall char conversion rate is controlled by reaction since the reaction rate is much slower than diffusion. Because diffusion is relatively fast, reactant concentration is uniform (green line in Fig 2-2) since they can easily penetrate the porous particle from the external surface into the center. Thus, reaction occurs uniformly throughout the particle. The kinetic parameters (activation energy and the reaction order) measured in this regime are the true activation energy and reaction order. The particle size remains unchanged throughout conversion.

Regime II, also known as pore diffusion control regime, is the regime appearing at higher temperatures where significant reactant concentration gradients exist within the porous particle (blue line in Fig. 2-2). The timescales of diffusion through the particle and of chemical reaction are comparable under regime II. Therefore, reactant species are consumed throughout the pore structure, so concentration gradients appear. The char consumption rate is influenced by both diffusion and reaction. The effects of particle morphology must be well understood in order to predict char particle conversion behavior in this regime, since morphology significantly affects diffusion. In entrained flow gasification and combustion, char conversion usually occurs in this regime [44].

Regime III, also known as external diffusion control regime, is the regime appearing at a very high temperatures where the reaction rate is much faster than the rate of diffusion. Therefore, all reactant is consumed at the external particle surface before it can diffuse into the particle. This effect leads to a steep concentration gradient established between the particle's external surface and the surroundings (orange line in Fig. 2-2).

As discussed in the previous chapter, the development of global particle-scale models is related to the reaction regime. When the char particle conversion is controlled by kinetics (regime I), the effects of diffusion are negligible, leading to a simplified expression that can describe the conversion rate. In Regime III, the diffusion rate is slower than reaction and becomes the char conversion rate limiting factor. Since only a tiny fraction of the reactant can penetrate the particle's external surface [45] under this condition, intraparticle behaviors are unimportant, and their effects can be omitted from models. Commonly applied SCM [31], kinetics/diffusion fixed-core models [32] and multiple surface reaction models [33], may all be accurate for this situation. For regime II, in which char particles typically react for combustion and high-temperature gasification of pulverized coal and biomass [41,42,46,47], both the kinetics and transport affect the overall char conversion rate. Intra-particle diffusion and heterogeneous kinetics should both be considered for predictive modeling. The importance of char morphology should be investigated, as it significantly affects the transport process through the porous particles in industrially-relevant Regime II conditions [48].

2.2 Effectiveness factor models

The definition and role of the effectiveness factor (η_i) has been briefly explained in Chapter 1. A review of classic effectiveness factor models is performed in this section. The goal of effectiveness factor models is to consider the effects of intraparticle diffusion on the overall reaction rate and to obtain a rapid and accurate solution for the overall reaction rate. Effectiveness factor models are simple particle-scale models that can be solved analytically and are often used in reactor-scale CFD codes. Based on the definition, the effectiveness factor is:

$$\eta = \frac{R_{actual}}{R_{ideal}} \qquad (2-1)$$

where R_{actual} is the real reaction rate within the particle domain, and R_{ideal} is the ideal reaction rate when no pore diffusion limitations exist over the same domain. Thus, the effectiveness factor measures the limitations of diffusion on the overall reaction rate. Aside from implementations in gas-solid reactions, it is also (and originally) used in porous catalyst applications [49]. In zone I, the effectiveness factor equals one, indicating the porous particle is uniformly filled with reactant and the reaction rate everywhere is identical to the rate on the external surface. In zone II, as temperature increases, the effectiveness factor starts to decrease from one as the effects of pore diffusion become more important (slower) relative to the reaction. When char conversion is fully controlled by external diffusion and there is no reactant penetration, which is zone III, the effectiveness factor drops to zero since there are no species that can be transported into char particle since they react as soon as they reach the surface [50].

As outlined in Section 2.1.1, the reactant concentration distribution is determined by pore diffusion inside the particle under regime II conditions. It has been noted that the inner surface area is much larger than the external surface which is exposed to the surroundings [51], indicating that most char conversion takes place on the inner surface where more active sites can participate in reactions. This suggests the significant influence of pore diffusion process on the overall char particle conversion rate. Obviously, pore structure, which impacts the pore diffusion, is important in capturing the conversion rate. Based on the size of the pores, they are characterized as: micropores (<2 nm), mesopores (2-50 nm), and macropores (>50 nm) [52].

Diffusion of species in confined pores occurs via molecular diffusion (dominated by molecular collisions) as well as Knudsen diffusion (dominated by collisions between gas molecules and the pore walls) which becomes more important for smaller pore sizes (micropores and mesopores). Therefore, the effects of the pore diffusion (molecular and Knudsen) should be considered while calculating effectiveness factor. The calculations of molecular diffusion, Knudsen diffusion within small pores, and their effective pore diffusion are provided in [53,54]and will be briefly described here and detailed in Chapter 3. Moreover, during combustion and gasification, carbon is consumed on the pore walls within the particle, leading to a change of the pore structure and internal surface area. The altered pore structure causes the evolution of the internal pore surface which changes the amount of surface area available for reactions. For internal pore surface evolution, many models, such as grain models (different sizes of non-porous sub-sphere) [55], random pore models (pores with random sizes and orientation, most widely used) [56], and average pore size models (pores with the same length and diameter) [57], have been developed.

2.2.1 Conventional analytical effectiveness factor models

Simple analytical and semi-analytical models have been developed to calculate effectiveness factors. Effectiveness factor models are based on solving a steady, one-dimensional reaction diffusion problem with appropriate boundary conditions, with simplifications, such as a single gas species and isothermal particles. The diffusion equation with reaction, in spherical coordinates (the most common used form), can be written as:

$$D_{eff}\left(\frac{\mathrm{d}^2 c}{\mathrm{d}R^2}+\frac{2}{R}\frac{\mathrm{d}c}{\mathrm{d}R}\right)-Skc=0 \qquad (2-2)$$

Where D_{eff} $(\frac{m^2}{s})$ is the effective diffusivity, c $(\frac{mol}{m^3})$ is the species concentration, R (m) is the particle radius, S $(\frac{m_2}{m_3})$ is specific internal surface area per unit volume, and k $(\frac{1}{s})$ is the rate constant. Based on the reaction-diffusion equation, a nondimensional number, the Thiele modulus (ϕ_i), has been introduced to describe the ratio of the chemical reaction rate to the rate of mass transport (diffusion) within the porous particle [58] (similar to a Damkohler number). Its original form is expressed as:

$$\phi=R\sqrt{\frac{Sk}{D_{eff}}} \qquad (2-3)$$

When chemical reaction is slower than diffusion, the Thiele modulus is smaller than one, while the Thiele modulus is larger than one when the diffusion rate is slower than the chemical reaction rate. For a uniform solid sphere, the effectiveness factor can be expressed in terms of the Thiele modulus:

$$\eta_i = \frac{3}{\phi_i}\left(\frac{1}{\tanh(\phi_i)} - \frac{1}{\phi_i}\right) \qquad (2-4)$$

This basic effectiveness factor approach is still widely applied in both coal and biomass research [15,59,60,61,62].

The mixture-averaged effective diffusivity for species i in a porous medium can be obtained by a simple approximation that considers the effects of both molecular diffusion and Knudsen diffusion [50]:

$$D_{eff,i} = \frac{\theta}{\tau}\left(\frac{1}{D_{knud,i}} + \frac{1}{D_{m,i}}\right) \qquad (2-5)$$

where θ and τ are particle porosity and tortuosity of the pores, $D_{knud,i}$ is the Knudsen diffusion coefficient given by [54], and $D_{m,i}$ is the molecular diffusion coefficient for species i. Knudsen diffusion occurs when the scale length of a system is comparable to or smaller than the mean free path of the species particle [63] within the solid char particle.

However, it has been demonstrated experimentally that it is incorrect to employ a spherical model for many realistic coal char particles with that have high porosity and thin walls [64,48]. It has been suggested that these common particle geometries should be treated as flat plates instead of spheres, due to the small diffusion length and small local curvature due to the thin walls and high internal void porosity. Thus, some researchers

[65,66,67] have used the classical effectiveness factor expression for flat plate geometries, with the Thiele modulus defined as:

$$\phi = \frac{l}{2}\sqrt{\frac{Sk}{D_{eff}}} \qquad (2-6)$$

where l is the measured wall thickness of char particle. In some applications, the effective thickness is calculated by $V_{mps}/S_{mps,interface}$, where V_{mps} is the micropore solid volume and $S_{mps,interface}$ is the total surface area of solid particle. Then, the effectiveness factor is calculated as:

$$\eta_i = \frac{\tanh \phi_i}{\phi_i} \qquad (2-7)$$

The assumption of a uniformly porous spherical and flat plate models for char particles, used in the classical approach, is insufficient for real char particles that often have highly non-uniform morphologies [64] (See Section 2.4). For coal char, while the hollow sphere approach (discussed in Chapter 4) is better for some cases, and models based on cylinders (such as the uniform finite cylinder (UFC) and uniform infinite cylinder (UIC) models, etc.) have been used for biomass. Other more complex effectiveness factor approaches, such as 1D–GC and 1D–GV models [68,69] and Pellet-Particle Model [70], also face difficulties due to simplifying assumptions and/or the complexity of real particle structures. In other words, existing analytical models may agree well with certain particle types, but their performance need to be investigated for a *distribution* of particles with different structures. So far, no research has evaluated the performance of effectiveness factor models using geometrically-faithful 3-D solutions for real char particles. The 3-D, pore-resolving simulation approach is well-suited to carry out such an evaluation. The performance of effectiveness factor models suitable for use in reactor-scale CFD codes (not only the uniform sphere and flat plates model, but also the models described above) is examined in Chapter 4.

2.3 Partial differential equation-based simulation approaches

2.3.1 Spatially resolved effective continuum models

In contrast to the analytical effectiveness factor models, which are based on several simplifications of the physics (e.g., single gas species, isothermal particles), it is possible to solve conservation equations for a reacting char particle using numerical methods. This type of partial differential equation-based model is used for fundamental investigation because it is too expensive for particle-scale submodels in reactor-scale CFD codes. Since real char particles contain a wide variety of pores with different sizes (see Section 2.1.2), conservation equations based on first principle are impossible to solve for the actual pore space. Therefore, for simplification, an effective continuum model based on the “upscaled” (volume-averaged) conservation equations [38,71], is widely employed in porous char simulations. The pore structure and internal surface area of the pores are modeled at the sub-grid-scale [72,73,74]. Upscaling transforms conservation equations for the actual pore space into “effective-continuum” conservation equations for smoothly varying variables. The validity of the effective-continuum approach requires a separation of length scales; the upscaling must be performed over representative volume elements that are large enough to contain a statistical number of heterogeneities (pores), but small enough to resolve particle-scale gradients, such as temperature and concentration gradients [75]. This implies that the characteristic size of the pores is much smaller than: (a) the size of the particle itself, and (b) the characteristic length of the physical processes to be resolved [76,77]. Valid and invalid situations for an effective-continuum approach are illustrated in Fig 2-3.

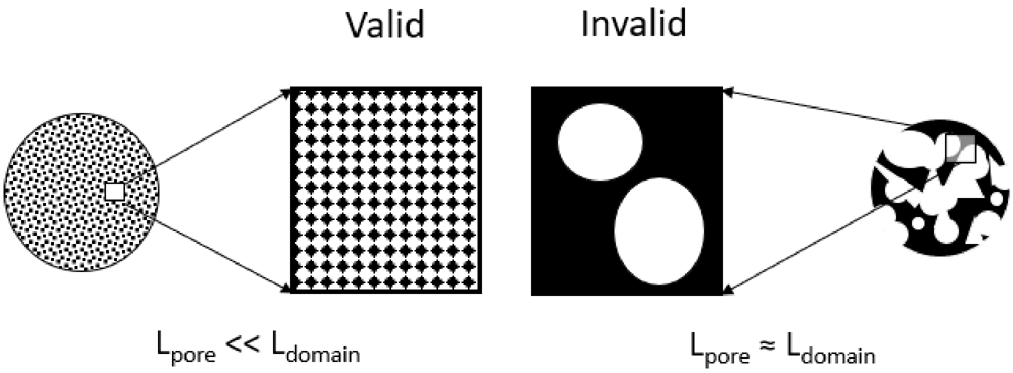

Fig. 2-3 Length constrains for “upscaled” method.

Char particles produced from many coals and biomass feedstock contain a range of pore sizes, including large macro-pores that can approach the size of the particles themselves. Therefore, the length-scale constraints for upscaling are often violated [76,78]. A typical coal char particle cross-section obtained from high-resolution micro-CT is shown in Figure 2-4, with the solid microporous char in red, and the large macropores and voids, which clearly violate the conditions for upscaling, shown in blue.

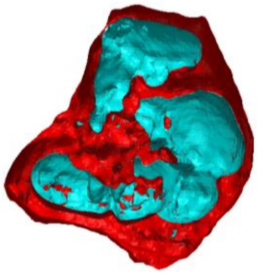

Fig. 2-4 A 3-D char particle morphology and macro-pore structure obtained from micro-CT.

Nonetheless, most char consumption models assume, explicitly or implicitly, that particles are amenable to treatment as volume-averaged spheres or cylinders, with smoothly varying effective properties and sub-grid-scale porosity. This is the case for stand-alone, spatially resolved models that examine the impacts of reaction, advection, and diffusion on density/diameter evolution [59,79,80], including those that explicitly attempt to account for the presence of large pores [81], as well as effectiveness factor models used in reactor-scale CFD codes. However, the application of effective-continuum models in the absence of scale separation can lead to inaccurate predictions of heterogeneous reactions [82], mixing [83] and hotspots [84] . Experiments have demonstrated that real char particles cannot be accurately modeled as homogeneous, porous spheres [64] and that char morphology has a strong impact on conversion for zone II conditions [64,43] .

2.3.2 Spatially resolved pore resolving models

Because the constraints for upscaling are often violated, effective continuum models fail to predict the true behaviors of char particle combustion. Some studies have used discrete networks to model char consumption [85,86,87,88] instead of using upscaling method, but the ability of such networks to emulate real char morphology is unconfirmed and the approach is difficult to combine with other physics. Others have modeled reaction and transport in char particles using resolved, but idealized, pores, which are called pore resolving models. For instance, a few simple idealized pores were created in form of short gaps, long gaps, rings, and layers respectively within the solid spherical particles. The temperature distribution through the particles and Stefan flow effects were investigated and compared with the pure solid spherical particle [26]. More complicatedly, an agglomerate of 185 smaller monodisperse non-porous spheres comprising a larger sphere has been used for modeling oxy-combustion of a porous coal char particle [89]. The details of the particle conversion process within the idealized resolve pores was studied under the changed regime conditions and the flow velocity. Similar research focusing on single particle oxy-combustion simulation was performed using idealized, resolved cone-shaped pores to understand the effect of particle size and porosity on coal char conversion [90]. The monodisperse/polydisperse pores cut from a 3-D volume of spherical particles forming a packed-bed structure was numerically obtained to examine the impact of different pore size distributions on the particle carbon conversion rate [91,92]. Human-made catalyst particles, which often contain geometrically regular pores, are more amenable to treatments using idealized, resolved pores. For instance, reaction and transport in porous catalyst particles were studied using resolved cylindrical holes while the surrounding grains were treated as an effective continuum [93,94]. Moreover, pore resolving models can be employed for biomass as well. An idealized 3-D structure of biomass particles with morphological parameters based on confocal scanning laser microscopy was developed for non-reacting simulations of heat and mass transfer [95]. Some idealized resolved pore structures used in the mentioned pore resolved simulations are shown in Fig. 2-5.

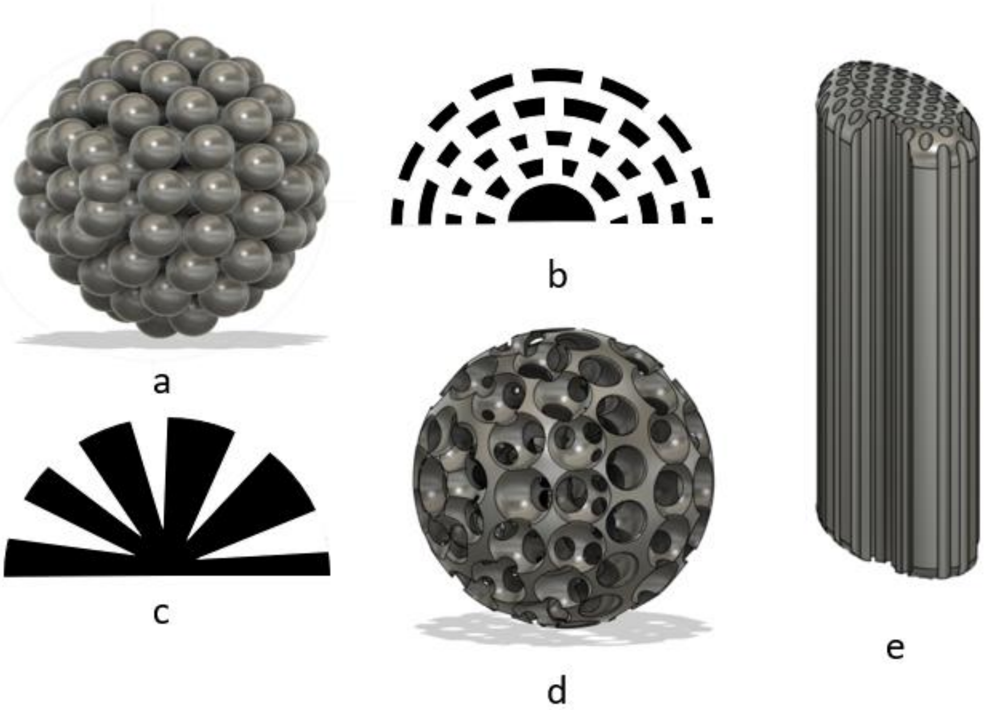

Fig. 2-5 Pore resolved geometries of (a) agglomerate of smaller non-porous spheres [89], (b) layers [26], (c) cone-shaped pores [90], (d) monodisperse pores [91], and (e) biomass particle [95].

However, the cited studies are not the most accurate in the sense that real porous structures have not been employed in the particle-scale simulations [96]. To capture the impact of realistic and actual particle morphology, the first realistic, pore-resolving, reacting flow simulation for char particle conversion was developed [44]. The simulation was compared to an effective-continuum simulation of a spherical char particle with identical initial mass, volume, porosity, surface area and equivalent diameter. The oxygen penetration and rates of conversion differed significantly between the two models before the gasification transitioned from zone II to zone I conditions.

This thesis extends this approach to study a *distribution* of particle morphologies, since only a few coal char particles were examined in the previous work and uses the approach to assess and implement effectiveness factor models. This model and its application will be discussed in Chapter 3. Briefly, the real, irregular resolved pore structures, which often violate the length-scale constraints for upscaling are resolved using micro-CT. After meshing the real particle geometry, conservation equations based on the first principles are solved in the large, resolved pores (blue areas in Fig. 2-4), and effective continuum equations are applied only to the surrounding microporous grains (red areas in Fig. 2-4), where volume averaging is appropriate because the pores are very small and numerous.

2.4 Characterizing char morphology

2.4.1 Conventional image analysis and limitations

Characterizing char morphology enables a better understanding of the conversion behavior during combustion and gasification. In regime II, the morphology of the "large macropores" (of similar order of magnitude as the particle length-scale) can sometimes play a more influential role in particle burnout than intrinsic kinetics [97]. Therefore, the effects of the char morphology should be considered in conversion models to improve their predictive capabilities. Optical microscopy and scanning electron microscopy (SEM) are typically used for char particle morphology assessment [98,99]. These techniques disperse a distribution of particles in epoxy resin, which is hardened and sliced to obtain cross-sections. The two-dimensional (2-D) cross-sections provide for observation of the "large macropores" within the char particles (any pores that are smaller than the image resolution will be lumped into the solid material) allowing the measurement of volume of pores, wall-thickness, swelling degree, unfused material, size and shape of particles, and can be used for carbon conversion models [100,101,102,103,104,105]. Resolved pore porosity is estimated for each particle in the sample by calculating the fraction of its area occupied by visible pores to its total cross-sectional area. Wall thickness is determined for each particle by using measurement lines extending from the center of a single cross section of the particle image.

Nevertheless, as pointed out in [103], methods based on 2-D cross-sections lack accuracy due to the complex, 3-D structures of real particles. For instance, the estimation of macro-porosity based on cross-sectional particle area assumes the ratio of macropore volume to particle volume equals the ratio of macropore area to particle area for the cross-sectional image. For the three-dimensional char particle, this assumption is only valid when the particle is perfectly symmetric and the cross-sectional image passes through the center of the particle. Apparently, this assumption would fail all the time since the realistic char particle is, in general, highly asymmetric due to the irregular geometry. Moreover, it is unlikely that the cross-sectional image would exactly cross the center of the particle while preparing sliced samples in the epoxy resin.

Two masked cross-sectional images from the same particle, but with different orientations, are illustrated in Fig. 2-5. The microporous solid regions are in red, and the resolved pores are in blue.

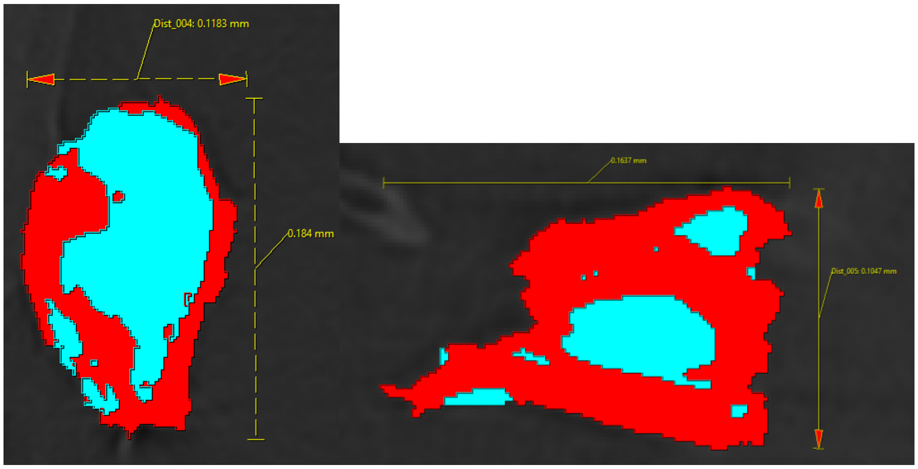

Fig. 2-6 The same char particle shown in two different orientations.

The cross section on the left of Figure 2-6 exhibits a thinner wall thickness and a higher porosity than the cross section on the right. Realistic char particles with non-uniform macropores and asymmetric geometry clearly cannot be characterized based on single cross section method. It results in a high variability of macro-porosity measurements. Therefore, the morphological properties measured by the existing 2-D methods with simplifying assumptions cause a potential accuracy issue and *biased results* for a particle distribution (discussed in Chapter 6) for char particle characterization and introduces error into the char particle conversion models that rely on a proper distribution of morphological parameters. Although automated techniques have recently been developed to efficiently quantify morphological properties for char particle distributions [106,107], such measurements are still based on 2-D cross sections and only accurate when the char particle is symmetric at the measured section.

2.4.2 Char particle classification

In order to consider the effects of the char particle morphology in char conversion models, a classification methodology is necessary for a distribution of particles. For coal char particles, a complex particle classification system was developed by [108] that divided coal char particles into 11 categories: tenuisphere, crassisphere, tenuinetwork, mesosphere, fragment, inertoid, solid, fusinoid, mixed porous, mixed dense, and mineroid, that were mainly classified by the pore volume and wall thickness obtained from microscopy analysis. Similarly, the International Committee for Coal and Organic Petrology (ICCP) has defined nine coal char types [109], including tenuisphere, crassisphere, tenuinetwork, crassinetwork, mixed porous, mixed dense, inertoid, fusinoid/solid and mineroid. The strategy of the classification system is based on the amount of unfused material, wall thickness and porosity. Examples of particle geometries of the typical complex classification system are illustrated in Figure 2-7.

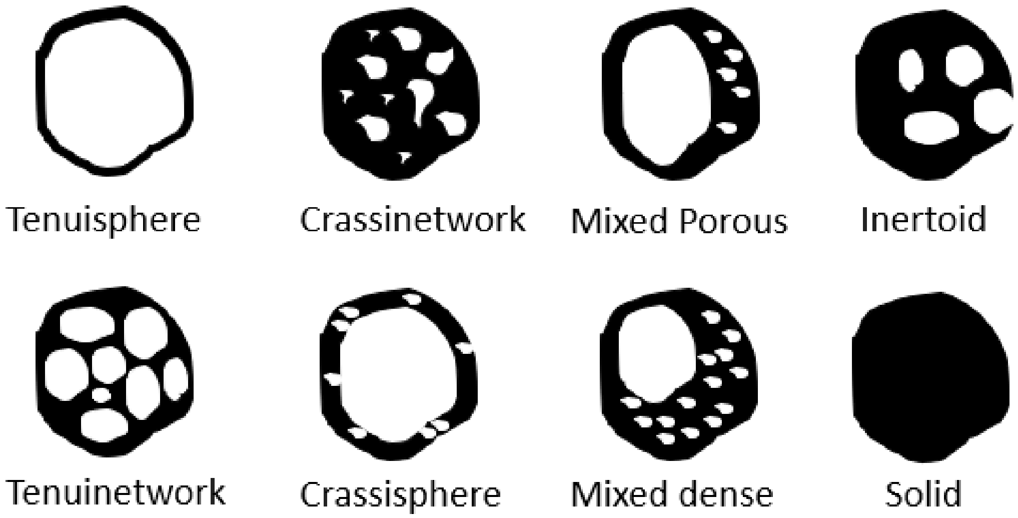

Fig. 2-7 Structures of typical char particle in complex classification (Adapted from [102]).

In many works [64,48,101,102,103] that rely on the classified char particle morphologies to improve the char particle conversion models, three coarse coal char morphologies are often used for pulverized particles (~100 μm): cenospheres, solid, and mixed porous-solid structures [110], as shown in Figure 2-8.

Fig. 2-8 Structures of typical char particle in simplified classification (adapted from [110]).

The censopherical-type particles have high macropore volume leading to a highporosity (> 60%) and swelling ratio (> 1.3), and thin wall (< 5 μm). Solid-type of particles have low porosity (< 40%), low swelling ratio (< 0.9), and thick walls (> 5 μm). Mixed porous-solid type particles have intermediate characteristics.

Biomass char morphology depends on the fuel’s cellulose, hemicellulose, and lignin content, cell wall characteristics, and devolatilization conditions, such as the heating rate [111,112]. Irregular void structures, cenospheres, and dense chars have been observed [111–114], as well as features not typical of coal char, such as high aspect ratios, large cellular structures, and anisotropic pores [95,112,115]. A classification system has been developed based on aspect ratio, wall thickness and porosity [113] with a similar method based on 2-D cross-sectional images.

However, the existing classification systems for both coal and biomass have classified particles solely according to their morphology and used 2-D measurements based on particle cross-sections. A new classification system is therefore needed to select an accurate, computationally efficient 1-D particle-scale combustion model *based on combustion behavior* for a distribution of morphologies.

As discussed previously, the char particle conversion process is usually analyzed with the simplified particle shapes (sphere, cylinder etc.). However, the shape and morphology of char particles vary from particle-to-particle in the large distribution of particles in a reactor. The calculation of effectiveness factors for every particle tracked in reactor-scale CFD using a single model structure would likely be inaccurate.

2.5 Conclusions

As discussed in this chapter, the overall goal of this thesis is to improve the accuracy of reactor-scale CFD codes by improving particle-scale models for char particle combustion. However, models based on idealized particle geometries are insufficient to capture the phenomena occurring in the real char particle during combustion. To overcome these shortcomings, pore-resolving simulations for a distribution of particles will be used to generate fundamental knowledge about reaction and diffusion in real particles imaged with micro-CT. These will be used to assess and propose simple effectiveness factor models utilizing a strategy that can be integrated in reactor-scale CFD codes for an array of char particle types. A better representation of distributions of real particle morphologies can be then used in the reactor-scale CFD simulation, thus improving their predictive capabilities.

2.5.1 Research objectives

2.5.1.1 Objective 1: Analyze the interplay of reaction and diffusion in a population of real coal and biomass char particles using pore-resolving, micro-CT-based combustion simulations.

Due to the shortcomings that effective continuum models have with (a) upscaling constraints being violated by large macropores and resolved pores, and (b) the inapplicability of perfectly spherical particle structures, a pore-resolving approach is needed for accurate analysis. This work, therefore, aims to use a new char conversion simulation based on real particle geometries obtained with micro-CT to study the fundamentals of char particle combustion for many small coal and biomass char particles. The pore-resolving model will be used to draw conclusions about the effects of real char morphology, and to quantify the impacts of morphological parameters, on the coupling of reaction and diffusion during combustion.

2.5.1.2 Objective 2: Analyze, recommend, and develop effectiveness factor models that can be applied to a range of real particle geometries.

Many effectiveness factor models have been developed using a variety of simplifications and can yield good predictions in certain cases. However, the applicability to real char particles is unknown. Therefore, the pore-resolving simulation tool provides an opportunity to evaluate existing effectiveness factor models' performance by comparing the results with those of the CFD simulation of real particles. To set up a comparable evaluation method between these models, morphological properties of the char particles, and kinetic, transport and thermodynamic parameters should be consistent between the analytical and 3-D models.

2.5.1.3 Objective 3: Develop an automated 3-D image analysis tool and classification tool to quantify particle morphology and apply an accurate effectiveness factor model for every particle in a distribution.

The morphology of char particles, such as porosity, surface area and effective wall thickness, can have a significant influence on the overall char conversion process. Furthermore, those morphological parameters can be used to classify the char particles and assign appropriate effectiveness factor model ("appropriateness is to be determined based on comparison with 3-D simulations). However, 3-D image analysis requires manual segmentation by processing scanned images, selecting thresholding values, segmenting the solid particle area from the background, etc. The process is time consuming and cannot be easily integrated into our proposed workflow of characterizing char particle distributions in 3-D and assigning a distribution of effectiveness factor models (based on the knowledge obtained from our pore-resolving simulations). Therefore, for the purpose of conveniently and quickly characterizing particle geometries for a distribution of particles, an automated 3-D image analysis tool for micro-CT data will be developed for a distribution of particles. Compared to current 2-D techniques for measuring char particle geometry, an automated image analysis based on real, 3-D particle structures is more accurate and faster. This aim will be integrated with machine learning (ML) algorithms that use the quantified morphological parameters to classify particles by suitable effectiveness factor models. Using the automated image analysis and classification workflow, reactor-scale CFD codes can account for a realistic distribution of char particle morphologies with a corresponding distribution in combustion models.

Chapter 3. Conversion Behaviors in a Population of Real Coal and Biomass Char Particles Using Pore-Resolving, Micro-CT-Based Combustion Simulations

This chapter will discuss the effects of porous char particle (both coal and pine biomass) morphology on its combustion using pore-resolving simulations based on real 3-D particle structures obtained from high-resolution micro-CT. “Morphology” refers to geometrical features and large pores (> a few microns) which affect gas diffusion throughout the particle. A distribution of coal and biomass char particles will be examined with the 3-D pore-resolving model. The impacts of char morphology on the reaction-diffusion interplay will be studied.

In Section 3.1, background information regarding micro-CT and its utilization in coal and biomass research are briefly reviewed. Fundamental assumptions, governing equations and the computational approach for the micro-CT based, pore-resolving simulation are presented in Section 3.2. A comparison between transient and steady simulations, and a mesh convergence study is presented in Section 3.2, as well. The impacts of morphological parameters like the distribution of porosity and external void fraction, on temperature and oxygen fraction profiles within the particles is discussed in Section 3.3 for coal and biomass particles.

3.1 Introduction

As discussed in the last chapter, many idealized pore resolving models have been used by other researchers to address the deficiencies associated with effective-continuum models due to the presence of large macropores in sub-millimeter char particles. Their insufficiencies have been demonstrated as well. In this thesis, the alternate approach to modeling reaction and transport in disordered porous char while respecting the length-scale constraints is to experimentally obtain the real particle morphology in three dimensions (3-D) and to perform pore-resolving simulations.

X-ray computed tomography (CT) is an attractive technique for obtaining the internal and external geometry of disordered porous media due to its non-destructive nature, acquisition speed, high resolution, and convenience. With the development of computer technology, applications utilizing X-ray CT have increased (mineralogy, cleaning, pyrolysis, combustion and gasification, and carbon dioxide sequestration) related to coal and biomass research. The number of published journal articles applying X-ray CT for coal-related studies increased around six times over the last 20 years [116]. It is likely that this technology will become more common in the future for biomass fuel characterization.

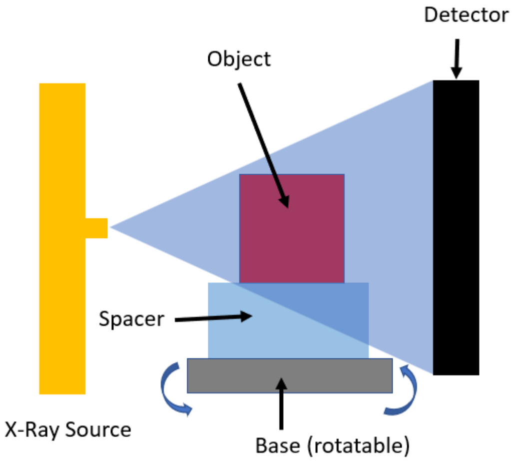

Fig. 3-1 Example of X-ray CT principle (adapted from [117]).

The basic principle of X-ray CT is illustrated in Fig. 3-1. X-rays are a form of electromagnetic radiation that contains much higher energy than visible light. This intensive energy is usually generated by using focused electron beam that bombards a target that consists of high-density object to release high energy photons that form X-rays. The electron beam, as the key to create those photons, is produced by the “excitation” voltage (usually in keV) to accelerate electrons excited from a filament cathode and concentrated onto a metallic cathode. The “bremsstrahlung” radiation consists of X-rays emitted with the photon energy. And it equals to the input voltage, due to the interaction of the high-density cathode and activated electrons [116]. X-rays released from the source pass through the object that is placed on the rotatable base. (The high energy photons can penetrate through most objects.) With increased penetration depth, the intensity of the X-rays is reduced, causing a different attenuation, that can be captured by the detector to form a 2-D X-ray image showing different levels of greyscale. For instance, the organ tissue has a lower attenuation than the bone when the X-rays passing through. Instead of 2-D X-ray image based on fixed angle, a rotatable base provides views along various angles to generate a series of images of the object. A full 3-D structure (external and internal) of the object can then be mathematically reconstructed. X-ray CT technology is widely used and has been applied in solid fuel analysis (3-D petrography and mineralogy [118], drying [119], swelling [120], carbon dioxide sequestration [121]).

X-ray micro-computed tomography (or “micro-CT,” which is X-ray CT with a resolution lower than 15 μm) has been used to image the internal and external structure of sub-millimeter char particles in three dimensions (3-D) and can help elucidate the impact of real morphology during char combustion of pulverized char [122,115]. Micro-CT (135 µm voxels) was recently used to image the evolution of solid density and gas temperature in large (~19 mm), smoldering biomass particles in-situ, and revealed the importance of biomass structure (e.g., cracks) on char oxidation [123]. A subsequent study found that pore orientation affected volatile transport, while char oxidation was largely confined to the edges of 16 mm particles [124]. Micro-CT (2 µm voxels) was also used in conjunction with zone II experiments to qualitatively examine the impact of anisotropy, pore morphology, and gas transport on the evolution of cylindrical wood char particles (2 mm) [115]. For cylindrical biomass char with large pores (>5 µm) oriented along the particle axis, gasification likewise occurred primarily in the axial direction rather than in the radial direction. For coal, non-reacting simulations of transport in coal macropores and resolved pores larger than 13.85 µm based on geometries obtained from micro-CT [125] have been reported. Micro-CT has also been used to generate geometries for 3-D, pore resolving CFD simulations to examine the impacts of real char morphology during gasification [44]and combustion [122]. Moreover, pulverized char particle morphology has been quantified (porosity and wall thickness) in three dimensions by applying micro-CT images [100].

By taking advantages of micro-CT, the first realistic, pore-resolving, reacting flow simulation for char particle conversion was developed [44] to address the violation of the length-scale constraints by effective-continuum models. An 850 µm coal char particle was imaged in three dimensions using micro-CT (voxel size 20 µm). The particle was then isotropically scaled to 100 µm to represent pulverized char and was meshed and exported for CFD simulation under entrained flow gasification conditions. Conservation equations based on first principles were applied within the resolved large pores, which could not be included in the effective-continuum due to their violation of the length-scale constraints for upscaling. For the regions of “microporous” char that surround the resolve pores, effective-continuum equations were employed, since they contain smaller pores amenable to upscaling. The simulation was compared to an effective-continuum simulation of a spherical char particle with identical initial mass, volume, porosity, surface area and equivalent diameter. The oxygen penetration and rates of conversion differed significantly between the two models before the gasification transitioned from zone II to zone I conditions [44].

In this chapter, the micro-CT-based, pore-resolving simulation approach is extended to a distribution of particles, with smaller sizes (~100 µm), reacting in a combustion environment. Pore-resolving simulations are used to study a population of 150 pulverized, bituminous coal char particles and 30 biomass char particles formed at a high heating rate, whose 3-D internal and external geometries have been obtained from high resolution micro-CT. The simulations are used to assess (in later chapters) the fidelity of existing one-dimensional effectiveness factor models, which are often used as particle-scale models in reactor-scale CFD codes.

3.2 Micro-CT-based pore-resolving simulations

3.2.1 Char production

3.2.1.1 Coal char

Bituminous coal particles (Illinois #6) were sieved to a 100 µm nominal diameter. The coal contained 46.61% fixed carbon, 40.34% volatile matter and 13.05% ash on a dry basis, and was composed of 67.48% carbon, 4.82% hydrogen, 8.60% oxygen, 1.53% nitrogen and 4.52% sulfur. The particles were scattered in a single layer on a sheet of aluminum foil, covered with a glass beaker, filled with argon, and sealed. The inverted beaker was then placed in a pre-heated, 800°C muffle oven for 30 seconds, resulting in a maximum initial heating rate estimated to exceed 1000 K/s.

3.2.1.2 Biomass char

Pine sawdust from a woodworking facility (Larrabee, Iowa) was sieved to a 100 µm nominal diameter. Biomass particles were dispersed in a single layer on a sheet of aluminum foil, covered with a beaker, purged with nitrogen, and sealed. To produce char at a high heating rate, the inverted beaker was placed in a pre-heated muffle oven at 800°C for 30s.

3.2.2 Micro-CT imaging and image processing

3.2.2.1 Coal char

Dozens of coal char particles were attached to a micro-pipette tip and imaged using a GE v|tome|x s 240 X-ray micro-CT scanner operating at 80 kV and 130 µA, with a voxel size of 1.632 µm. The stack of reconstructed TIFF images was then imported into ScanIP (Synopsys, Mountain View, USA) software for processing, segmentation, and meshing. Individual particles were segmented from one another and from the pipette support material. A recursive Gaussian filter was initially applied to the greyscale images of the individual particles, which were then segmented into what is termed the “microporous solid” and “resolved voids/pores” using manual grey-scale thresholding. The microporous solid region is comprised of unresolved micropores, mesopores and macropores, as well as carbonaceous char. The distribution of particles was comprised of cenospheres (particles with a large central resolved pores) and network-type particles with a more complex pore structure [109]. Most of the cenospheres could be classified as thick-walled crassispheres rather than thin-walled tenuispheres. Three dimensional renderings of a cenospherical particle, a transitional particle, and a more complex particle structure, after filtering and segmentation, are shown in Fig. 3-2, indicating the resolved pores and the microporous char.

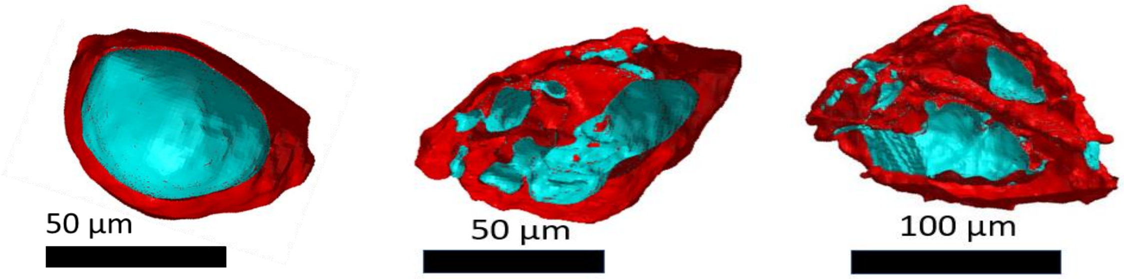

Fig. 3-2 Three-dimensional rendering of three char particles, with the resolved pores shown in blue and the microporous solid in red for cenosphere (left), transitional (middle), and network (right) particle.

3.2.2.2 Biomass char

Like the coal char, dozens of biomass char particles were imaged simultaneously using a high-resolution micro-CT (GE v|tome|x s 240) operating at 60 kV and 190 μA, with a voxel size of 2.00 μm. Following reconstruction, the TIFF stack was imported into ScanIP. Thirty particles were separated and segmented from one another and from the support. For each particle, a recursive Gaussian filter was applied, and grey-scale thresholding was used to segment the resolved "large pores" from the "microporous char" which was comprised of carbonaceous solid and unresolved porosity, as shown in Fig 3-3.

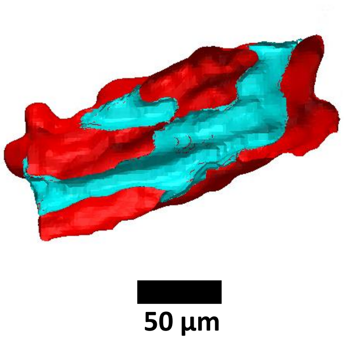

Fig. 3-3 Three-dimensional rendering of representative biomass char particles, with the resolved pores shown in blue and the microporous solid in red.

3.2.3 Pore-resolving CFD simulation

3.2.3.1 Coal char

To focus on the impacts of particle morphology on the reaction-transport balance, the effective particle diameter and the total particle volume were made identical for every particle by using the isotropic scaling factor

$$R_{scale} = \frac{\left(\frac{6}{\pi}\left(V_{mps}+V_{voids}\right)\right)^{\frac{1}{3}}}{100\ \mu\mathrm{m}} \qquad (3-1)$$

where V_{mps} is the volume of microporous solid and V_{voids} is the volume of the resolved pores, which were calculated using volume integration of the 3-D geometries obtained from micro-CT imaging (see Appendix for measured data), because most pulverized particles were approximately 100 µm in diameter prior to devolatilization, the scale factors ranged only between 0.663 and 1.411.

The unresolved porosity of the sub-grid-scale microporous solid regions, θ_{mps}, was set to 25.6% for all particles. All transport and thermodynamic parameters and all kinetic parameters, including the sub-grid-scale surface area per unit volume of the microporous solid regions, S (3.79 x 10^7 m^2_C/m^3), were identical for every particle in the distribution. Although these sub-grid-scale parameters are not based on experimental data for this coal char, they are typical for coal char and most importantly, are consistent from particle to particle, allowing for an evaluation of the impacts of the large pore morphology. The resolved pore volume, V_{voids}, and the microporous solid volume, V_{mps}, differed between the particles, as did the spatial distribution and morphology of the resolved pores. The resolved porosity of the particles, θ, ranged from 11.9% to 60.3%.

The particles were individually placed at the center of a spherical domain with a diameter of 1000 µm. Far-field boundary conditions of 1373 K, and mole fractions of 12% O_2, 10% H_2O, 74% CO_2, and 4% CO are based on the pre-flame region of a 100 kWth pilot scale furnace [126]. No relative velocity was imposed, as the small particles are treated as entrained in the surrounding flow. However, the velocity at the boundary was free to adjust itself according to Stefan flow effects, which resulted in a net flux away from the particles.

Figure 3-4 shows a cross-section of part of a computational domain. In the resolved pores (blue regions of Fig. 3-4), as well as in the gas-phase boundary layer surrounding, the porous particle (green region of Fig. 3-4), standard gas-phase conservation equations for mass, momentum, species, and thermal energy were employed (See Section 3.2.3.3). In this way, large heterogeneities (pores) which are not amenable to upscaling were treated in a mathematically valid manner [44]. Because the microporous char (red regions of Fig. 3-4) contains sub-grid-scale, sub-micron pores that are amenable to upscaling, effective-continuum conservation equations for mass, momentum, species, and thermal energy were employed in these regions to account for the presence of both gas and solid phases (see Section 3.2.3.3). All heterogeneous reactions occur on the unresolved surface area, *S*, of the microporous solid regions, because the total resolved interfacial area was at least two and half *orders of magnitude* smaller than the unresolved surface area of the microporous solid.

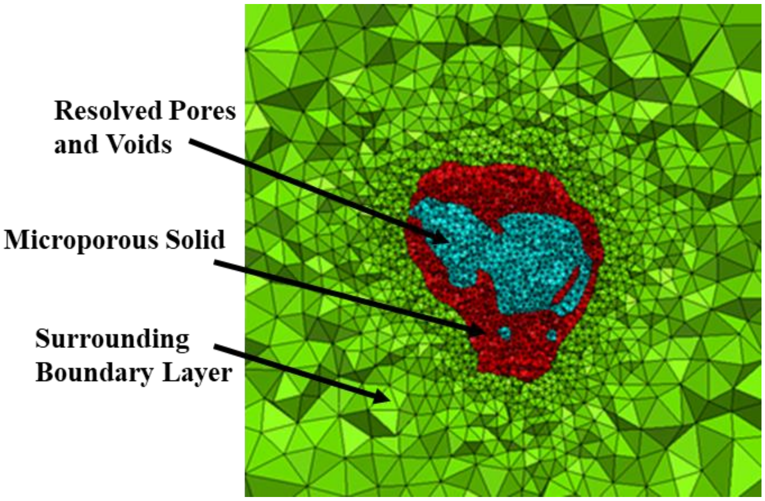

Fig. 3-4 Cross-section of a portion of the meshed computational domain for a char particle: Resolved pores (blue), microporous solid (red) and part of the surrounding boundary layer (green).

3.2.3.2 Biomass char

To focus on the impacts of morphology, all biomass particles were isotropically scaled by a small factor such that the total volume of each char particle (which includes the volume of microporous char and resolved pores) was identical. Morphological measurements for each particle were then performed (see Appendix). Individual biomass char particles were placed in the center of a spherical domain with a diameter of 1300 μm, which was meshed with tetrahedra using Scan IP's "+FE Free" algorithm. The same boundary conditions were used for biomass and coal char. Particles were assumed to be perfectly entrained in the flow, so, again, no relative (slip) velocity was imposed, although the boundary velocity was free to adjust itself according to Stefan flow effects arising from non-equimolar heterogeneous reaction.

A cross-section of a typical segmented and meshed biomass particle is shown in Fig. 3-5. Like the coal char particles, the large pores (blue regions), which violate the size constraints for an effective continuum treatment, were fully resolved in the geometry, and standard gas-phase conservation equations (mass, momentum, species, and thermal energy) were applied in those regions. The same first-principles conservation equations were applied in the gas boundary layer surrounding the particles (green regions). For the "microporous char" (red regions), which contains much smaller micropores, mesopores, and macropores that satisfy the size constraints for upscaling, effective-continuum conservation equations were applied (for mass, momentum, species, and thermal energy, see Section 3.2.3.3). A mass source term was included in the mass conservation equation to account for gas species generated due to the heterogeneous reactions, which occur on the surface of unresolved microporous char. The ideal gas equation of state was employed for these high-temperature, atmospheric pressure combustion simulations.

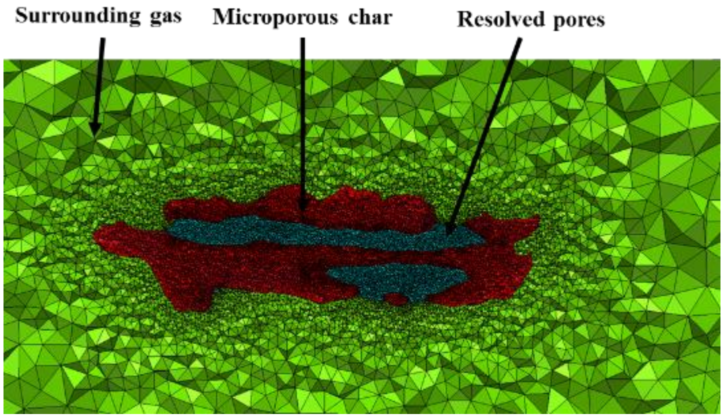

Fig. 3-5 Cross-section of typical meshed domain of a biomass particle, showing surrounding gas (green), microporous char (red), and resolved pores (blue).

All submodels and parameters for transport and reaction are identical to those used in the microporous char in the pore-resolving simulations, except for the subgrid-scale porosity, which is larger in the effective-continuum model, because large pores are lumped into the subgrid-scale. The boundary conditions and solvers were identical to those used for the pore-resolving model. A finite cylindrical particle with uniform porosity and identical total volume to the pore-resolving particles was meshed. The total porosity and aspect (length-to-radius) ratio, β, were chosen to be identical to one of the biomass char particles described in next section.

3.2.3.3 Governing equations and sub-models

In the “resolved pores” region (as well as the “surrounding gas” region) that violates the size constraints for an effective continuum assumption, standard conservation equations based on the first principles were applied. The conservation equations are given by [44]:

$$\frac{\partial(\rho)}{\partial t} + \nabla * (\rho\vec{v}) = 0 \qquad (3-2)$$

$$\frac{\partial(\rho\vec{v})}{\partial t} + \nabla * (\rho\vec{v}\vec{v}) = -\nabla p + \nabla * \left(\bar{\bar{\tau}}\right) \qquad (3-3)$$

$$\frac{\partial(\rho Y_i)}{\partial t} + \nabla * (\rho\vec{v}Y_i) = -\nabla\vec{J_i} \qquad (3-4)$$

$$\frac{\partial(\rho E)}{\partial t} + \nabla\cdot\big(\vec{v}(\rho E + \rho)\big) = \nabla\cdot\Big[k\nabla T - \Big(\sum_i h_i\vec{J_i}\Big) + (\bar{\bar{\tau}} * \vec{v})\Big] \qquad (3-5)$$

Classical upscaled effective continuum equations for mass, momentum, species, and energy conservation were solved within the “microporous char” region, which contains smaller, sub-grid-scale pores [44,127].

$$\frac{\partial\theta\rho}{\partial t}+\nabla(\theta\rho\vec{v})=S_m \qquad (3-6)$$

$$\frac{\partial\theta\rho\vec{v}}{\partial t}+\nabla(\theta\rho\vec{v}\vec{v})=\ -\theta\nabla P+\nabla(\theta\bar{\bar{\tau}})-\left(\frac{\theta^2\mu}{B}\vec{v}\right) \qquad (3-7)$$

$$\frac{\partial\theta\rho Y_i}{\partial t}+\nabla(\theta\rho\vec{v}Y_i)=-\nabla\vec{J}_i+R_i \qquad (3-8)$$

$$\frac{\partial\big(\theta\rho_f E_f+(1-\varepsilon)\rho_s E_s\big)}{\partial t}+\nabla*\Big(\vec{v}\big(\rho_f E_f+p\big)\Big)=\nabla\left(k_f\nabla T-\left(\sum_i h_i\vec{J}_i\right)+\left(\bar{\bar{\tau}}_{eff}*\vec{v}\right)\right)+S_f^h \qquad (3-9)$$

where θ is the porosity, ρ is the density, $\vec{v}$ is the velocity, S_m is the mass source term, t is the time, P is the pressure, $\bar{\bar{\tau}}$ is the stress tensor, μ is the dynamic viscosity, B is the permeability, Y_i is the mass fraction for species i, $\vec{J}_i$ is the diffusion flux for species i, R_i is the rate of production for species i, h is the enthalpy, E_f is the total fluid energy, E_s is the total solid medium energy, k_{eff} is the effective thermal conductivity of the medium, T is the temperature, and S_f^h is the fluid enthalpy source term.

A source term in the continuity equation represents net positive gaseous species generated by heterogeneous reactions within the porous region (leading to Stefan Flow). Heterogeneous reactions occur on the sub-grid-scale surface which belongs to the effective continuum region. A viscous resistance term corresponding with permeability is to account for the effects caused by porous medium. The volumetric species and energy source terms contributed by the diffusion and reactions are also included in equations. The intrinsic reaction rate has been described in the previous section and standard models for molecular and Knudsen diffusion are included.

One oxidation reaction and two gasification reactions are represented by global heterogeneous expressions for coal char combustion

$$C + \frac{\omega + 2}{2(\omega + 1)} O_2 \rightarrow \frac{\omega}{\omega + 1} CO + \frac{1}{\omega + 1} CO_2 \qquad \text{R1}$$

$$C + CO_2 \rightarrow 2CO \qquad \text{R2}$$

$$C + H_2O = H_2 + CO \qquad \text{R3}$$

where ω is the product ratio of CO to CO_2 and can be obtained from [128]

$$\omega = 70 \exp\left(-\frac{3070}{T_p}\right) \qquad (3-10)$$

For coal char particles, heterogeneous oxidation and gasification reactions were considered but gasification reactions were nearly three orders of magnitudes slower than oxidation at the conditions simulated. For the biomass particles, the gasification reactions were not considered. Homogenous reactions were not considered for either coal or biomass, due to the small particle size [81], and radiation was assumed to be dominated by particle-to-particle radiation among particles of similar temperature.

Power law (*n*th order) kinetic expressions were employed for gasification and a 1st order expression was used for oxidation. Arrhenius rate constants with pre-exponential factors and activation energies based on the review in [46,129]were used (see table 4-1) and are the same as used in [128] for coal char. For biomass, kinetic parameters in

Arrhenius rate constant and reaction order for biomass char oxidation [130] used in the 3-D pore-resolving simulations (see table 4-2). Generally, the reaction source term in species conversion equation represents intrinsic reaction kinetic, which is expressed as

$$R_i = S k_i P_i^n \tag{3-11}$$

$$k_i = A_{s,i} \exp\left(\frac{-E_i}{R_u T_p}\right) \tag{3-12}$$

Table 3-1 Reaction kinetic parameters for coal char particle.

Reaction	$S\ (\frac{m^2}{m^3})$	$A_s\ (\frac{kmol}{m^3 \cdot s \cdot atm^n})$	$E\ (\frac{kj}{mol})$	n
R1	3.79×10^7	7.91×10^7	127	1
R2	3.79×10^7	1.45×10^8	230	0.4
R3	3.79×10^7	2.90×10^8	230	0.4

Table 3-2 Reaction kinetic parameters for biomass char particle.

Reaction	$A_s\ (\frac{kmol}{m^3 \cdot s \cdot atm^n})$	$E\ (\frac{kj}{mol})$	n
R1	1.52×10^7	100.4	1

The molecular diffusion expression employed in the resolved pores and gas regions is given by [131]:

$$D_{m,i} = \frac{(1.0 * 10^{-7}) T^{1.75} \sqrt{\frac{MW_i + MW_{avg}}{MW_i MW_{avg}}}}{P\left(v_i^{\frac{1}{3}} + v_{avg}^{\frac{1}{3}}\right)^2} \tag{3-13}$$

In the microporous solid, both Knudsen and molecular diffusion were considered in formulating effective diffusion coefficients, D_{eff}, due to the small pore sizes in those regions. The Knudsen diffusion coefficient for species *i* is given by:

$$D_{Knud,i} = \frac{d_{pore}}{3}\sqrt{\frac{8R_uT}{\pi MW_i}} \qquad (3-14)$$

where the mean pore diameter, d_{pore}, is calculated using

$$d_{pore} = \frac{4\theta}{S} \qquad (3-15)$$

where θ represents the porosity.

The effective diffusivity of the microporous solid is then calculated from $D_{Knud,i}$, the mixture-averaged molecular diffusion coefficient, $D_{m,i}$, the porosity, θ , and the tortuosity τ, which is taken to be unity

$$D_{eff,i} = \frac{1}{\left(\frac{1}{\frac{\theta}{\tau}D_{Knud,i}} + \frac{1}{\frac{\theta}{\tau}D_{m,i}}\right)} \qquad (3-16)$$

In the surrounding boundary layer and in the resolved pores, standard, gas-phase mixture-averaged diffusion coefficients were used. The viscosity and thermal conductivities were determined using kinetic theory and standard mixing rules and the ideal gas equation was used. The density of species *i* in the gas phase is determined by the ideal gas equation of state. Viscosity and thermal conductivity for each species are based on kinetic theory.

3.2.3.4 Discretization and mesh validation

Each segmented particle was individually meshed with tetrahedra using Scan IP's "+FE Free" meshing algorithm. A finer mesh was used in the particles and near the interface between microporous solid and resolved pores, while a coarser mesh was employed in the boundary layer (see Fig. 3-4 and 3-5). Being a low Mach number, variable density problem, the pressure-based solver was used for solving the governing equations, using the coupled algorithm. The power law scheme was used for most spatial finite volume discretization, but the PRESTO! scheme was used to compute the pressure.

A mesh study was performed to ensure that the solution was converged with respect to the spatial discretization. Three meshes (consisting of approximately one million, two million and four million elements) were used to compute the steady state solution for a particle chosen at random. The oxygen mole fraction, a variable which varies drastically and irregularly throughout the computational domain (as will be seen in next section), was averaged over polar and azimuthal directions, and plotted versus radius in Fig. 3-6. The relative error for the one- and two-million element meshes was 0.0173 and 0.0144, respectively. A mesh of approximately two million elements was deemed sufficient and used for every particle studies. The computation time for each 3-D particle with a two million element mesh was approximately 140 hours on a 28-core CPU.

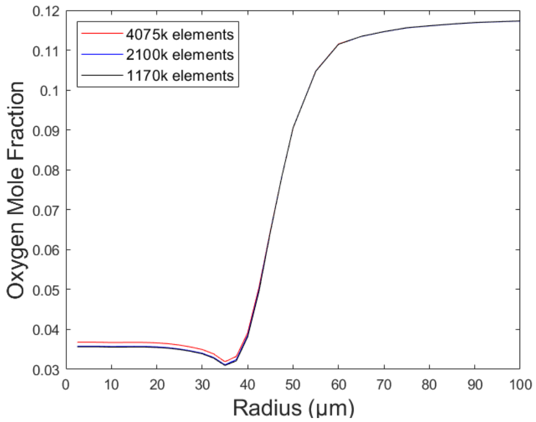

Fig. 3-6 Comparison of directionally averaged oxygen mole fraction for different meshes.

3.3 Results and discussion

3.3.1 Transient and steady-state solutions

Studies have established, at least for simple effective-continuum geometries, that the instantaneous distribution of species in reacting sub-millimeter char particles is approximately quasi-steady at any time [132,133]. In other words, a transient simulation for a reacting pulverized char particle would be closely represented by a series of steady state simulations at different levels of char conversion. This implies that steady-state simulations provide an accurate representation of the transport-reaction coupling for a *given* morphology. However, a comparison between steady-state and transient solutions was performed to ensure that the former provides an adequate representation of the latter for the complex char particles and conditions simulated in this study.

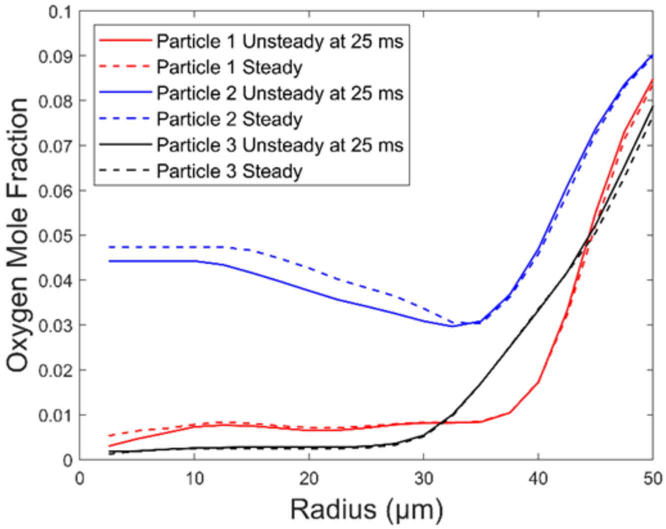

Fig. 3-7 Comparison of directionally averaged oxygen mole fraction within three different particles for steady and transient simulations.

Radial distributions of oxygen mole fraction averaged over polar and azimuthal angles are compared for transient [44] and steady-state simulations in Fig. 3-7, for three coal particles. The predictions are compared at (an early time of) 25 ms to minimize the degree of structural evolution that occurred in the transient simulation. The reason that an even earlier time was not used for comparison is because fast transients exist at the beginning of the unsteady simulation as the species profiles adjust to the imposition of the boundary conditions. All three particles yielded similar results for both transient and steady simulations, with average relative differences of 6.93%, 4.63%, 4.46%. Some, or perhaps most, of this difference can be attributed to the carbon conversion that occurred in the first 25 ms of the transient simulation. It is concluded that steady state simulations are reasonable representations of the interplay of reaction and diffusion for a given morphology and therefore sufficient for the purposes of this study.

3.3.2 3-D simulations for coal char particles

The combustion of 150 char particles imaged with high-resolution micro-CT was then simulated using the pore-resolving CFD model, with approximately two million elements per particle. Figure 3-8 shows 3-D morphologies of six representative char particles ranging from highly cenospherical to more complex pore structures (Fig. 3-8(a)), as well as the oxygen mole fraction distributions (Fig. 3-8(b)) and temperature distributions (Fig. 3-8(c)) for planes passing through the centers of the same particles. It is noted that the oxygen mole fraction and temperature are shown for both the resolved pores and the microporous char regions.

It is observed in Fig. 3-8(b) that the oxygen mole fraction distribution is highly dependent on the structure of the resolve pores and pores and is elevated in those regions. For all char particles, the minimum oxygen mole fraction is located within the microporous char and not at the particle center. This indicates that for most particles, small holes exist that allow for enhanced transport between the particles' interior pores and the external surface. Even for the most cenospherical particle (the leftmost particle in Fig. 3-8), the minimum oxygen mole fraction occurs in the thickest region of microporous solid, although the concentration in the central resolve pore is only slightly higher than its minimum value due to the lack of holes on the surface of this particle (this was verified in three dimensions). For the more complex network-type char structures, the oxygen mole fraction is highly asymmetric and does not vary monotonically between the particle surface and its center.

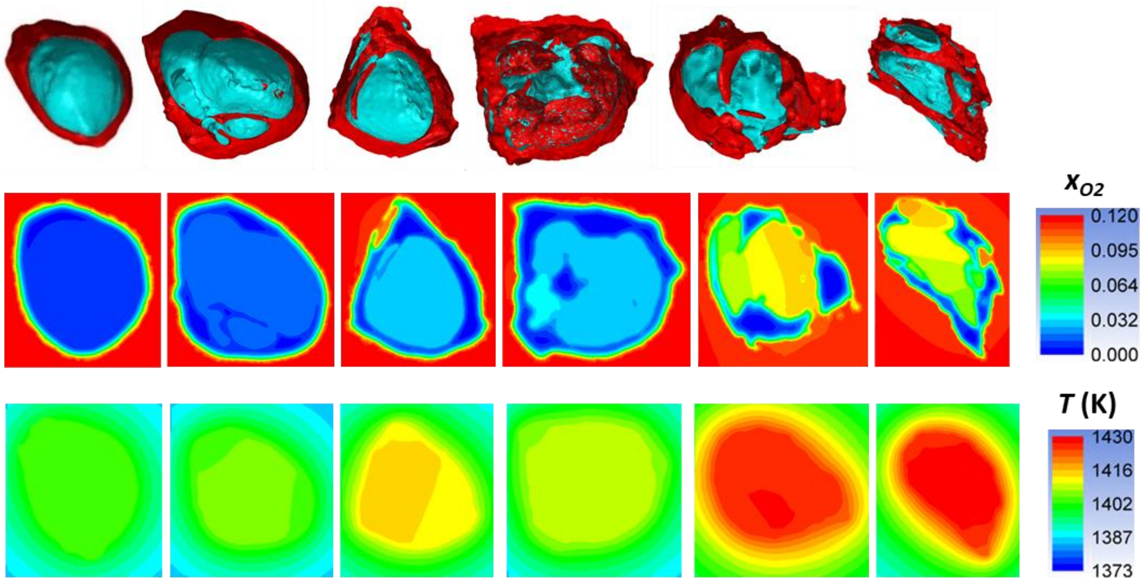

Fig. 3-8 (a) Three dimensional geometries of six particles, showing microporous char (red) and resolved pores (blue), together with, (b) oxygen mole fraction distributions, and (c) temperature distributions, for two dimensional sections of the same particles.

In contrast to the highly non-uniform oxygen mole fraction, the temperature distribution is nearly spatially uniform and does not exhibit marked differences between the resolved pores and the microporous char, as shown in Fig. 3-8(c). The observed temperature gradients reside primarily around the outer edge of the particles. This is not unexpected, due to the small size of the pulverized char particles, their relatively high thermal conductivity, and the quiescent atmosphere associated with particles assumed to be entrained in the surrounding flow. This gives rise to a Biot number much smaller than unity and nearly uniform internal temperatures. It is noted that this conclusion may not hold in conditions closer to zone III (diffusion-limited) combustion in which the temperature rise would be higher. The volume averaged particle temperature for the hottest burning particle was 1430 K, while for the coolest particle it was 1403K.

The reactant and temperature distributions are also investigated with increased boundary temperature to simulate the combustion condition transitioning from zone II to zone III. Fig. 3-9 shows temperature and oxygen mole fraction distributions for planes passing through the centers of three representative particles, for several values of the far field temperature based on certain properties. Particle 1 (P1) has resolved pores which are isolated from the external surface and low θ ($\theta = 0.188$) (Fig. 3-8(a)). Particle 2 (P2) has a high portion of resolved pores connected to the external surface and high θ ($\theta = 0.411$) (Fig. 3-9(b)), and Particle 3 (P3) has a low portion of its resolved pores connected to the external surface, but high θ ($\theta = 0.528$) (Fig. 3-9(c)).

It is observed in Fig. 3-8 that the distribution of oxygen (reactant) within a particle depends on whether its large pores are accessible to the outer surface. For P1, which has a single, isolated resolve pore, the minimum oxygen mole fraction is widely distributed across both microporous solid and the central resolve pore, with higher levels only observed near the particle surface. The oxygen mole fraction decreases monotonically toward the particle center through the thick microporous solid region due to the lack of pores that intersect the external surface. With increasing boundary temperatures, there is little difference in the oxygen mole fraction distributions for the P1 particle.

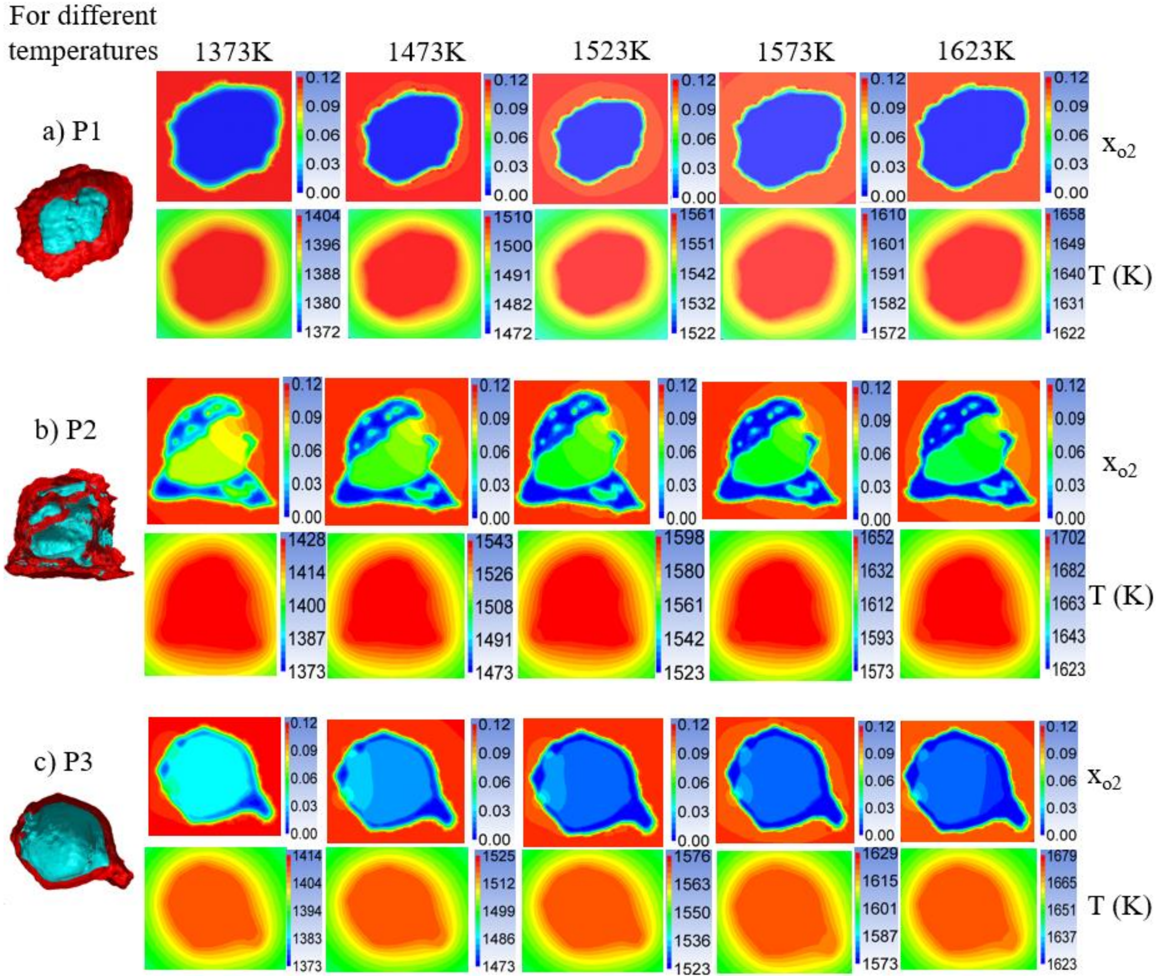

Fig. 3-9 3-D morphology of particles P1, P2 and P3 and their oxygen mole fraction (X_{O2}) and temperature (T) distributions, for several temperature boundary conditions.

The P2 particle, which has several pores which penetrate the external surface, exhibits a non-uniform and non-monotonic oxygen mole fraction distribution that is highly dependent on the morphology of the pores. The minimum oxygen mole fraction for P2 is located within its microporous solid, which is not the case for P1. Similar to what has been found previously, the oxygen mole fraction in the resolved pores is highly asymmetric, with pores intersecting the external surface exhibiting higher oxygen mole fractions. Holes in the particle surface enhance reactant transport within the particle. The oxygen mole fraction decreases and becomes more uniform within the resolved pores as the far-field boundary temperature increases because conditions become closer to zone III combustion (external-diffusion-limited), decreasing the importance of surface accessibility.

The P3 particle exhibits elevated oxygen mole fraction in the cracks with a somewhat more uniform oxygen distribution inside the particle. At a given temperature, the average oxygen mole fraction within P3 is higher than P1, which has a similar structure but lower resolved porosity, but it is lower than P2 even though the P3 has a higher resolved porosity. This is because gas transport is controlled by the morphology of the pore-structure, and particularly, by pores with access to the external surface.

Temperature distributions for all particles are nearly spatially uniform, regardless of the accessibility of the pores or the far field boundary temperature, with temperature gradients observed only near the particle edges. The nearly-uniform internal temperatures are due to the small size of the pulverized particles, high thermal conductivity, and the entrained flow assumption, leading to small Biot numbers as discussed before. However, it is noted that P2 has a higher temperature than P3, and P1 has the lowest temperature, because oxygen readily penetrates the P2 particle via its small holes, causing increased rates of exothermic oxidation.

The types of coal particles mentioned above are summarized from the particles that are arranged on the abscissa in an increasing order of the external void fraction

(EVF), an indicator which increases as particles transition from cenospheres with isolated resolve pore to more complex and connected pore structures. The EVF is defined as

$$\mathrm{EVF} = \frac{S_{ext,void}}{S_{ext,total}} \tag{3 - 17}$$

where $S_{ext,total}$ is the total interfacial area between the particle and surrounding boundary layer (the green/red and green/blue interface areas in Fig. 3-4), and $S_{ext,void}$ represents the interface area between the resolve pores and surrounding boundary layer (the green/blue interface in Fig. 3-4). This ratio decreases as the particles becomes more cenospherical, with a single, isolated central resolve pore, and increases for particles with more numerous and complex pores that penetrate the particle surface. In other words, the order of particles along the abscissa places the (mostly thick-walled) cenospheres on the left and the more connected, complex pore structures on the right.

Based on that, the distribution of oxygen within in the selected particles are displayed in Fig. 3-10, in which the oxygen mole fraction calculated by the pore-resolving simulations, x_{O2}, within microporous solid regions is averaged over polar and azimuthal angles at every radial position, using

$$x_{O2,mps} = \frac{\int_0^{2\pi}\int_0^{\pi} \delta\, x_{O2}(r,\theta,\varphi) r^2 \sin(\theta)\, d\theta d\varphi}{\int_0^{2\pi}\int_0^{\pi} \delta r^2 \sin(\theta)\, d\theta d\varphi} \tag{3 - 18}$$

where δ is unity for microporous solid regions and zero elsewhere. Microporous solid oxygen mole fraction distributions are shown for 15 representative particles in Fig. 3-10: five cenospheres ("Group 1"), five transitional particle ("Group 2"), and five particles with network structures ("Group 3"). The plot lines are interrupted when there is no microporous solid at a particular radial position.

The oxygen mole fraction on the external surface is similar across all groups, and all three groups exhibit a sharp decrease in the oxygen mole fraction between the external surface and a radius of ~40 µm. This drop is likely due to those points being comprised of protrusions where the average oxygen mole fraction is high, and the reaction rate is correspondingly fast.

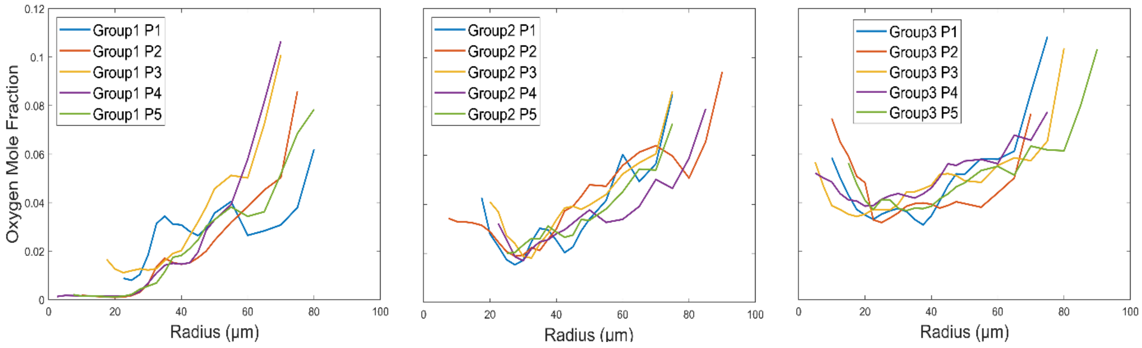

Fig. 3-10 Oxygen mole fraction in the microporous solid as a function of radius (averaged over polar and azimuthal angles) for 5 particles (P1-P5) from (a) cenospherical, (b) transitional and (c) network particle groups calculated from the pore-resolving simulation.

More pronounced differences are observed in Fig. 3-10 near the center of the particles. For Group 1, the oxygen mole fraction keeps decreasing in the microporous solid regions toward the particle center until it approaches or reaches zero. Conversely, for Groups 2 and 3, the oxygen mole fraction *increases* toward the particle center. In fact, for some particles in Group 3, the oxygen mole fraction in microporous regions near the particle center approaches its surface value. The large pores connected to the external surface facilitate the transport of oxygen throughout the particle and the characteristic length-scale for diffusion is much smaller than the particle radius. This leads to higher oxygen concentration in the microporous solid in the complex particles compared to the particles that have isolated central resolve pores, as seen in Fig. 3-10.

The relatively high oxygen mole fraction throughout the pore space of the more complex particles is verified in Fig. 3-11, in which the oxygen mole fraction within the resolved pores is averaged over polar and azimuthal angles at every radial position for the same 15 particles shown in Fig. 3-10. To obtain the data in Fig. 3-11, Eq. (3-18) is again used, but in this case δ is unity for the resolved pores and zero in other regions. For the cenospherical particles (Group 1) the oxygen mole fraction is nearly uniform in the resolve pore space and significantly lower than its surface value, due to the near isolation of the central resolve pore from the external surface. For the transitional (Group 2) and network-type (Group 3 – highest EVF) particles, the oxygen mole fraction is higher in the resolved pores due to their connectedness to the external surface.

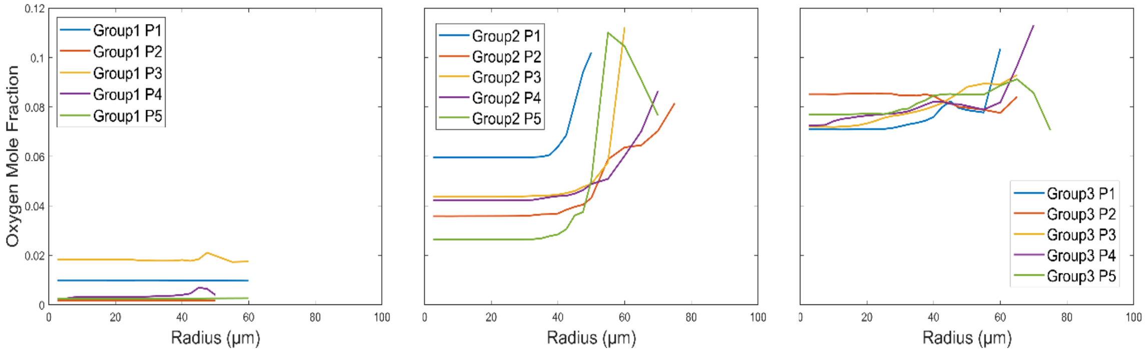

Fig. 3-11 Oxygen mole fraction in the resolved pores as a function of radius (after averaging over polar and azimuthal angles) for (a) cenospherical, (b), transitional and (c), network particles calculated from the pore-resolving simulation.

3.3.3 3-D simulations for biomass char particles

Zone II combustion of 30 biomass char particles with geometries obtained from high-resolution micro-CT was studied using the pore-resolving simulations. Figure 3-12 shows the 3-D segmented geometries for five representative particles as well as an effective-continuum cylinder (top row) and cut-away views of the same segmented particles (second row). The particles are generally long and thin, with a mean aspect ratio of 6.25. This suggests that simple models based on cylindrical particles rather than spherical particles, are more appropriate for this biomass char, as observed for many other biomasses. It is also noted that even particles which appear externally non-porous can have significant internal porosity. For the 30 particles, the resolved (large pore) porosity, θ_{void}, ranged from 6.3% to 27.5%. In Lester's biomass char nomenclature [113], these chars would be classified as high-aspect ratio, porous (as opposed to cellular) structures.

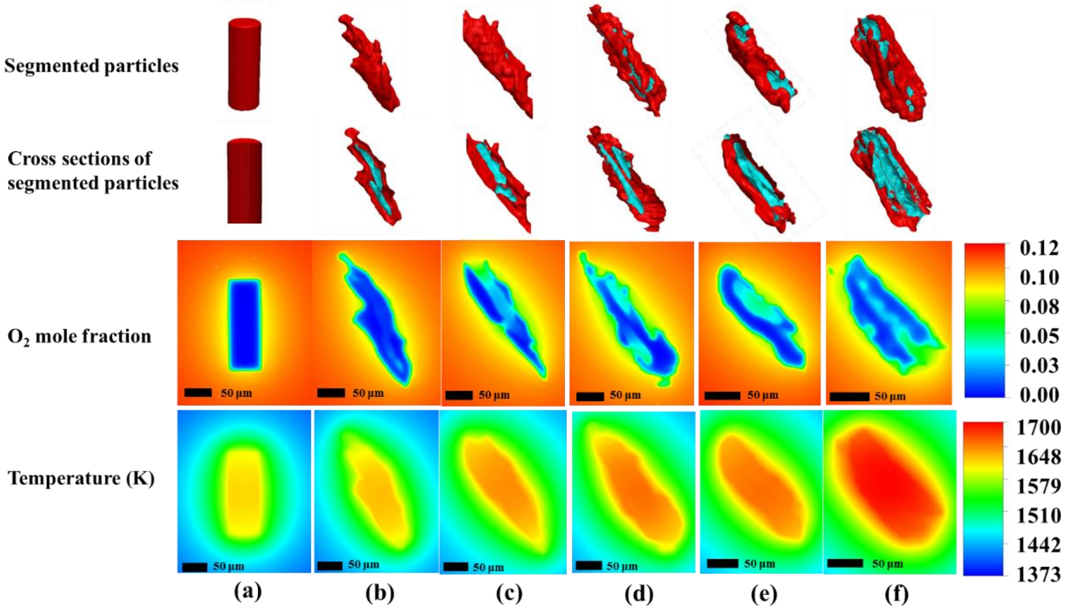

Fig. 3-12 Top row: 3-D geometries for a cylindrical effective continuum particle (column a) and five real, segmented biomass char particles (columns b, c, d, e, and f) showing microporous char in red and resolved pores in blue. Second row: cross-sections of the same particles. Third row: oxygen mole fraction distributions for the same particles cross-sections, calculated from the simulations. Fourth row: temperature distributions for the same particles, calculated from the simulations.

Figure 3-12 also shows distributions of oxygen mole fraction, x_{O2} (third row) and temperature (fourth row) for the same cross-sections, which pass through the center of the biomass char particles. It is noted that the x_{O2} distributions for the real biomass char particles are highly dependent on the morphology, as observed for coal chars undergoing zone II combustion. Local minima in x_{O2} occur in the thick microporous char regions, irrespective of the distance from the particle surface. The large pores facilitate enhanced oxygen transport from the particle surface to its interior regions. This is somewhat similar to the impact of mm-scale cracks in larger biomass particles [134], but differs from the general observation that char oxidation is confined to the edges of mm-scale particles [135]. It is noted, however, that despite the significant porosity observed for "Particle B" (see Fig. 3-12, second row), x_{O2} is only slightly elevated in this particle's interior. This highlights the fact that large pores facilitate enhance gas transport only if the pores penetrate the particle's external surface, which is only minimally the case for Particle B.

For the effective-continuum cylindrical particle (Particle A), all porosity is modeled at the subgrid-scale, and it is uniformly distributed. In this frequently used model, large pores cannot facilitate oxygen diffusion into the particle interior, leading to a monotonic x_{O2} distribution, with the highest oxygen mole fraction at the external surface and the lowest oxygen mole fraction on the particle's central axis. It is noted that the total porosity of Particle A is identical to the total porosity ($\theta + \theta_{subgrid-scle}(1 - \theta)$) of Particle E, highlighting the importance of large pores in enhancing gas diffusion throughout the particle.

In contrast to x_{O2}, temperature distributions within all particles (effective-continuum and real biochar) are nearly spatially uniform throughout both the large pores and microporous char regions. Small temperature gradients are observed near the edges of the particles, but most of the gradients exist in the surrounding gas (the far-field boundary is at 1373 K). This is similar to the situation for pulverized coal char and is due to the small particle sizes and high thermal conductivity resulting in small Biot numbers. Although temperature is relatively uniform within each particle, differences between particles are non-negligible. The effective-continuum particle has the lowest spatially averaged temperature (1609 K), whereas the particle with the highest oxygen penetration (Particle F) has the highest spatially averaged temperature (1680 K). Increasing levels of large porosity connected to the external surface led to higher oxygen penetration, higher char oxidation rates, more heat release, and higher temperatures.

To further examine the impacts of large pores and to compare oxygen penetration in real morphologies to effective-continuum predictions, Particles A and E, which have the same total porosity, were compared. Figure 3-12 shows the directionally averaged oxygen mole fraction as a function of effective radius, which is calculated for the approximately cylindrical Particle E in the following manner. A set of 3-D iso-surfaces were created between the particle center and edge such that each point on an iso-surface is the same normal distance from the particle's edge. Then, the effective radius was defined in eq (3-19) using the relation between the surface area of a cylinder and its radius and length. First, the surface area of each irregular iso-surface layer, S_{layer}, is measured using surface integration. The aspect ratio of each layer, β_{layer}, is identical and is equal to β_{bio} measured by bounding box method. It should be noted that this method overestimates both length and radial directions. The effective radius, r_{eff}, for each iso-surface is then calculated by rearranging the expression for the area of a cylinder

$$r_{eff} = \sqrt{\frac{S_{layer}}{2\pi(1+\beta_{bio})}} \qquad (3-19)$$

The oxygen mole fraction was then area-averaged over each iso-surface in two different ways. In the first method, the averaging was performed only over the microporous char regions, while in the second method, averaging was performed over both the microporous char and resolved pores (all regions).

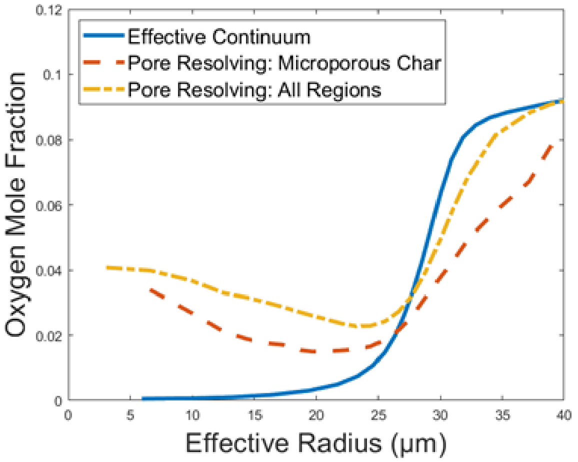

Fig. 3-13 Oxygen mole fraction as a function of effective radius, for the pore-resolving simulation and the spatially resolved effective continuum simulation.

When averaging over all regions, it is seen in Fig. 3-13 that the real biomass char particle has a higher x_{O2} in the particle interior than the effective continuum particle, as expected from the enhanced oxygen penetration in the large resolve pores, seen in Fig. 3-12. However, even in the microporous char, x_{O2} is higher for the real particle than the effective continuum particle, despite the porosity of the microporous char being lower for the real particle (since the total porosity of the two particles is the same and the effective-continuum particle lumps all porosity at the subgrid-scale). The reason is likely that the elevated x_{O2} in real biomass char pores and the large interfacial area between those pores and the microporous char leads to enhanced penetration into the microporous char. The characteristic length-scale for diffusion is thus decreased for the real biomass char particles. In contrast, for the effective continuum particle, oxygen must traverse the entire radius of the particle from its outer edge. Finally, it is noted that the higher x_{O2} at the outer edge for the effective continuum particle is likely caused by its higher porosity in the microporous char regions, as mentioned above. In the edge regions of both particles, oxygen diffuses primarily from the particle surface and the higher subgrid-scale porosity in Particle A leads to higher oxygen concentrations.

3.4 Conclusions

High-resolution micro-CT imaging was performed for pulverized coal char particles and pine biomass char particles (sieved to 100 μm) to obtain the internal and external geometries in 3-D. The first pore-resolving, zone II combustion simulations for real char particles were then carried out for 150 coal char and 30 biomass char particles. The pore-resolving simulations respect the separation of length-scales required for effective-continuum treatments of porous media, by applying equations based on the first principles in the resolved pores and the surrounding boundary layer, and only using effective-continuum conservation equations in the microporous solid regions where the pore size is much smaller than the size of the particles.

The reactant (oxygen) mole fraction distribution in real coal char particles was highly dependent on the morphology of large pores, was non-monotonic with distance from the particle’s surface, and attains local minima within thick microporous char regions irrespective of the distance from the external surface. The prevalence of complex interconnected large pore networks that extend to the external surface enhanced oxygen transport throughout the particle, even within microporous solid regions near the particles’ centers. Conversely, particle temperatures were nearly spatially uniform throughout the particles, irrespective of the resolve pores morphology, for the zone II condition examined in this study.

Similar observations apply to the anisotropic pine char particles imaged with high-resolution micro-CT. They exhibited non-monotonic oxygen mole fraction distributions facilitated by enhanced diffusion in large pores that were connected to the external surface. Effective-continuum simulations underpredicted reactant penetration into the particle, even in the microporous char regions that surround the large pores.

Chapter 4. Effectiveness Factor Models Evaluation and Development

This chapter will assess the performance of common effectiveness factor models using the “true” effectiveness factors calculated from the 3-D pore-resolving simulation for each coal and biomass char particle.

The first section explains how true 3-D effectiveness factor calculated using data from the 3-D pore-resolving simulation. In Section 4.2, detailed effectiveness factor models that are applied for either coal or biomass particles will be discussed. The comparison is presented in Section 4.3, with subsections devoted to coal and biomass.

4.1 Introduction

In the last chapter, it was observed that the reactant (oxygen) mole fraction distribution in real coal char particles is highly dependent on the morphology of resolved pores and facilitates enhanced diffusion in large pores that are connected to the external surface for both coal and biomass char particles.

As indicated in Chapter 2, in order to account for the impact of diffusion on the volume-integrated reaction rate in porous particles, the effectiveness factor, η, is used. In reactor-scale CFD codes, particle-scale models calculate the actual reaction rate by solving a simple, analytical model for η and multiplying by the ideal reaction rate which can be computed using Eulerian-phase data for the cell containing the particle. Because many Eulerian-phase source terms are proportional to the reaction rate, the accuracy of the particle-scale model can significantly affect the performance of reactor-scale CFD [96,136].

In this case, the performance of existing effectiveness factor models based on assumptions of idealized shape and a variety of other simplifications is questionable. To increase the accuracy of the reactor-scale CFD simulation, it is first necessary to assess existing effectiveness factor models using actual (or “real”) effectiveness factors based on 3-D pore resolving simulation. To display representative data, particles with varied structures (50 of the coal chars and all 30 biomass chars) will be evaluated.

To assess the accuracy of simple models for real char morphologies, pore-resolving simulations can be used to calculate the “true” 3-D effectiveness factor using numerical integration,

$$\eta_{3D} = \frac{\iiint R_{actual}(x_{O2},T)dV}{\iiint R_{ideal}(x_{O2,s},T)dV} \qquad (4-1)$$

The actual reaction rate, R_{actual}, employs oxygen mole fraction, x_{O2}, data for each location in the microporous char, whereas the ideal rate, R_{ideal}, is calculated using a uniform reactant concentration throughout the particle equal to its boundary value, $x_{O2,s}$, which would prevail in the absence of internal diffusion limitations. Both actual and ideal rates use temperatures, T, for each local position in the char.

The formulation of the effectiveness factor models is presented for the case of a first order reaction, consistent with the rate expression for oxidation used in the pore-resolving simulation, although effectiveness factors for nonlinear rate expressions are possible. To ensure a faithful comparison between the predictions of the 3-D pore resolving simulation and the effectiveness factor models for each of the coal char particles and biomass char particles, the latter employed geometric and morphological parameters (interfacial area, resolve pore porosity, etc.) obtained from micro-CT image analysis of each particle. The predictions of the 3-D models are not used to tune the effectiveness factor models in any way.

4.2 Effectiveness factor models

4.2.1 Coal char

4.2.1.1 Uniform sphere

The uniform sphere model and flat plate model have been briefly discussed in Chapter 2, but will be explained in more detailed here for our specific case. The classical expression for the effectiveness factor of a uniformly porous, symmetrical sphere is given by

$$\eta_{sphere} = \frac{3}{\phi_{sphere}}\left(\frac{1}{\tanh(\phi_{sphere})} - \frac{1}{\phi_{sphere}}\right) \qquad (4-2)$$

where ϕ_{sphere}, the Thiele modulus, represents the ratio of the reaction rate to the diffusion rate within the porous particle. For a first order reaction, it is given by [137]

$$\phi_{sphere} = R\sqrt{\frac{S(1-\theta)\,k}{D_{eff}}} \qquad (4-3)$$

where R is the particle radius, k is the intrinsic (per unit area) heterogeneous rate constant of the solid divided by its density (with resultant units of length per time) and S, θ and D_{eff} have been defined. For each particle, the radius, R can be calculated using the 3-D geometries obtained from micro-CT by averaging the distance from each node on the interface between the particle and the surrounding boundary layer to the particle's center. However, due to the scaling represented by Eq. (3-1), R was exactly 50 µm for all particles in this study. This allows for a focus on the effects of morphology, while eliminating the effect of particle size.

The uniform sphere model is unique among the effectiveness factor models to be examined in that it does not account for the resolved porosity, θ, in calculating the length scale of the particle. Therefore, to ensure that the mass of carbon and total internal surface area per particle is consistent with the corresponding 3-D simulation, the reactive surface area, S, of the uniform sphere model includes the factor $(1-\theta)$, which represents the volume fraction of microporous solid in each particle.

Due to the uniform sphere model's treatment of the resolved pore porosity at the sub-grid-scale, there is some ambiguity as to whether the total porosity

$$\theta_{Total} = \theta + \theta_{mps}(1-\theta) \qquad (4-4)$$

or the porosity of the microporous solid regions, θ_{mps}, should be used when calculating the Knudsen diffusivity, D_{Knud}, to achieve consistency with the 3-D pore-resolving simulation. Consistent with the approach of Hodge et al. [64,48] who compared effectiveness factor models to experimental data, the average pore diameter, d_{pore}, and D_{Knud} were calculated using θ_{mps}, which is based on the nanometer-scale micro- and meso-pores through which Knudsen diffusion is dominant, while the molecular diffusion coefficient, D_m, is evaluated using θ_{Total}.

For each particle simulated, the porosity of the resolved pores, θ, is obtained from the quotient of V_{mps} and $(V_{mps} + V_{voids})$, where the volume of each region was calculated using volume integration of the 3-D geometries obtained from micro-CT imaging (see Appendix for individual particle data).

4.2.1.2 Flat plate

Based on experimental evidence, it has been suggested that cenospherical and network char particles may be more accurately modeled as flat plates rather than uniform spheres [64]. The classical solution for the effectiveness factor of an infinite flat plate of thickness, L, is given by

$$\eta_{flat} = \frac{\tanh \phi_{flat}}{\phi_{flat}} \qquad (4-5)$$

where the Thiele modulus is given by

$$\phi_{flat} = \frac{L}{2}\sqrt{\frac{S\,k}{D_{eff}}} \qquad (4-6)$$

Treating each particle as a symmetric hollow sphere, the cenosphere wall thickness, L, which corresponds to the plate thickness, was calculated using the particle radius, R, and the porosity of the resolved pores, θ

$$L = R\left(1 - \theta^{\frac{1}{3}}\right) \qquad (4-7)$$

It is seen in Eq. (4-7) that in the flat plate model (as well as in the other analytical models to follow) the presence of large pores and voids is considered when formulating the geometry of the particle. In other words, the plate thickness, L, is based solely on the volume of microporous solid, V_{mps} and the resolve pore porosity is not treated as sub-grid-scale. Thus, the surface area, S, in Eq. (4-6) need not include the factor $(1-\theta)$, and the effective diffusivity, D_{eff}, is unambiguously calculated using θ_{mps}.

4.2.1.3 Hollow sphere models (inaccessible and accessible)

Buffham developed a lesser-known analytical solution for the effectiveness factor of a symmetric hollow sphere [64] based on [138], which may be more appropriate than the flat plate model for cenospheres, especially those with thicker walls. The effectiveness factor for a hollow sphere is given by

$$\eta_{inacc-hs} = \frac{3}{\phi_{inacc-hs}\left(1-\frac{R_{in}}{R_{out}}\right)}\left(\frac{\coth\left(\phi_{inacc-hs}\left(1-\frac{R_{in}}{R_{out}}\right)\right)+\phi_{inacc-hs}\frac{R_{in}}{R_{out}}}{1+\phi_{inacc-hs}\frac{R_{in}}{R_{out}}\coth\left(\phi_{inacc-hs}\left(1-\frac{R_{in}}{R_{out}}\right)\right)}-\frac{1}{\phi}\right) \qquad (4-8)$$

where R_{in} and R_{out} are the inner and outer radii, and the Thiele modulus ϕ is

$$\phi_{inacc-hs} = R_{out}\sqrt{\frac{S\,k}{D_{eff}}} \qquad (4-9)$$

R_{out} is identical to R, as previously defined, while the inner radius was calculated using the geometry of a hollow sphere, with θ from volume integration of the 3-D particles

$$R_{in} = R_{out}\theta^{\frac{1}{3}} \qquad (4-10)$$

The boundary conditions that were used to arrive at the analytical solution are a no flux condition at the center of the sphere and a fixed concentration at the external surface, which are identical to those used in deriving the effectiveness factor for a uniform sphere.

However, because many highly porous particles have large holes connecting the internal pores to the external surface, the solution for the effectiveness factor of a hollow sphere with a single, *accessible* central resolved pore η_{acc-hs}, is also relevant. This solution is obtained using a concentration boundary condition on the inner surface that is identical to that imposed on the external surface. This model is termed the accessible hollow sphere model, and its effectiveness factor is given by [139]:

$$\eta_{acc-hs} = \frac{3}{\phi\left(1-(\frac{R_{in}}{R_{out}})^3\right)} \begin{pmatrix} (1+\left(\frac{R_{in}}{R_{out}})^2\right) \coth\left(\phi\left(1-\frac{R_{in}}{R_{out}}\right)\right) \\ -2\frac{R_{in}}{R_{out}} cosech\left(\phi\left(1-\frac{R_{in}}{R_{out}}\right)\right) - \frac{1-\frac{R_{in}}{R_{out}}}{\phi} \end{pmatrix} \qquad (4-11)$$

For each particle, R_{out} and R_{in} are identical to those used in the inaccessible hollow sphere model, and based on individual 3-D measurements, as explained above. It is also emphasized that kinetic and transport parameters for each particle were consistent between the 3-D CFD simulations and the analytical models.

4.2.1.4 Generalized Cylinder Model (1D–GC) and Variable Diffusivity Model (1D–VD)

Another class of effectiveness factor models has been formulated to account for the complex three-dimensional structure of many catalyst particles in a one-dimensional framework [69,140], extending earlier approaches which use a particle’s volume to surface area ratio as the characteristic length-scale[68,141]. The generalized cylinder (1D–GC) and variable diffusivity (1D–VD) models, as outlined in [69,140], require a detailed characterization of the particle’s morphology, but have shown excellent accuracy in reproducing full 3-D calculations for catalyst applications (3% and 1% maximum error, respectively[140]). These models require assumptions of isotropic microporous regions, uniform reactivity in the microporous region, and uniform temperature and composition along the interface between the microporous solid and the surrounding fluid.

The 1D-GC model requires the solution of a 1-D reaction-diffusion equation for the (dimensionless) reactant concentration, Y, along the (dimensionless) coordinate, z, with dimensionless reaction rate $r(Y)$ and variable cross-section with shape factor, σ[69]:

$$z^{-\sigma}\frac{d}{dz}\left(z^{\sigma}\frac{dY}{dz}\right) = (1+\sigma)^2\phi_{1D-GC}^2\, r(Y) \qquad (4-12)$$

with boundary conditions

$$Y = 1\ at\ z = 1 \qquad (4-12a)$$

$$\frac{dY}{dz} = 0\ at\ z = 0 \qquad (4-12b)$$

The Thiele modulus, ϕ, is given (for an irreversible reaction) by

$$\phi = L\sqrt{\frac{S\,k}{D_{eff}}} \qquad (4-13)$$

where the characteristic length L, represents the ratio of the particle volume to its interfacial area. In the present context, the characteristic length, L, corresponds to

$$L = \frac{V_{mps}}{S_{mps,interface}} \qquad (4-14)$$

where $S_{mps,interface}$ is the interfacial area between microporous solid and resolved pores or external boundary layer (the interface between red and blue regions, as well as red and green regions, in Fig. 3-3). For each of the 50 particles, V_{mps} was calculated by volume integration and $S_{mps,interface}$ was calculated by surface integration over the interfaces in the 3-D structures obtained from micro-CT (see Appendix).

For the 1D–GCγ model (the variant of the model more appropriate at low Thiele modulus), the shape factor, σ, appearing in Eq. (4-12) requires the solution of Poisson's equation on the particle's surface[69]. The shape factor is given in terms of parameter γ

$$\sigma = \frac{3\gamma - 1}{1 - \gamma} \qquad (4-15)$$

where

$$\gamma = \frac{\iiint G dV_{mps}}{V_{mps}} \qquad (4-16)$$

and G is obtained from solving (dimensionless) Poisson's equation on the microporous solid domain

$$\nabla^{*2} G = -1 \ \text{ in } V_{mps} \qquad (4-17)$$

subject to boundary condition

$$G = 0 \ \text{ on } S_{mps,interface} \qquad (4-18)$$

In this study, Poisson's equation for *G* was solved numerically using COMSOL for each real 3-D particle geometry obtained from micro-CT, followed by the calculation of γ and σ. In a reactor-scale CFD context, it is envisioned that these geometrical calculations would be performed for a representative distribution of particles as a preprocessing step and would not need to be performed within the effectiveness factor routine. The governing 1-D equation (Eq. (4-12)) was then solved numerically for Y¸ and the effectiveness factor calculated by numerical integration

$$\eta_{1D-GC} = (1+\sigma)\int_0^1 r(Y) z^{\sigma} dz \qquad (4-19)$$

For the 1D–GCΓ model [69] (the variant of the model more appropriate at high Thiele modulus), the shape factor, σ, is obtained from

$$\sigma = \frac{\Gamma}{1-\Gamma} \qquad (4-20)$$

where the geometric parameter, Γ, requires integration of the local principal radii of curvature over the particle's smooth interfacial area and its non-smooth edges, *W*, if present [142]

$$\Gamma = \frac{l}{S_{mps,interface}}\left(\iint \left(\frac{1}{R_a}+\frac{1}{R_b}\right) dS_{mps,interface} + \int_W \mathcal{H} dW\right) \qquad (4-21)$$

where R_a and R_b are the local principal radii of curvature on the particle's interfacial area and the non-smooth edge term, $\mathcal{H}$, is zero for naturally occurring char particles. For each real three-dimensional particle, R_a and R_b were calculated using COMSOL. The governing 1-D equation (Eq. (4-12)) was again solved numerically for Y¸ and the effectiveness factor calculated by numerical integration (Eq. (4-19)). The 1D–GC model parameters calculated for each particle are provided in the Appendix.

The 1D–VD model [69] employs a variable diffusivity along a single coordinate direction, *x*.

$$D_{eff}(x) = D_{eff}\ \Theta(x) \qquad (4-22)$$

where

$$\Theta(x) = \exp(C_1 x + C_2 x^{\alpha}) \qquad (4-23)$$

The model requires three parameters (C_1, C_2 and α) which are chosen such that the effectiveness factor matches the first three terms (including the zeroth order term) of the low modulus series expansion and the first two terms (including the zeroth order term) of the high modulus expansion [141]. In practice, the model's three parameters require the solution of Poisson's equation for *G* on the particle's surface (Eq. (4-17)) to obtain γ from Eq. (4-16) and β from

$$\beta = \frac{\iiint G^2 dV_{mps}}{V_{mps}} \qquad (4-24)$$

as well as the integration of R_a and R_b over the particle's smooth surface and non-smooth "edges" angles (to obtain Γ from Eq. (4-21)). Parameter C_1 is obtained from

$$C_1 = -2\Gamma \qquad (4-25)$$

while C_2 and α are obtained from simultaneously solving nonlinear equations

$$\gamma = \int_0^1 \frac{(1-x)^2}{\Theta(x)} dx \qquad (4-26)$$

$$\beta = \int_0^1 F^2(x) dx \qquad (4-27)$$

where

$$F(x) = \int_0^x \frac{(1-x_0)}{\Theta(x_0)} dx \qquad (4-28)$$

Again, in the context of a reactor-scale CFD code, these calculations would be performed outside of the effectiveness factor routine. The effectiveness factor requires the numerical solution of a 1-D boundary value problem to obtain the concentration profile

$$\frac{d}{dx}\left(\Theta(x)\frac{dY}{dx}\right) = \phi_{1D-VD}^2 \ r(Y) \qquad (4-29)$$

$$Y = 1 \ \text{ at } x = 0 \qquad (4-29a)$$

$$\frac{dY}{dx} = 0 \ \text{ at } x = 1 \qquad (4-29b)$$

where the Thiele modulus is evaluated from Eq. (4-13). The dimensionless Y was then used in integrating the dimensionless reaction rate to yield the effectiveness factor [69]

$$\eta_{1D-VD} = \int_0^1 r(Y)dx \qquad (4-30)$$

4.2.2 Biomass char

Analytical solutions for effectiveness factors of biomass particles have been developed for slabs, spheres (same as coal), and cylinders, and approximations are available for more complex geometries. Due to the fibrous nature of many biomass feedstocks, cylindrical models may be best suited to the shape of many biochars, such as the pine char analyzed here, and are outlined below.

The uniform finite cylinder (UFC) and uniform infinite cylinder (UIC) models treat particles as porous solid cylinders with uniform properties and exclusively subgrid-scale porosity. For the UFC, the geometry is 2-D and the analytical solution for the effectiveness factor, η_{UFC}, involves an infinite series and Bessel functions. the classical expression for the effectiveness factor is [143] based on[144],

$$\eta_{\mathrm{UFC}} = \frac{2I_1(\phi_{UFC})}{\phi_{UFC} I_0(\phi_{UFC})} + 4{\phi_{UFC}}^2 \sum_{n=1}^{\infty} \frac{1}{\alpha_{UFC,n}^2\left({\phi_{UFC}}^2 + \alpha_{UFC,n}^2\right)} \frac{\tanh\left(\lambda_{UFC,n}\right)}{\lambda_{UFC,n}} \qquad (4-31)$$

where $\alpha_{UFC,n}$ are the roots of $J_0\left(\alpha_{UFC,n}\right) = 0$, $\lambda_{UFC,n}$ equals to ${\beta_{bio}}^2(\phi^2 + \alpha_{UFC,n}^2)$.

The Thiele modulus is similar to the uniform sphere model,

$$\phi_{UFC} = R_b \sqrt{\frac{k(1-\theta)}{D_{eff}}} \qquad (4-32)$$

and $I_j(\cdot)$ is the j^{th} order modified Bessel functions of the first kind, the cylinder's aspect ratio, β. The effective diffusivity, D_{eff}, and the intrinsic reaction rate constant, k, which incorporates the subgrid-scale surface area, were evaluated using identical submodels and parameters as used in the pore-resolving simulations for each real particle. The temperature (used in calculating k and D_{eff}) for a particle was obtained from a volume average over the microporous char region from that particle's pore-resolving simulation. (It has been seen in Chapter 3 that temperatures were nearly spatially uniform.) To ensure that the mass, volume, and subgrid-scale surface area of carbon in each 2-D UFC particle with subgrid-scale porosity matches that of its respective 3-D particles with resolved porosity, θ, the term (1- θ) is included in Eq. (4-32), as discussed in[122].

To ensure a faithful comparison with the pore-resolving simulations, the radius, R_b, used in the Thiele modulus for each particle was obtained from morphological measurements based on micro-CT for each specific particle. The particle's total volume is known (from 3-D pore-resolving simulation) and a bounding box method was used to measure its aspect ratio, β_{bio}, defined as the ratio of the bounded length, to the bounded radius. The bounded length is taken directly from the length of the bounding box, and the bounded radius is approximated as half the average of the box's width and depth. Using the expression for the volume of a cylinder, the radius of the UFC particle is then:

$$R_{bio} = \left({V_{Tot}}/{\pi\beta_{bio}}\right)^{\frac{1}{3}} \qquad (4-33)$$

The length of the particle is then given by

$$L_{bio} = \beta_{bio} R_{bio} \qquad (4-34)$$

By using the bounding box method to obtain the dimensionless β_{bio}, with its overestimation in both length and radial directions, and then calculating R_{bio} by matching the volume of the cylinder to that of the real 3-D particle, a more accurate correspondence of geometric parameters is obtained than by taking R_{bio} directly from bounding box measurements.

For the 1-D UIC model, which assumes a cylinder of infinite length, the classical expression for the effectiveness factor, η_{UIC}, involves Bessel functions of the first kind [50] and expresses as

$$\eta_{UIC} = \frac{2I_1(\phi_{UIC})}{\phi I_0(\phi_{UIC})} \qquad (4-35)$$

It depends on the Thiele modulus, ϕ_{UIC}, which is given by the expression in Eq. (4-32). Again, to ensure a faithful comparison with the pore-resolving simulation for each biomass char particle, the radius, R_{bio}, is obtained for each particle from Eq. (4-33) and all subgrid-scale parameters were identical to those used in the pore-resolving simulation.

Analytical solutions for hollow cylinders have also been derived since these geometries are often relevant to catalysis. In contrast to the UFC and UIC, which treat all porosity at the subgrid-scale, hollow cylinder models resolve a large, central cylindrical pore. Based on the work of Gunn[144], Buffham formulated analytical solutions for hollow finite cylinders and hollow infinite cylinders[139]. For a 2-D hollow finite cylinder, an “accessible” inner surface model will be considered (AHFC), such that the interface between the annulus and inner pore is exposed to the same concentration of reactant as the external surface (the same Dirichlet boundary conditions). For the 1-D hollow infinite cylinders, solutions for both accessible (AHIC) and inaccessible (IHIC) inner surfaces are available. For the IHIC, a no-flux boundary condition is applied at the inner surface and a fixed concentration is applied at the outer surface.

For the 2-D AHFC, η_{AHFC} is given by a complex expression involving several Bessel functions [139],

$$
\begin{aligned}
\eta_{AHFC} = \; & \frac{8}{{\phi_{AHFC}}^{2}\left(1-\frac{R_{in}}{R_{out}}^{2}\right)}\left\{\sum_{n=0}^{N_1}\left[\coth(\lambda_n L\phi_{AHFC}) - \operatorname{cosech}(\lambda_n L\phi_{AHFC})\right]\right. \\
& \times\left(\frac{\lambda_n}{\beta_{AFHC,n}^{2}L\phi_{AHFC}} - \frac{1}{\lambda_n L\phi_{AHFC}}\right)\frac{J_0\left(\beta_{AFHC,n}\frac{R_{in}}{R_{out}}\phi_{AHFC}\right) - J_0(\beta_{AFHC,n}\phi_{AHFC})}{J_0\left(\beta_{AFHC,n}\frac{R_{in}}{R_{out}}\phi_{AHFC}\right) + J_0(\beta_{AFHC,n}\phi_{AHFC})} \\
& + \sum_{n=0}^{N_2}\left(\frac{2}{\gamma_n L^2\phi_{AHFC}} - \frac{2\gamma_n\phi_{AHFC}}{\pi^2(2n+1)^2}\right) \\
& \times\frac{\left(-\frac{2}{\gamma_n\phi_{AHFC}}\right) + \frac{R_{in}}{R_{out}}F\left(\gamma_n\phi_{AHFC};\gamma_n\frac{R_{in}}{R_{out}}\phi_{AHFC}\right) + F\left(\gamma_n\frac{R_{in}}{R_{out}}\phi_{AHFC};\gamma_n\phi_{AHFC}\right)}{I_0\left(\gamma_n\frac{R_{in}}{R_{out}}\phi_{AHFC}\right)K_0(\gamma_n\phi_{AHFC}) - I_0(\gamma_n\phi_{AHFC})K_0\left(\gamma_n\frac{R_{in}}{R_{out}}\phi_{AHFC}\right)} \\
& + \sum_{n=N_2+1}^{N_3}\left(\frac{2}{\gamma_n L^2\phi_{AHFC}} - \frac{2\gamma_n\phi_{AHFC}}{\pi^2(2n+1)^2}\right) \\
& \left.\times\left[H\left(\gamma_n\phi_{AHFC},\frac{R_{in}}{R_{out}}\right) - \left(\frac{R_{in}}{R_{out}}+1\right)\right]\right\} \qquad (4-36)
\end{aligned}
$$

Where the $F(\psi_1;\psi_2)$ equals to $K_0(\psi_1)I_1(\psi_2) + I_0(\psi_1)K_1(\psi_2)$, $J_{\mathrm{j}}(\cdot)$ and $Y_{\mathrm{j}}(\cdot)$ are the jth order unmodified Bessel function of the first and second kinds.

The λ_n and γ_n are expressed as

$$
\lambda_n = \sqrt{1+\beta_{AHFC,n}^{2}} \qquad (4-37)
$$

$$
\gamma_n = \sqrt{1+\frac{(2n+1)^2\pi^2}{{L_{bio}}^{2}{\phi_{AHFC}}^{2}}} \qquad (4-38)
$$

The eigenvalues β_n are the values of β satisfying

$$Y_0\left(\beta_{AHFC}\frac{R_{in}}{R_{out}}\varphi\right)J_0(\beta_{AHFC}\phi_{AHFC}) - Y_0(\beta_{AHFC}\phi_{AHFC})J_0\left(\beta_{AHFC}\frac{R_{in}}{R_{out}}\phi_{AHFC}\right) = 0 \quad (4-39)$$

with the initial guess points starting from

$$\beta_{AHFC} = \frac{(n+1)\pi}{\left(1-\frac{R_{in}}{R_{out}}\right)\phi_{AHFC}}, \qquad n = 0,1,2,\dots,N_1 \qquad (4-40)$$

The solution requires specification of inner and outer radii (R_{in} and R_{out}), the cylinder length (L_{bio}), and depends on the nominal Thiele modulus,

$$\phi_{AHFC} = R_{out}\sqrt{\frac{k}{D_{eff}}} \qquad (4-41)$$

To ensure a valid comparison between pore-resolving simulations and the hollow cylinder models, k, and D_{eff} were obtained using identical parameters and models, and the resolved porosity for each particle, θ, was taken directly from volume integration of segmented particle data from micro-CT. The outer radius, R_{out}, equals R_{bio}, which was obtained from measurements of each particle, as shown in Eq. (4-33), L_{bio} was obtained from Eq. (4-34), and R_{in} was calculated such that the core porosity equals the value of θ measured for each biomass char particle, by using

$$R_{in} = R_{out}\theta^{\frac{1}{2}} \qquad (4-42)$$

Effectiveness factors for the 1-D AHIC and IHIC models are given in [139] and involve Bessel functions of the first and second kind, as well as the ratio of R_{in} to R_{out}. The effectiveness factor solution for an infinite hollow cylinder with inaccessible inner surface is

$$\eta_{IHIC} = \frac{2}{\phi_{IHIC}\left(1-\frac{R_{in}}{R_{out}}^{2}\right)} \frac{K_1\left(\frac{R_{in}}{R_{out}}\phi_{IHIC}\right) I_1(\phi_{IHIC}) - I_1\left(\frac{R_{in}}{R_{out}}\phi_{IHIC}\right) K_1(\phi_{IHIC})}{K_1\left(\frac{R_{in}}{R_{out}}\phi_{IHIC}\right) I_0(\phi_{IHIC}) + I_1\left(\frac{R_{in}}{R_{out}}\phi_{IHIC}\right) K_0(\phi_{IHIC})} \quad (4-43)$$

where $K_{\mathrm{j}}(\cdot)$ is the j^{th} order modified Bessel functions of the second kind. The effectiveness factor for an infinite hollow cylinder with accessible inner surface is

$$\begin{aligned}\eta_{AHIC} = {} & \frac{2\left[K_0\left(\frac{R_{in}}{R_{out}}\phi_{AHIC}\right) - K_0(\phi_{AHIC})\right]\left[I_1(\phi_{AHIC}) - \frac{R_{in}}{R_{out}} I_1\left(\frac{R_{in}}{R_{out}}\phi_{AHIC}\right)\right]}{\phi_{AHIC}\left(1-\frac{R_{in}}{R_{out}}^{2}\right)\left[I_0(\phi_{AHIC})K_0\left(\frac{R_{in}}{R_{out}}\phi_{AHIC}\right) - I_0\left(\frac{R_{in}}{R_{out}}\phi_{AHIC}\right)K_0(\phi_{AHIC})\right]} \\ & + \frac{2\left[I_0\left(\frac{R_{in}}{R_{out}}\phi_{AHIC}\right) - I_0(\phi_{AHIC})\right]\left[K_1(\phi_{AHIC}) - \rho K_1\left(\frac{R_{in}}{R_{out}}\phi_{AHIC}\right)\right]}{\phi_{AHIC}\left(1-\frac{R_{in}}{R_{out}}^{2}\right)\left[I_0(\phi_{AHIC})K_0\left(\frac{R_{in}}{R_{out}}\phi_{AHIC}\right) - I_0\left(\frac{R_{in}}{R_{out}}\phi_{AHIC}\right)K_0(\phi_{AHIC})\right]} \quad (4-44)\end{aligned}$$

The nominal Thiele moduli are identical for the AHIC and IHIC models and are given by the expression in Eq (4-41).

To ensure a valid comparison between 3-D pore-resolving simulations and the 1-D AHIC and IHIC models, the resolved core porosity for each particle was set equal to its measured θ. Thus, R_{out} equals R_{bio}, which was obtained from particle-specific measurements and Eq. (4-33) and R_{in} was again calculated using particle-specific θ_{void} and Eq. (4-42). Geometric parameters for all models are in Appendix. Convergence of all series solutions was verified.

4.3 Evaluation of effectiveness factor models using pore-resolving simulations

All parameters (reaction rates, diffusion coefficients, sub-grid scale surface area, etc.) were identical in the 3-D and analytical models for each char particle type (coal or biomass). Temperature-dependent parameters in the analytical model used the volume averaged temperature for each particle calculated from the corresponding 3-D model. Nonetheless, effectiveness factor models solve a single, simplified reaction-diffusion equation, while the 3-D CFD simulation solves conservation equations for mass, momentum, *n*-1 species, and thermal energy conservation. Therefore, to ensure that the 3-D simulation and the effectiveness factor models are comparable and that differences are primarily due to the impacts of real particle geometries, a 3-D pore resolving simulation was run for a uniformly porous sphere at steady state and compared to the analytical solution [137]. The effectiveness factor calculated from the CFD simulation was 0.475, which was in close agreement with the value of 0.486 calculated using the classical effectiveness factor model, indicating that any differences observed for the real char particles are primarily due to their geometrical complexities. The small difference is attributed to the additional physics captured in the CFD simulation, such as the impacts of Stefan flow, the presence of multiple product species, the somewhat spatially varying temperature, etc.

In comparing the pore-resolving simulations and the effectiveness factor models, the particles are arranged on the abscissa in increasing order of the external void fraction (EVF), an indicator which increases as particles transition from cenospheres with isolated resolved pores to more complex and connected pore structures (see Chapter 3 for details).

4.3.1 Coal char

It is first observed in Fig. 4-1 that the true, 3-D effectiveness factors (and thus the reaction rates, via Eq. (4-1)) exhibit a two- to three-fold particle-to-particle variation, despite all particles having the same effective diameter and reacting under the same conditions. This suggests that reactor-scale CFD codes, which often incorporate a distribution of particle sizes, should also consider incorporating a distribution of porosity and/or morphology. It is noted, however, that a size distribution of particles of uniform porosity accounts for mass variations, contributing to the variability seen in Fig. 4-1.

The commonly-used uniform sphere effectiveness factor model treats all porosity as sub-grid scale and overestimates the characteristic diffusion length. In this model, large pores do not act as reactant reservoirs or channels and gas only penetrates the particle by diffusing through uniformly porous solid. As it has been experimentally demonstrated that the uniform sphere method is not suitable for realistic particles with multiple large pores [64], it is not surprising to see, in Fig. 4-1, that the uniform sphere model using the same diffusion model (Section 4.2.1) predicts the lowest effectiveness factor and is the least accurate compared to the 3-D solution. It is noted, that if d_{pore} is calculated using the total porosity, the agreement with the 3-D solution would improve, as the overestimation of the D_{Knud} would offset the error in the characteristic length scale. Another option to reduce the error of the uniform sphere model would be to use a uniform sphere whose radius is smaller and based only on V_{mps}.

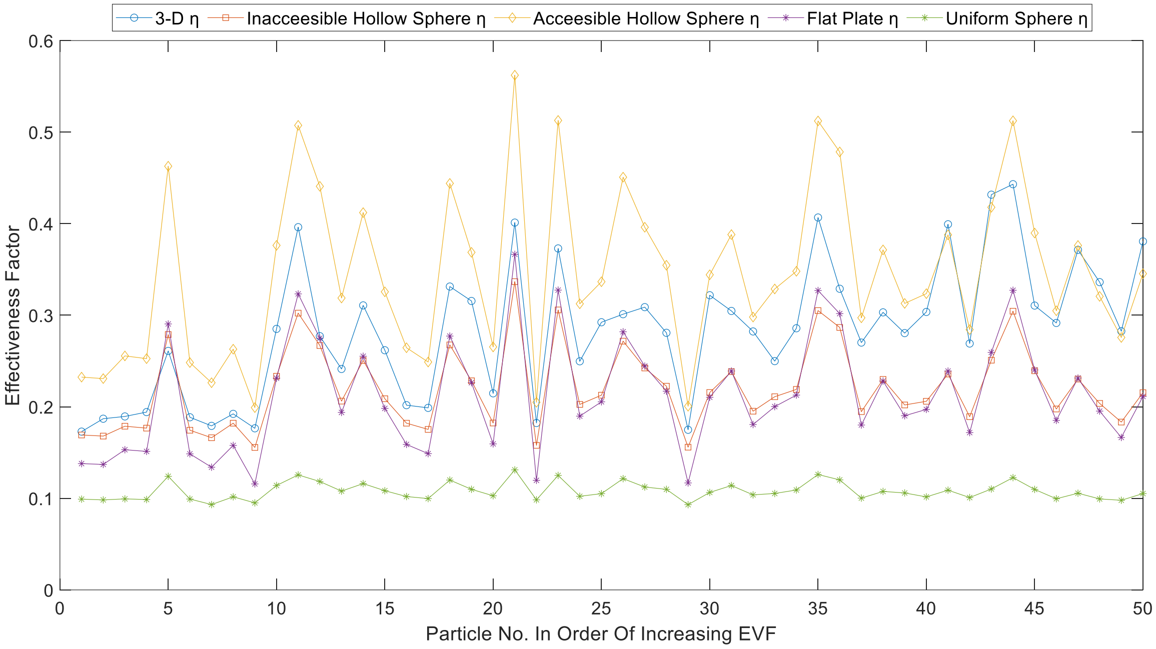

Fig. 4-1 Comparison of effectiveness factors predicted by classical models with effectiveness factor obtained by volume integration of the 3-D, pore-resolving simulation data.

The analytical solutions for inaccessible hollow spheres and flat plates provide reasonable approximations to the exact effectiveness factors for censpherical particles, as seen in Fig. 4-1. These two models account for the presence of large (resolved) pores and incorporate a shorter length-scale for diffusion through the microporous solid (see Eqs. (4-7) and (4-10)). While the two models yield similar predictions, the inaccessible hollow sphere model is more accurate for cenospherical particles, which is the particle type for which these models provide a reasonable prediction (8.4% relative error vs. 21.7% relative error for particles 1-10). This is because a flat plate is a less realistic geometry than a hollow sphere, especially for thicker-walled cenospheres. For all 50 particles, the inaccessible hollow sphere model yields an average relative error of 20.7%, compared with 25.3% for the flat plate model. For the more complex structures on the right of the abscissa, neither the flat plate nor the inaccessible hollow sphere model is accurate, with average errors of 31.3% and 30.0% for particles 30 to 50.

Despite its accuracy for censpheres, the inaccessible hollow sphere model predicts lower effectiveness factors than the true 3-D effectiveness factors for all particle types. This is likely because the central pore in the hollow sphere model is inaccessible and oxygen must first penetrate through the microporous solid region. For most real char particles, however, large pores that extend to the particle surface allow oxygen to channel throughout the particle, as seen in Fig. 3-7(b) in Chapter 3, particularly for the network-type particles. Furthermore, it has been shown previously in a study of a single resolved char particle that large macropores and voids also increase the penetration of reactant into the microporous solid regions to a larger extent than predictions of uniform porosity effective continuum models [44]. This is because the large pore networks present in real char particles act as reservoirs for reactant and decrease the effective length-scale for diffusion within the adjacent microporous solid, which would increase the effectiveness factor. This observation is also corroborated by Fig. 3-8 in Chapter 3.

Due to these reasons, the accessible hollow sphere model with the consistent inner and outer boundary conditions, on the other hand, works well for particles with high EVF value on the right side in Fig. 4-1. Therefore, the accessible hollow sphere model is more accurate for particles with more complex structures, which is the particle type for this model provides a reasonable prediction (7.5% relative error for particles 40-50). For all 50 particles, the accessible hollow sphere model yields an average relative error of 23.7%

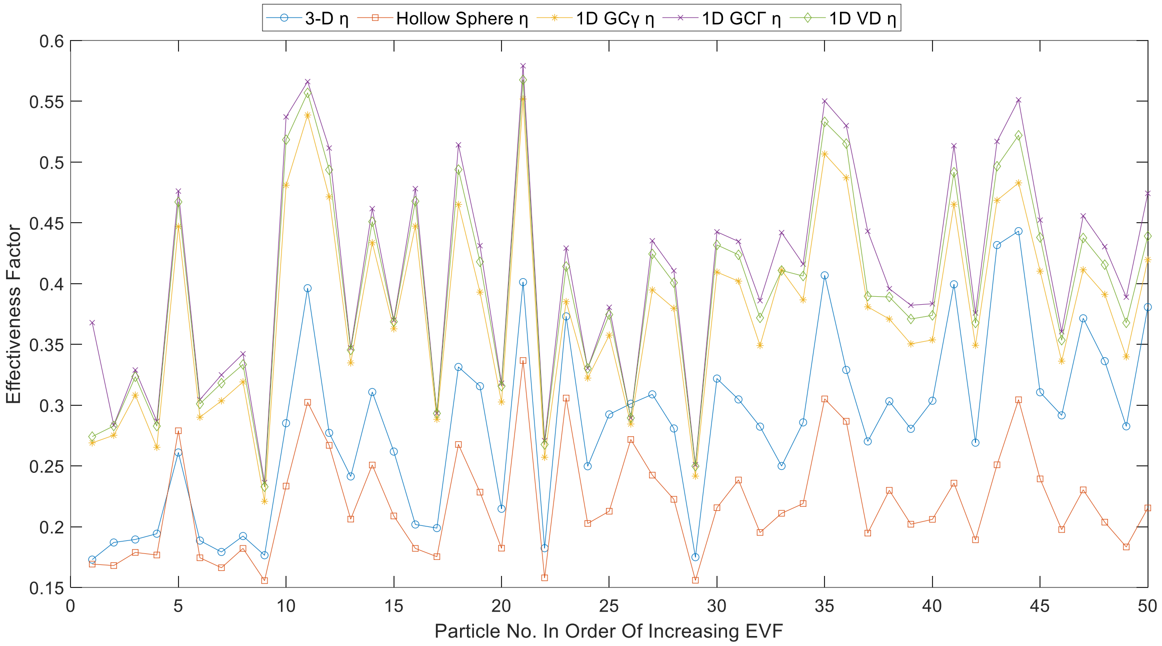

Fig. 4-2 Comparison of effectiveness factors predicted by 1D–GC and 1D–VD models with the hollow sphere model and with effectiveness factor obtained by volume integration of the 3-D, pore-resolving simulation data.

Effectiveness factors calculated using the more complex 1D–GCγ, 1D–GCΓ and 1D–VD models are shown in Fig. 4-2, in which the 3-D, pore-resolving solution and the inaccessible hollow sphere effectiveness factor model are also shown. Several geometric parameters are incorporated in the 1D–GCγ, 1D–GCΓ and 1D–VD models, as described in Section 4.2.1, which led to very high accuracy in catalyst applications [69][140]. It is observed in Fig. 4-2 that the 1D–GCγ, 1D–GCΓ and 1D–VD models produce similar effectiveness factor predictions. Compared to the 1D–GCγ model, which predicts the lowest effectiveness factors, the 1D–VD and 1D–GCΓ models yield an average of 4.8% and 8.4% higher values, respectively. All three models predict higher effectiveness factors than the solutions obtained from the 3-D pore-resolving simulations, with an over-prediction of 55.6% for the most cenospherical particles (particles 1 to 10) and 16.8% for the more connected, network-type particles (particles 40 to 50). Effectiveness factors calculated for each particle are provided in the Appendix.

Similar to accessible hollow sphere model, the 1D–GCγ, 1D–GCΓ and 1D–VD models incorporate several assumptions, noted in Section 4.2.1, which includes the restrictive assumption, for high temperature combustion and gasification applications, of *uniform reactant concentration along the interface* between the microporous solid and external surface/resolved pores (the red/blue and red/green interfaces in Fig. 3-3 in Chapter 3). However, oxygen concentration gradients exist within the resolved pore space, which reduces the interfacial oxygen mole fraction at locations toward the particle centers, as seen in Fig. 3-7(b). This reduction in interfacial oxygen mole fraction results in true (3-D) effectiveness factors which are lower than the predictions of the 1D–GC and 1D–VD models.

Particles with macropores extending to the surface (particles toward the right of the abscissa in Fig. 4-2) have a more uniform oxygen mole fraction on the microporous solid/resolved pore interface than cenospheres, whose inner wall is largely disconnected from the surface. The connected voids and pore networks facilitate the transport of oxygen to the entire pore network, whereas oxygen reaches the inner wall of the most cenospherical particles predominantly by transport through the microporous solid. This leads to better accuracy (smaller overprediction of effectiveness factors) for the hollow sphere model (accessible), 1D–GC and 1D–VD for the more complex, connected void structures than the more cenospherical structures, as seen in Fig. 4-2.

4.3.2 Biomass char

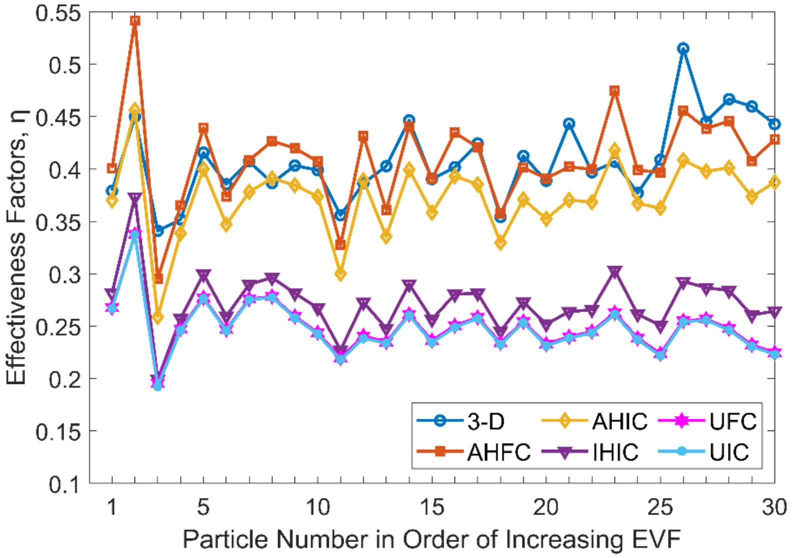

Fig. 4-3 Effectiveness factors for 30 particles calculated by 3-D pore resolving simulation and five analytical models.

Effectiveness factors from 3-D pore-resolving simulations (Eq. (4-1)) for all 30 pine char particles are compared to analytical models (Section 4.2.2) in Fig. 4-4. It is recalled that for each particle, the analytical solutions employed the particle's specific morphological parameters obtained from micro-CT imaging. Particles are arranged on the abscissa by particle number (one to 30) in order of increasing external void fraction, EVF, which is the fraction of the particle's external surface that is penetrated by large pores (or "voids"). EVF was well-correlated with $\eta_{3\text{-}D}$ for coal char particles [122], but neither EVF nor any single measured morphological parameter (e.g., porosity, aspect ratio, surface area, etc.) correlated particularly well with $\eta_{3\text{-}D}$ for these biomass chars. It is noted that although each particle had identical size (total volume), $\eta_{3\text{-}D}$ ranged between 35.4% to 51.5%.

As seen in Fig. 4-3, the UFC and UIC models predict similar effectiveness factors, which is due to the high aspect ratio of the pine char particles. Both models significantly underpredict the "true" effectiveness factors, due to their neglect of the impact of large, connected pores serving as reactant conduits. The uniform models thus overestimate the characteristic diffusion length and the level of diffusion limitations. The relative errors averaged for all particles for the UFC and UIC are 38.6% and 39.0%, respectively.

Based on Fig. 3-10 in Chapter 3, hollow cylinders appear to approximate the morphology of the pine char particles with greater accuracy than uniform cylinders. While the IHIC model severely underpredicts $\eta_{3\text{-}D}$ (average relative error 33.1%) since the inaccessible inner surface forces oxygen to be transported across the entire annular thickness, the AHIC and AHFC models, with accessible inner surfaces, reproduce the effectiveness factors for the pine char particles with better accuracy. These models capture the reduced length-scale for oxygen diffusion, which is now approximately equal to half the annular thickness. Although "fully accessible" models overestimate the level of x_{O2} on the interface between large pores and microporous char based on Fig. 3-10 (which leads to overestimations of η), they also underestimate the interfacial area and overestimate the local thickness of microporous char regions. These two factors would lead to underestimations of η, counteracting the impact of the fully accessible assumption. The average relative errors for the AHIC and AHFC are 9.0% and 6.0%, respectively. In contrast to mm-scale particles with many parallel pores that experience diffusion primarily in the axial direction (i.e., slab behavior)[115], these smaller, µm-scale char particles contain fewer, more irregular large pores, experience significant radial diffusion (Fig. 3-10), and are more accurately modeled as hollow cylinders (Fig. 4-3).

4.4 Conclusions

Because reactor-scale CFD simulations require analytical models that are accurate as well as computationally efficient for the thousands of tracked char particles, predictions of effectiveness factor models have been compared with the effectiveness factors calculated from the 3-D pore-resolving simulations. For coal char particles, effectiveness factors predicted from the classical uniform sphere model, a classical flat plate model, hollow sphere models (inaccessible and accessible inner surfaces), and the 1D–GC and 1D–VD models were assessed. The commonly used uniform sphere model treats all pores as sub-grid-scale and results in effectiveness factors which are too low for all particle types. The hollow sphere model (inaccessible) produced good agreement (better than the flat plate model) with the pore-resolving simulation for char particles which were cenospherical, but was inaccurate for particles with more connected pore structures. Conversely, the hollow sphere model (accessible) can provide accurate prediction for coal char particles which the resolved pores connect to outer surface with enhanced capability. Although the 1D–GC and 1D–VD models account for the three-dimensional morphology of real particles, they overpredicted the effectiveness factors for all particle types due to their assumption of uniform reactant concentration along the entire solid/resolved pore *interface*. This assumption is particularly inaccurate for cenospheres with minimal connection between the central resolved pore and external surface.

Zone II combustion of cenospherical coal char can be adequately modeled in a one-dimensional context using the inaccessible hollow sphere effectiveness factor approach. Char particles with higher connectivity are adequately-modeled by the accessible hollow sphere model. However, transitional particles require either a new effectiveness factor approach, a modification of the 1D–GC or 1D–VD models to account for non-uniform interface concentration, or perhaps a modification of bimodal (“macro-micropore”) effectiveness factor models [70] to account for “macropores” that cannot be treated at the sub-grid-scale.

For biomass char particles, uniform cylindrical effectiveness factor models, which are often used as particle-scale models in reactor-scale codes, significantly underpredicted the effectiveness factors compared to results from the geometrically faithful simulations. Hollow cylinder effectiveness factor models with fully accessible inner surfaces exhibited better agreement with results for the real particles, although these models incorporate assumptions with counterbalancing inaccuracies.

In conclusion, commonly used uniform sphere and cylinder models significantly underpredict effectiveness factors, which will likely reduce the accuracy of reactor-scale CFD simulations. Reactor-scale CFD codes, which often employ a distribution of particle sizes, should also include a distribution of morphologies and a corresponding distribution of effectiveness factor models, given the variation of reaction rates between particles of the same size reacting under the same conditions and the demonstrated impacts of morphology on analytical effectiveness factor predictions.

Chapter 5. Particle Classification Based on Real 3-D Char Particle and Machine Learning Algorithms for Effectiveness Factor Selection

To facilitate reactor-scale CFD codes employing a distribution of char particles with corresponding distribution of effectiveness factor models, a rapid and accurate *classification system* is needed. Therefore, in this chapter, machine learning (ML) approaches are introduced (Section 5.1) and later applied to classify every particle in a distribution of bituminous char according to its expected combustion behaviors, using its 3-D morphology as input. In Section 5.2, the procedure of measuring morphological parameters (porosity, volume, etc.) for each particle from its 3-D structure are discussed, as well the data acquisition for classifier training. Basic principles of the machine learning algorithms are explained in Section 5.3, followed by results and discussion (Section 5.4) and conclusions (Section 5.5).

5.1 Introduction

Whereas previous approaches have classified particles solely according to their morphology, with an assumed correspondence to combustion behavior [145,73,102], the first novelty of the present approach is that it uses ML to classify bituminous char particles according to their combustion behaviors, using morphology as input. Furthermore, while previous approaches have employed 2-D morphological measurements (Section 2.4) based on particle cross-sections (discussed in Chapter 6), the second novelty of the present approach is that the morphological parameters used for classification are obtained in 3-D, using a single high-resolution micro-CT scan of a char particle distribution.

At the reactor scale, boilers, furnaces, and gasifiers always contain a distribution of char particles with a distribution of morphologies. It has been shown experimentally that real char particles cannot be treated as homogeneous, porous spheres and that variations in char particle morphology affect conversion under zone II conditions [64,43,97]. As seen in Chapter 4, reactor-scale CFD codes should incorporate a distribution of particle morphologies, with a corresponding distribution of combustion/gasification models, to improve their predictive capabilities.

To facilitate the use of realistic morphology distributions and associated distributions of particle-scale combustion/gasification models and parameters in reactor-scale CFD codes, char particles formed under relevant conditions must be analyzed and classified. A classification system that is based on the real combustion behaviors should be developed to assign related effectiveness factor models to certain particle groups for reactor-scale CFD, based on the findings from Chapters 3 and 4.

Machine learning (ML) refers to a system that can understand and acquire knowledge from observed data by using computational algorithms to perform a set of tasks [146,147]. This approach has received more attention recently in the solid fuel industry using classification, for prediction of gasification, combustion, and pyrolysis behaviors due to its efficiency to reduce the complexity of CFD simulation that usually describes complex processes. Solely from a biomass perspective, the number of academic publications increases from around ten (2000 - 2002) to over 350 (2018 - 2020) [148].

5.1.1 Support vector machines

Support vector machines (SVM) [149] are commonly used to solve binary classification problems, by transforming a dataset to a higher dimension with a selected kernel function to find the maximum distance to the surrounding data points on a hyperplane for data separation. This transformation can be approached by a calculation using the kernel function [150]. Fig. 5-1 illustrates an SVM classification of two nonlinear separable classes. The solid blue line indicates the hyperplane with the maximum-margin between two dashed lines that is found by the algorithm. They are trained to divide the data into different groups (classes) such that the distance between the hyperplane and the nearest data point from each of the two classes is maximized. The data points are "support vectors."

Depending on the selected kernel, SVMs are capable of dealing with both linear and nonlinear problems by finding the maximum margin on the hyperplane. The form of general nonlinear support vector machine function with kernel function is,

$$f(\boldsymbol{x}) = \beta_{SVM} + \sum_{i \in A} \alpha_{SVM,i} K(\boldsymbol{x}, x_i) \qquad (5-1)$$

where $\boldsymbol{x}$ is the input vector, β_{SVM} and $\alpha_{SVM,i}$ are the constant parameters, A is the collection of indices of all support data points and $K(\boldsymbol{x}, x_i)$ is the kernel function. Due to its ability to capture nonlinear relationships, the Radial Based Function (RBF) kernel function is usually employed while involving nonlinear data [151]. The RBF function has the form

$$K(x_i, x_{i'}) = \exp\left(-\gamma_{SVM} \sum_{j=1}^{p} \left(x_{ij} - x_{i'j}\right)^2\right) \qquad (5-2)$$

where γ is the width parameter.

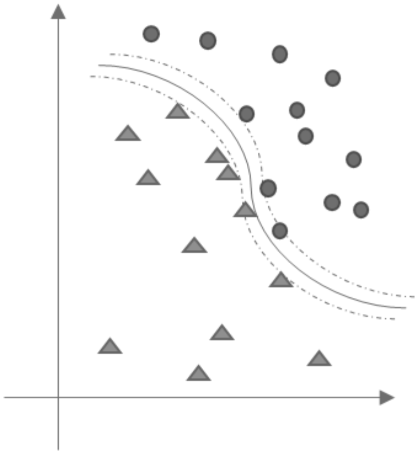

Fig. 5-1 SVM classification using two nonlinear classes.

5.1.2 Random forest

Random Forest (RF) classifiers [152] are based on a number of decision trees to form an ensemble learning network, which differs from other machine learning algorithms. Unlike traditional decision tree methods that faces high variance and overfitting issues, RF employs bootstrap aggregation (bagging method). The basic idea of the RF method is 1) resampling the training data set multiple times to form bootstrapped sample sets each time, 2) for each bootstrapped sample set, a decision tree is trained, and 3) based on the result from all decision trees, the final output is decided by majority voting for classification. Since the original data set has been resampled, data imbalance is no longer an issue in constructing the decision tree. In majority voting, the final prediction is the most frequent class among the trained decision trees with different bootstrapped sample sets. Figure 5-2 shows the structure of the RF algorithm.

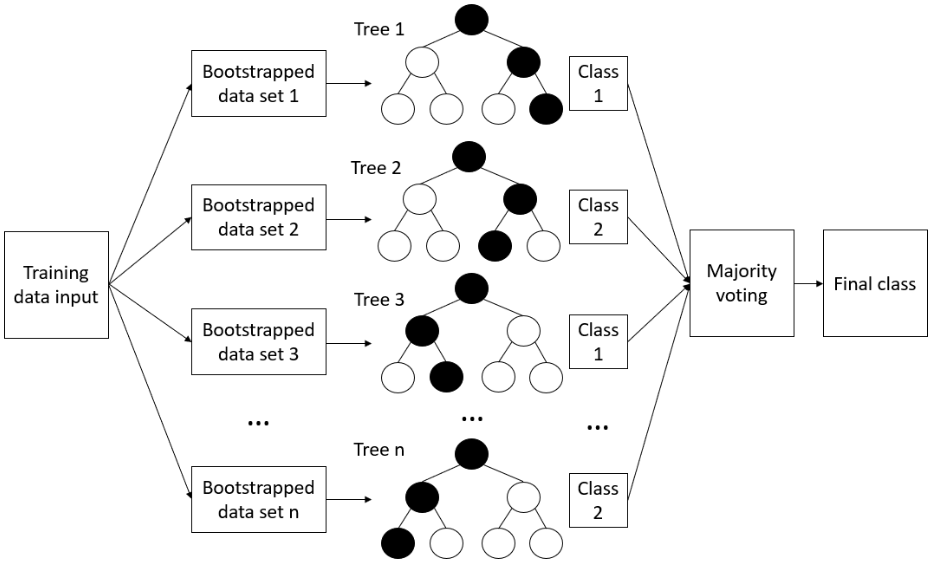

Fig. 5-2 The structure of the RF algorithm.

For purposes of classification, standard support vector machine (SVM) and random forest (RF) classifiers were implemented using MATLAB in the present study. SVM and RF algorithms for classification are attractive for use with limited data compared to the data set size required in neural network modeling [153,154]. The classification algorithms employ 3-D morphology data obtained from micro-CT imaging as input and 3-D pore-resolving combustion simulations to assign class labels during the training procedure.

5.2 Data acquisition and classifier training

5.2.1 Morphological parameters

Eight morphological parameters were measured in 3-D from the micro-CT data for each particle: the internal surface area (red/blue interfacial area in Fig. 3-3), external surface area (red/green interfacial area in Fig. 3-3), the contour ratio (discussed below), the resolved porosity, the solid volume, and three “void position indices” (VP_L, VP_W, VP_H).

The internal and external surface areas are calculated by surface integration over the interfacial areas illustrated in Fig. 3-3 (red/blue interface and red/green interface, respectively). The solid volume is calculated by volume integration over all red regions in Fig. 3-3, and the resolved porosity is the ratio of resolved pores volume (blue region) to the total volume (red and blue region).

During the segmentation process, the contour ratio is measured by contouring the solid particle (finding its boundaries) as shown in Fig. 5-3 and calculating the ratio of the number of voxels associated with the contoured (surface) region to the number of voxels in the solid particle’s volume. This surface-to-volume ratio provides a measure of the particle’s average “thickness” [105], with thicker particles associated with lower contour ratios.

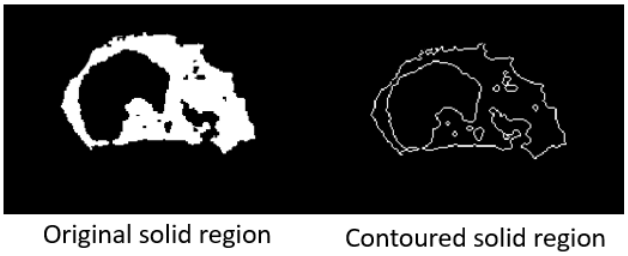

Fig. 5-3 Illustration of the contour ratio in two dimensions.

The void position indices are defined as ratios of particle length to the resolved pore (“void”) length (VP_L), and the analogous ratios for the width (VP_W) and height (VP_H). These ratios are measured by creating a bounding box - the smallest rectangular cuboid that can contain the volumes of the particle and the resolved pore regions, individually. The length dimension is the longest dimension of the bounding box. Larger *VP* values imply that the resolved pores extend closer to the particle's external surface.

5.2.2 Classification and feature selection

As discussed in Chapter 4, cenospherical coal char can be adequately modeled in a one-dimensional context using the inaccessible hollow sphere effectiveness factor approach. More complex network-type char particles with higher connectivity are satisfied by the accessible hollow sphere model. However, in the context of reactor-sale CFD codes, effectiveness factor models are integrated with boundary layer diffusion models to account the effect of diffusion limitations outside of the particle in addition to internal diffusion limitations. This is because char particles in a CFD cell have known boundary conditions for the far-field oxygen concentration, not the particle surface oxygen concentration. In this case, an "overall effectiveness factor" is employed.

The overall effectiveness factor, $\eta_{overall}$, represents the ratio of the actual, zone II, diffusion-limited reaction rate integrated over a particle's microporous solid volume, *V*, to the ideal reaction rate in the absence of any diffusion limitations in the particle's microporous solid *or in the surrounding gas boundary layer* [155]. The true (3-D) overall effectiveness factor is calculated for each particle using volume integration of data from the pore-resolving CFD simulations

$$\eta_{overall} = \frac{\iiint R_{actual} dV}{\iiint R_{ideal,\infty} dV} \qquad (5-3)$$

The actual reaction rate (R_{actual}) is calculated using the local values of reactant partial pressure, which varies due to intraparticle diffusion limitations, while the ideal reaction rate ($R_{ideal,\infty}$) employs a spatially uniform reactant partial pressure equal to that at the *far-field boundary*.

As discussed, the classically defined effectiveness factor, η, represents the ratio of the actual, zone II, diffusion-limited reaction rate integrated over a particle's solid volume, to the ideal reaction rate in the absence of any diffusion limitations within the particle [50]. Thus, in calculating the ideal reaction rate, the (classical) effectiveness factor employs a spatially uniform reactant partial pressure equal to the (assumed uniform) partial pressure at the particle's *surface*

$$\eta = \frac{\iiint R_{actual} dV}{\iiint R_{ideal,s} dV} \qquad (5-4)$$

The effectiveness factor, η, has been shown to be sensitive to particle morphology [64][122]. Combining Eqs. (5-3) and (5-4), the overall effectiveness factor, $\eta_{overall}$, is related to the (classically defined) effectiveness factor, η, by

$$\eta_{overall-3D} = \eta \, \frac{\iiint R_{ideal,s} dV}{\iiint R_{ideal,\infty} dV} \qquad (5-5A)$$

By eliminating common terms in $R_{ideal,s}$ and $R_{ideal,\infty}$, the expression for the overall effectiveness factor can also be written (for a first-order oxidation reaction) as

$$\eta_{overall-3D} = \eta \, \frac{\frac{1}{S} \iint P_{O2,s} dS}{P_{O2,\infty}} \qquad (5-5B)$$

where the numerator represents the surface weighted average oxygen pressure on the particle external surface and $P_{O2,\infty}$ is the oxygen pressure at the far field boundary.

To calculate an overall effectiveness factor using a analytical combustion model, $\eta_{overall-1D}$, a simple diffusion model is typically used [36,156] to calculate the partial pressure of reactant at the particle surface, $P_{O2,s}$, which differs from its partial pressure at the outer edge of the boundary layer, $P_{O2,\infty}$. Using Eq. (5-5B) and the ideal gas relation for partial pressure to mole fraction, the analytical overall effectiveness factor can be expressed in term of partial pressures (for a first-order reaction) as

$$\eta_{overall-1D} = \eta_{1D} \frac{P_{O2,s}}{P_{O2,\infty}} \qquad (5-6)$$

where η_{1D} is the effectiveness factor calculated from the analytical models outlined in Chapter 4. The partial pressure on the particle surface is found by equating the reaction rate and the diffusion rate at the particle surface (the subscript “ext” indicates that this calculation is typically done on a per unit external surface area basis) [34]

$$R_{reaction,ext} = R_{diff,ext} \qquad (5-7)$$

$R_{reaction,ext}$ of Eq. (5-7) represents the actual, diffusion-limited reaction rate in the particle per unit interfacial area, given by [36]

$$R_{reaction,ext} = \eta_{1D} \frac{LSkM_cP_s}{\nu R_u T_p} \qquad (5-8)$$

where M_c is the molar mass of carbon, L is the particle’s characteristic length, defined as the particle’s microporous volume to its interfacial area (red/blue and red/green interface in Fig. 3), ν is the stoichiometric coefficient, R_u is the gas constant, and T_p is the particle temperature. As in Chapter 4, S and k represent the particle's sub-grid-scale surface area, and the associated intrinsic reaction rate coefficient.

For right hand side of Eq. (5-7), classical 1-D boundary layer diffusion models are typically applied [36], and the rate of diffusion to the particle's external surface is given by

$$R_{diff,ext} = \frac{2D_m M_c}{d_p R_u T_m \nu}(P_\infty - P_s) \qquad (5-9)$$

where, d_p is particle diameter which equals to $2R_{out}$, D_m is the (mixture averaged) reactant diffusion coefficient in the gas boundary layer, T_m is the film temperature defined as $T_m = \frac{T_p + T_b}{2}$ [157]and T_b is the bulk temperature.

For a particle of a given size and porosity, $\eta_{overall-acc-hs}$ will exceed $\eta_{overall-inacc-hs}$ because of the enhanced gas penetration represented in the boundary conditions used in deriving η_{acc-hs}. To distinguish between accessible and inaccessible hollow sphere behavior for real 3-D char particles, an accessibility indicator, *AI*, is defined as

$$AI = \frac{\eta_{overall-3D} - \eta_{overall-inacc-hs}}{\eta_{overall-acc-hs} - \eta_{overall-inacc-hs}} \qquad (5-10)$$

The particles behave as increasingly accessible cenospheres as *AI* approaches (or in rare cases, exceeds) unity and behave as increasingly inaccessible cenospheres as *AI* approaches zero.

To train the SVM and RF classifiers, morphological parameters were calculated using manual segmentation and image analysis, as described in Chapter 6. In total, 150 particles and their corresponding independent variables (the eight morphological parameters) were used to train and test the SVM and RF classifiers. The ratio of the training set to the test set was 4:1.

Prior to the ML training, it is noted that each morphological parameter has a different scale of numerical values. The porosity, for example, is around 0.3 but the solid volume of particle is around 4^{-13} m. It has been noted [158] that the value of the independent features can result in a larger weight for some features during regression and classification. Therefore, it is necessary to scale the values of each feature into a comparable range, to find the real impact of various features. One common method is to calculate the means and standard deviations of each variable and transform each input using a linear transformation,

$$X_i = \frac{(x_i - \mu_{mean})}{\sigma_{mean}} \qquad (5-11)$$

where the x_i is the original input value for each feature along with corresponding means, μ, and standard deviations, σ. All morphological parameters were standardized using this approach.

The char particles were separated into two morphological classes based on their *combustion behavior*. Class labels were assigned using the calculation of *AI* for each particle from the 3-D pore-resolving simulations. Particles with *AI*<0.5 were labeled inaccessible cenospheres, while particles with *AI* ≥ 0.5 were labeled accessible cenospheres. The classifiers were then trained to predict the combustion behavior class of the particles using 3-D morphological features.

The accuracy (ACC_{train}) of the classifiers was evaluated by 10-fold cross-validation during the training, which represents the fraction of candidate particles in the training set that were correctly classified. The basic ideal of 10-fold cross-validation is that the training data set is first randomly divided into 10 sub data sets with the same size, of which nine sub datasets are used to train the model and the rest one dataset is used as "test" dataset to evaluate the performance of model. This process is repeated ten times (10-fold). The model among those 10-time repeating with the highest accuracy is exported as the final trained model.

The confusion matrix was then used to assess the performance of classifier for the test set using true positive (TP), false negative (FN), false positive (FP), and true negative (TN) predictions. The test set prediction accuracy for each classifier was calculated as

$$ACC_{test} = 1 - \frac{FP + FN}{TP + TN + FP + FN} \qquad (5-12)$$

To test the stability of the classifiers, the data set was randomly resampled ten times (repeated cross-validation) and separated into training and test sets. Each time, the classifiers were trained and evaluated. The final performance of the classifiers was assessed using the averaged confusion matrix (containing averaged TP, FN, FP, and TN obtained from each repetition). The ACC_{train} and ACC_{test} presented in next section have been averaged.

Feature selection was used to eliminate unnecessary input features, to simplify the classifier, to reduce training time, and to reduce potential biases caused by morphological parameter quantification. Since a backward feature selection algorithm can capture interacting features, the backward wrapper method [159] was used to remove irrelevant and redundant features which have negative contributions to the classification performance. During the procedure, the algorithm was started with all features, and subsets of features were created by eliminating those which decrease the accuracy at each iteration. Ten-fold cross-validation was also employed for feature selection.

5.3 Results and discussions

Overall effectiveness factors were obtained from the 3-D pore-resolving simulation and compared to analytical overall effectiveness factor for 150 coal char particles to evaluate the inaccessible and accessible hollow sphere models. As shown in Fig. 5-4. Particles are arranged on the abscissa in order of increasing ratio of the averaged oxygen mole fraction on the internal surface to the averaged oxygen mole fraction on the external surface (“O2 ratio"), which serves as a proxy for the level of enhanced diffusion elicited by the surface-accessible pores. The average relative error for the inaccessible hollow sphere model applied to all particles with AI < 0.5 is 11.6%, and the average relative error for the accessible hollow sphere model applied to all particles with AI ≥ 0.5 is 8.8%. It is noted that the average relative error using the inaccessible hollow sphere model increases to 34.0% for the 30 particles with the highest O_2 ratio and the average relative error using the accessible hollow sphere model increases to 23.2% for the 30 particles with the lowest O_2 ratio, indicating the importance of morphological classification for accurate combustion modeling. Furthermore, the inaccessible and accessible hollow sphere models generally bound the behavior of the highly porous bituminous char particles, making them appropriate choices for binary classification. However, a third effectiveness factor model could potentially be developed to increase the accuracy for the transitional cenospherical particles, in which case a multi-class classification scheme would be necessary.

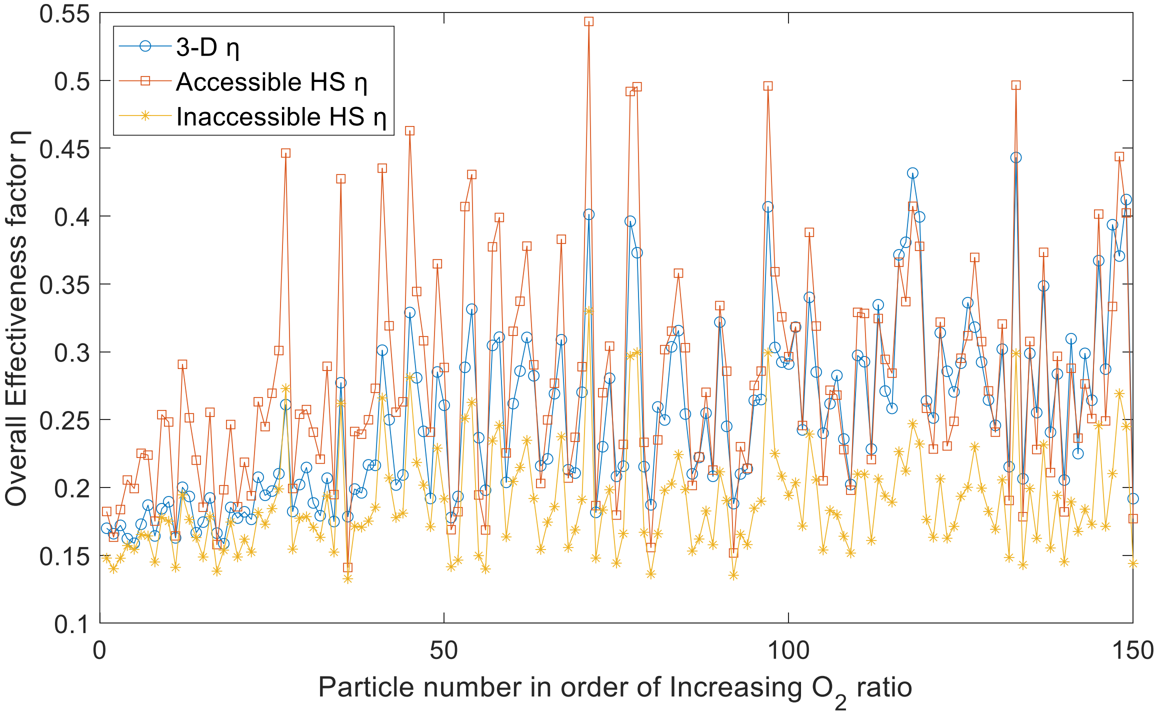

Fig. 5-4 Comparison of overall effectiveness factors predicted by accessible and inaccessible hollow sphere models with the overall effectiveness factors obtained by volume integration of the 3-D, pore-resolving simulation.

Following feature selection, five morphological parameters remained: the external surface area, contour ratio, resolved porosity, solid volume, and VP_L. To first focus on the performance of the classifiers without the confounding effects of the performance the automated image analysis routine, results are presented in Tables 5-1 and 5-2 for the SVM and RF classifiers, respectively, using manually measured morphological parameters. After 10-fold repeated cross-validation to train the SVM and RF classifiers using 80% of total particles, the average training accuracy, ACC_{train}, for the SVM and RF classifier were 0.735 ± 0.019 and 0.740 ± 0.027, respectively. The remaining 20% of particles were used as a test set to examine classifier performance and robustness. It is observed that both classifiers have a test accuracy greater than 70%, although the RF classifier has a slightly higher averaged accuracy in both training and testing sets. Both classifiers have higher uncertainty in ACC_{test} than ACC_{train}, which may be caused by an unbalanced sample, due to the samples being selected randomly and divided into test and training sets each time, or by the sample size.

The averaged confusion matrices are also shown in Tables 1 and 2. Because the particle distribution contains more accessible particles than inaccessible particles, as seen in the Tables 5-1 and 5-2, the Matthews correlation coefficient (MCC) which is used to evaluate the quality of binary classification system [160] is also calculated. Both true and false positives and negatives are considered in MCC as a balanced measurement for the classes with very different sizes. A coefficient near 1 indicates a perfect classification, 0 means no better than random prediction, and -1 represents that the prediction is against the observation. The MCC for the SVM and RF classifier were 0.320 and 0.345, respectively, indicating that although the sample is unbalanced and the classifiers have been trained to identify more particles as accessible by default, the RF and SVM classifiers still improve classification performance compared to random predictions (MCC of zero). This is particularly the case for the RF classifier, which performs better than the SVM for inaccessible particles.

It is observed that the accessible and inaccessible effectiveness factor models provide similar accuracy for transitional particles, which have *AI* near 0.5. This stems from the fact that the classification employed for char particles is based on a continuous quantitative metric rather than qualitative differences that can be unambiguously classified. It is therefore not unexpected that transitional particles would cause difficulty for the classifiers. The mean *AI* of misclassified particles in the test group for the SVM and RF classifiers is 0.44 ± 0.26 and 0.48 ± 0.25, respectively. This indicates that classification errors occur primarily for transitional particles, with an *AI* range of 0.3 to 0.7.

Table 5-1 Averaged confusion matrix for SVM classifier.

		Predicted classes	
		Accessible-type particle	Inaccessible-type particle
Measured classes	Accessible-type particle	TP: 17.9	FN: 2.6
	Inaccessible-type particle	FP: 5.6	TN: 3.9
ACC_{test}		0.727 ± 0.048	
ACC_{train}		0.735 ± 0.019	
MCC		0.320	

Table 5-2 Averaged confusion matrix for RF classifier.

		Predicted classes	
		Accessible-type particle	Inaccessible-type particle
Measured classes	Accessible-type particle	TP: 17.6	FN: 3.1
	Inaccessible-type particle	FP: 4.9	TN: 4.4
ACC_{test}		0.733 ± 0.068	
ACC_{train}		0.740 ± 0.027	
MCC		0.345	

Figure 5-5(a) shows the accuracy of the classifiers with transitional particles eliminated from the input data set, using definitions of transitional based on *AI* ranges of 0.40-0.60, 0.35-0.65, and 0.3-0.7. The classifiers were re-trained with each new data set under the same conditions described above. With increasing numbers of transitional particles removed, the average ACC_{test} for the RF classifier increases from 0.733 to 0.853 and the average ACC_{test} for the SVM classifier increases from 0.727 to 0.847. It is noted that even when the AI drop-off range is 0.3-0.7, there are still 104 particles remaining in the distribution. This indicates that the classifiers reliably predict combustion behavior for most of the highly porous bituminous coal char particles based on morphology, but that a multi-class classification approach could improve the accuracy for transitional particles.

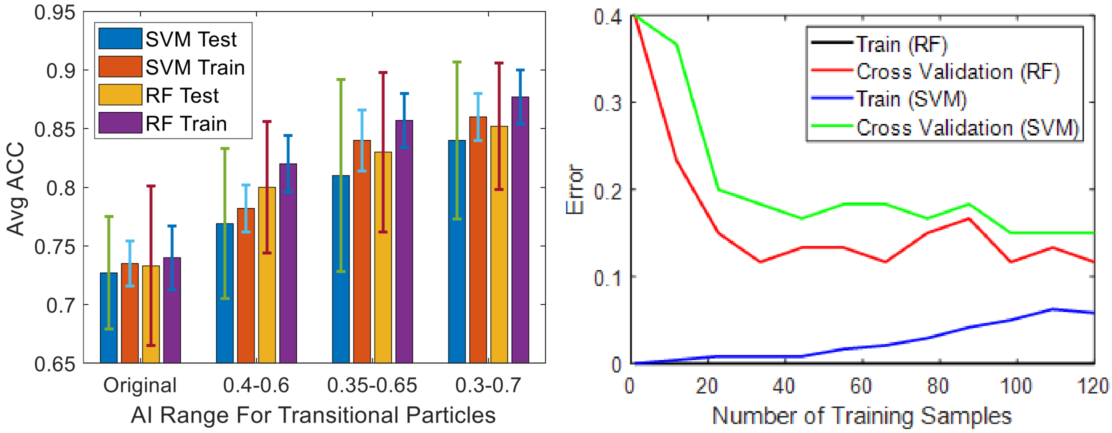

Fig. 5-5 Average accuracy with (a) transitional data removed (left) and (b) as a function of sample size for the RF algorithm.

Unlike deep learning algorithms, machine learning exhibits a peak in performance with increasing data size [161]. Figure 5-5(b) shows the sample size sensitivity for RF and SVM average accuracy, ACC_{test}. Ideally, the training error and cross validation error should be identical with increased samples size and remain the same no matter how much data is added thereafter. This means the “variance” (the gap between “train error” line and “cross validation” line) should be small, eventually. However, the variances here for both SVM and RF algorithms are still high between their validation error and training error. This indicates that the performance of the classifiers could be further improved with a larger sample size.

5.4 Conclusions

To facilitate modeling distributions of porous char particles in reactor-scale CFD codes, machine learning algorithms have been developed to classify bituminous char particles according to their expected zone II combustion behaviors. In contrast to existing approaches that classify particles based only on their morphology and employ 2-D quantification methods, the approach outlined here uses machine learning to classify particles according to their combustion behaviors, using 3-D morphology from micro-CT as input and 3-D pore-resolving CFD simulations to assign the class labels during the training.

For the highly porous coal char particles examined here, both inaccessible and accessible hollow sphere effectiveness factor models accurately represent (and bound) the behavior of most particles in the distribution. However, a more complex model could improve the representation of transitional particles. Each of the 150 char particles in the distribution was classified as behaving either as an accessible or inaccessible hollow sphere based on its zone II combustion behaviors simulated with the geometrically-faithful pore-resolving simulation.

Support vector machine and RF classifiers for the highly porous char particles were then trained using data from the 3-D pore-resolving simulations to classify particles according to their combustion behavior using 3-D morphological parameters obtained from micro-CT as input. The accuracy of the pre-trained classifiers was 0.740 ± 0.027 for the RF algorithm and 0.734 ± 0.019 for the SVM, using manually measured morphological parameters, and the MCC was 0.320 and 0.345, respectively. The misclassified particles were generally transitional particles which exhibited intermediate zone II combustion behavior between that of accessible and inaccessible hollow spheres, indicating that a multi-class classifier could improve performance.

Chapter 6. Particle Morphological Parameters Quantification based on 3-D Automated Image Analysis for Effectiveness Factor Model Calculation and Particle Classification

In Chapter 5, a classification system to choose an appropriate effectiveness factor model for every particle in a distribution was developed using 3-D morphological parameters as input, and for which the classifiers were trained with labels from the 3-D pore-resolving simulations. To allow others to use the pre-trained classifiers without having to do the tedious work of manual 3-D morphology measurements, an automated image analysis routine is developed in this chapter. It is noted that the measured morphological parameters (e.g., particle porosity) would *not only* be used in classification, but would also serve as parameters in the effectiveness factor models.

Conventional methods to measure particle morphological parameters are briefly summarized in Section 6.1 along with their limitations, which were discussed in the Chapter 2. Some basic image process techniques that are typically used to segment objects from obtained images are also introduced in Section 6.1. The workflow for a 3-D automated image analysis system integrated with a classification process and used to predict effectiveness factor models for use in reactor-scale codes is described at the end of Section 6.1. In Section 6.2, the detailed steps of automated 3-D structure construction and parameters measurement are explained. The accuracy of the 3-D automated image analysis system is assessed by comparing the morphological parameters obtained from the manual process and automated process in Section 6.3. The advantages of proposed automated images analysis system to measure the parameters and its future works are highlighted in the Section 6.4.

6.1 Introduction

From Chapter 2, it is known that char morphology distributions are currently quantified by embedding a distribution of particles in resin, slicing it to obtain 2-D cross-sections, and examining the cross-section using microscopy [99]. The resolved porosity is estimated for each particle in the distribution by calculating the fraction of the cross-sectional *area* occupied by visible pores to its total cross-sectional area. Wall thickness and other properties are similarly measured from 2-D cross-sections [104]. *Automated* techniques have been developed to efficiently quantify morphological properties for a large distribution of particles based on 2-D cross sections [104,106,145].

However, morphology measurements based upon 2-D cross-sections can produce results that are quite different compared to 3-D techniques, as illustrated by two cross-sections of the same particle shown in Fig. 6-1, which imply very different resolved porosities. More importantly, in a statistical sense (for a distribution of particles), 2-D quantification methods produce biased results, as shown by a comparison of 2-D and 3-D porosity measurements for a distribution of coal char particles (Ref. [100], see Fig. 12 therein). This implies that 2-D quantification methods will not be able to accurately classify distributions of particle-scale combustion behavior.

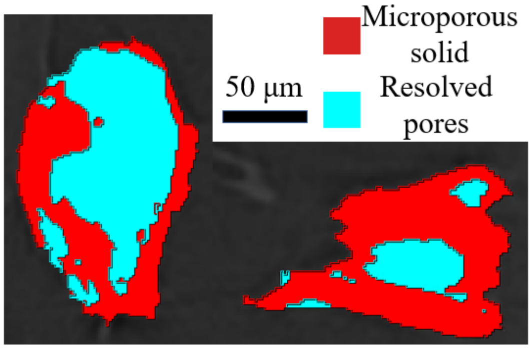

Fig. 6-1 Two orthogonal cross-sections of the same char particle imaged with micro-CT.

X-ray CT has been used to examine the internal and external structure of coal and biomass particles in 3-D (e.g., [116,124,162,163]), including the spatial distribution of porosity and its directionality [115,164]. A single two- to-three-hour micro-CT scan can image the internal and external structure of hundreds of pulverized char particles simultaneously and at high resolution (µm-scale voxels), enabling morphology measurement for every particle in the distribution [122]. However, only a single study [100] has quantified the morphology of a pulverized char particle distribution in three dimensions.

To overcome the disadvantages of the 2-D parameters quantification, Figure 6-2 shows an outline of the automated image analysis procedure in green box proposed in the present study for quantifying char particle morphological parameters in 3-D, which has been implemented using MATLAB. Pre-processing, filtering, and thresholding are used to segment the particles from the background. Segmentation of each particle is then performed in 3-D to distinguish between the carbonaceous microporous solid and the resolved pores. Morphological features are then quantified and can be imported into pre-trained classifiers to select appropriate distributions of particle-scale combustion models and the effectiveness factor models calculation in reactor-scale CFD codes. Details of each step are provided in the next section.

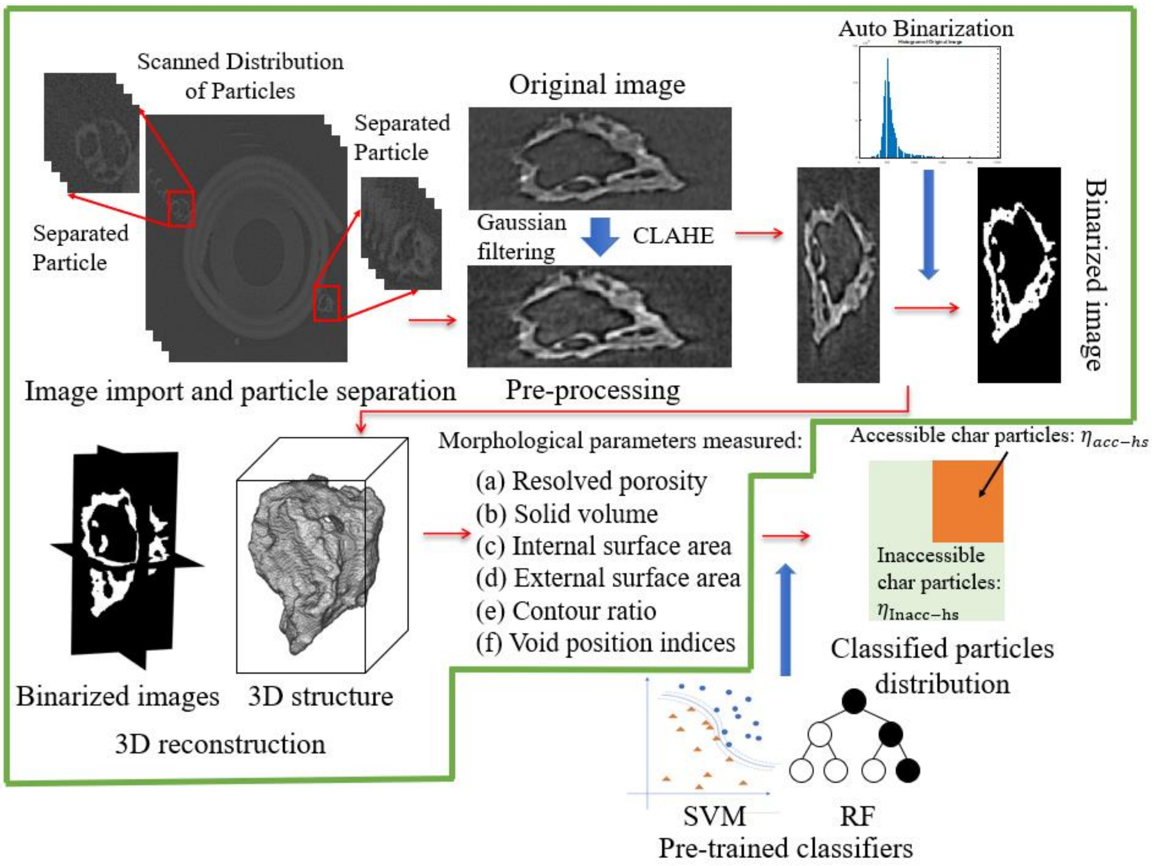

Fig. 6-2 Workflow for automated 3-D image analysis (green box) and classification.

Image segmentation, which plays a key role in this workflow, converts the scanned image into analyzable objects. The non-overlapping objects of interest are partitioned from an image by the image segmentation algorithms using image intensity, texture, contrast, and/or color [165]. Many segmentation algorithms have been developed and can be generally separated into histogram-based thresholding (global, local, entropy, etc.)[166], region-based (clustering [167], graph cut [168]), edge-based [169]. The latter two are also known as level set image segmentation.

Similar to the level-set image segmentation, the classification of the different algorithms based on their properties is shown in Table 6-1 adjusted from [170]. Many of recent developed algorithms are not explained here since it is not the main objective for the current study.

Table 6-1 The classification of level set image technologies.

Level set image segmentation		
Edge-based	**Region-based**	
Distance	Clustering	Watershed
Reaction diffusion	K-means	Markov random field
local region fitting information	Fuzzy c-means	graph cut
Virtual magnetic interaction	local intensity clustering	Region merging prior
L-distribution	Mean shift	Gaussian mixture model
Weighting energy function	Bayesian risk and Bayesian analysis	Region growing

To facilitate application of the workflow to other highly porous char particle distributions, the present chapter will develop an automated 3-D workflow to improve the predictive capability of the reactor-scale CFD simulations by using the correct proportion of effectiveness factor models for particle distributions based on their morphology.

6.2 Automated image analysis procedure

6.2.1 Image pre-processing and filtering

Individual particles were manually separated from the micro-CT scan of the char particle distribution, although this initial step will be automated in the future. One hundred and thirty particles were used to test the automated image analysis procedure, since 20 particles were not able to be segmented from the support material. After a stack of images representing an individual particle is imported, the routine automatically improves image quality by introducing the Gaussian filter window moving through the image matrix to reduce noise, and the contrast-limited adaptive histogram equalization algorithm [171] to enhance contrast.

6.2.2 Automated mask image segmentation

As discussed in the previous section, the level set method is capable to combine with thresholding methods to find accurate initial mask region for further iteration. Therefore, the performance of various histogram-based thresholding technology was tested by ImageJ [172] which has integrated multiple thresholding methods. The original test image and its manual segmentation is shown in Fig 6-3.

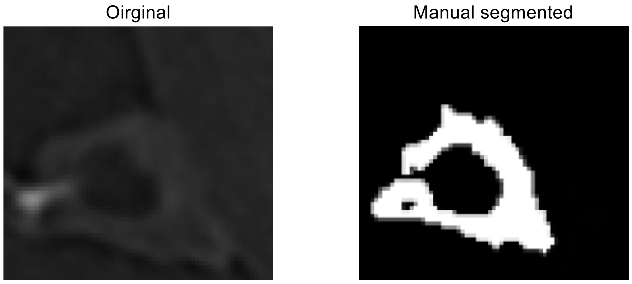

Fig. 6-3 The original test image (left) and the manual segmented image (right).

The same original image imported into the ImageJ and the segmented results were shown in Fig 6-4. The methods applied in the ImageJ here are all classical methods used for image segmentation for a decade. Since there are numbers of developed algorithms, it is a good and quick start to compare multiple methods for the people to determine specific method to focus on. The detailed information about each thresholding methods can be found in the ImageJ reference, the plug-in function is called “Auto Threshold”. Newly developed methods can be used in future work.

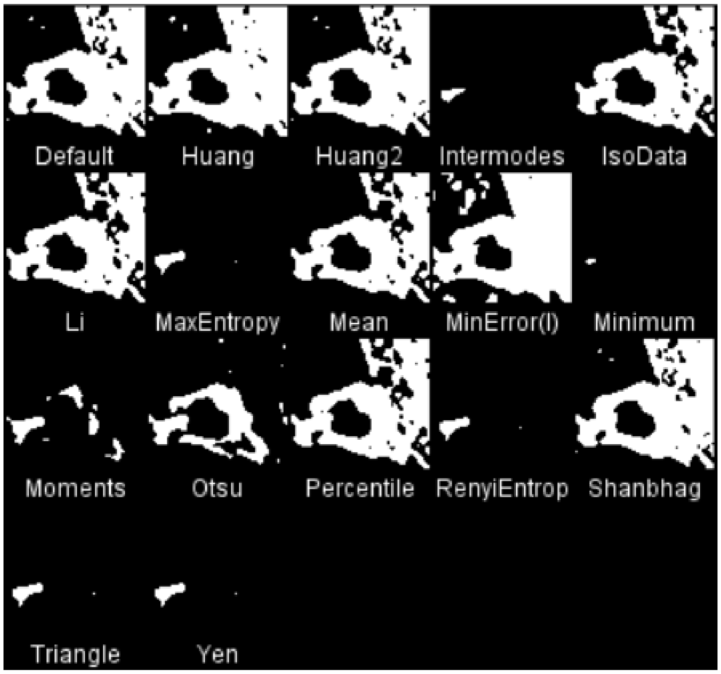

Fig. 6-4 The segmented test images with different thresholding methods.

It is clear that Otsu method performed the best segmentation. Otsu's method determines the minimal variance between the foreground and background by using an image's grayscale histogram. Otsu's method is popular due to its computational efficiency and its accuracy in finding object boundaries [173], but the global thresholding employed in 1-D Otsu's method has limited ability to handle images with low contrast, high noise, and small size compared to the background. 2-D Otsu's method utilizes gray value distributions and grayscale information from neighboring pixels to generate two-dimensional histograms, improving the segmentation performance [174]. Following image preparation and pre-processing, the size of the 3-D image matrix that contains the particle was calculated. Based on that, three 2-D images located at the center of each orientation were found automatically. Those 2-D images, or mask images, from orthogonal planes were extracted from the 3-D images matrix and used for further binarization. The mask images were then automatically binarized by introducing the grayscale images into 2-D Otsu’s function. During the automated procedure, the threshold was calculated based on the greyscale histogram to distinguish the particle from the background. The pixels with grayscale value higher than the threshold were identified as particles while the remaining pixels were labeled as background.

6.2.3 Automated 3-D segmentation

With binarized central mask images, an image matrix was automatically reconstructed by employing the “active contour without edges” function (The “activecontour” function in MATLAB), which is based on the Mumford–Shah minimization and the level set method [175]. The “activecontour” function is employed to segment images into background and foreground due to the following reason: (1) The micro-CT images of char particle are only grey-level images with relatively simple structures. The algorithm uses classic edge-based level set model that is good at handing complex topologies and capturing boundary for images with intensity homogeneity and noises problem (see next section for details). (2) It can combine with thresholds methods to improve the accuracy of the segmentation by generating correct initial mask images. (3) It is user-friendly for people to customize for their own case because it has fewer parameters compared to newly developed algorisms (Such as Level Set Evolution method with Distance Regularized (DRLSE) [176], Level set method based on local approximation of Taylor expansion (LATE) [177], etc.).

Starting from a binarized mask image, the “activecontour” function finds the boundaries of objects and is used to extend segmentation to the entire particle. This method is robust to noise [175], but requires an accurate mask image. Following this segmentation step, a 3-D binary image matrix was produced. Figure 6-5 shows an original micro-CT image, the 2-D binary image from one perspective, and the 3-D structure generated by the automated procedure for image processing, filtering, and segmentation.

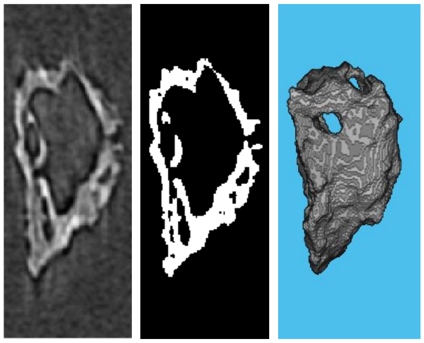

Fig. 6-5 Original image cross section (left), and automatically generated 2-D binary image (middle), and 3-D structure (right).

6.2.4 Automated morphological parameter measurement

Resolved porosity, solid volume, internal surface area, external surface area, contour ratio, and void position indices (VP_L, VP_W, VP_H) were measured using pixel and voxel information obtained from the automatically-generated 3-D structure. The workflow for automated measurement of each parameter is illustrated in Fig. 6-6. All functions employed in the workflow are available in the MATLAB image processing toolbox.

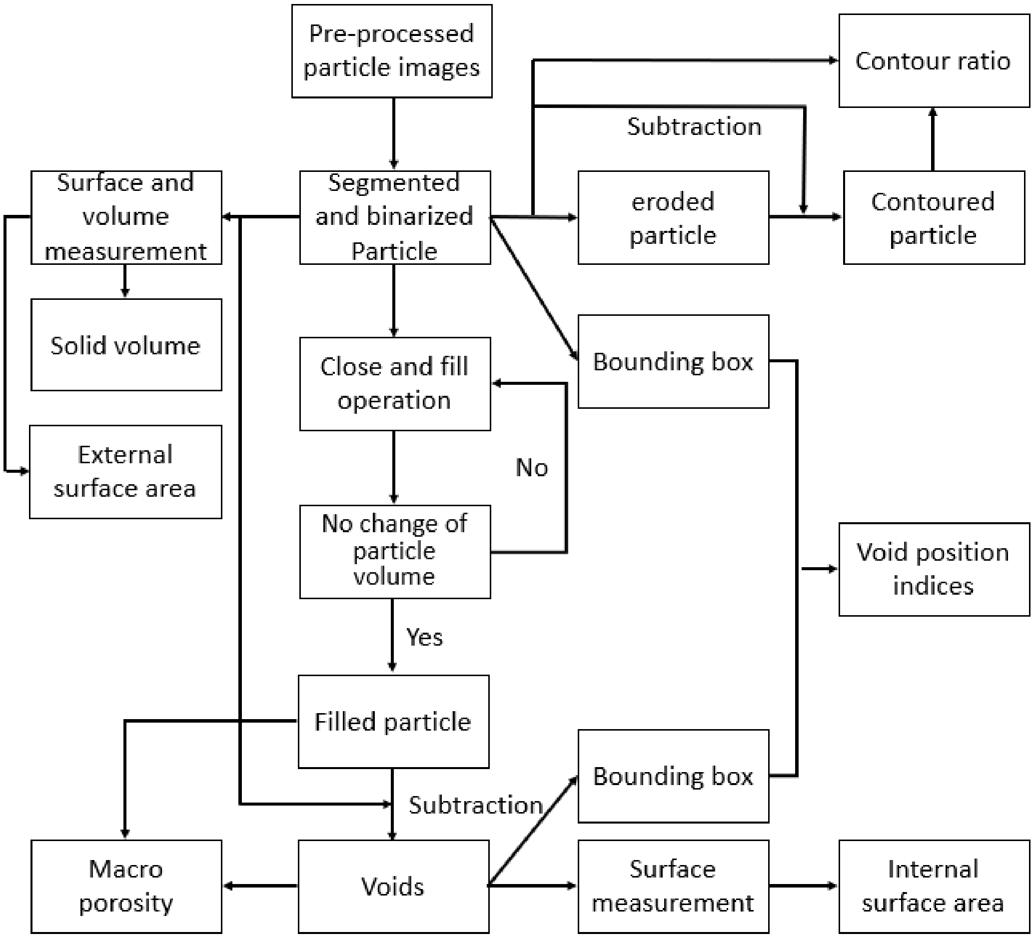

Fig. 6-6 Workflow for automated measurement of morphological parameters.

A loop employing a close and fill operation is first applied to the segmented particle volume. The close function is used to close gaps on the particle surface and a filling function is used to fill isolated resolved pores within the particle. In this step, any pores inside the particle are filled. By using a subtraction function, the pore-space can be extracted from the filled particle. The resolved porosity, θ, is then calculated as the ratio of the pore volume to the volume of the filled particle, in which the volume accounts for the number of voxels in the 3-D volumetric binary image and the voxel size. The surface area calculation is based on the method described in [178] by accounting for distance around the boundary of the region using the Crofton formula. As in the manual measurement (see Chapter 5), the void position indices are obtained in the automated procedure by constructing separate bounding boxes for the particles and their resolved pores. All measurements for surface area, volume, and void position indices are implemented using the MATLAB functions ‘regionprops3’ directly. The erode function is used to find the boundary of the original segmented particle, which is known as a contoured particle. The boundary can be found by subtracting the eroded particle volume from the original particle volume. Therefore, the contour ratio is the number of voxels on the contoured surface divided by the number of voxels in the original segmented particle.

6.3 Results and discussions

To facilitate a fully automated morphology quantification and combustion-model classification scheme for highly porous char particles from other bituminous coal feedstocks, the automated image analysis routine described in Section 6.1 has been tested. The morphological parameters obtained from the automated image analysis routine are compared with the manually-segmented and measured values, which were used to train the classifiers described in the Chapter 5 and analytical effectiveness factor calculations in Chapter 4. The morphology of 130 particles has been quantified with the automated image analysis procedure, since 20 particles could not be auto-segmented due to similarity in the attenuation coefficient between the particles and the support material.

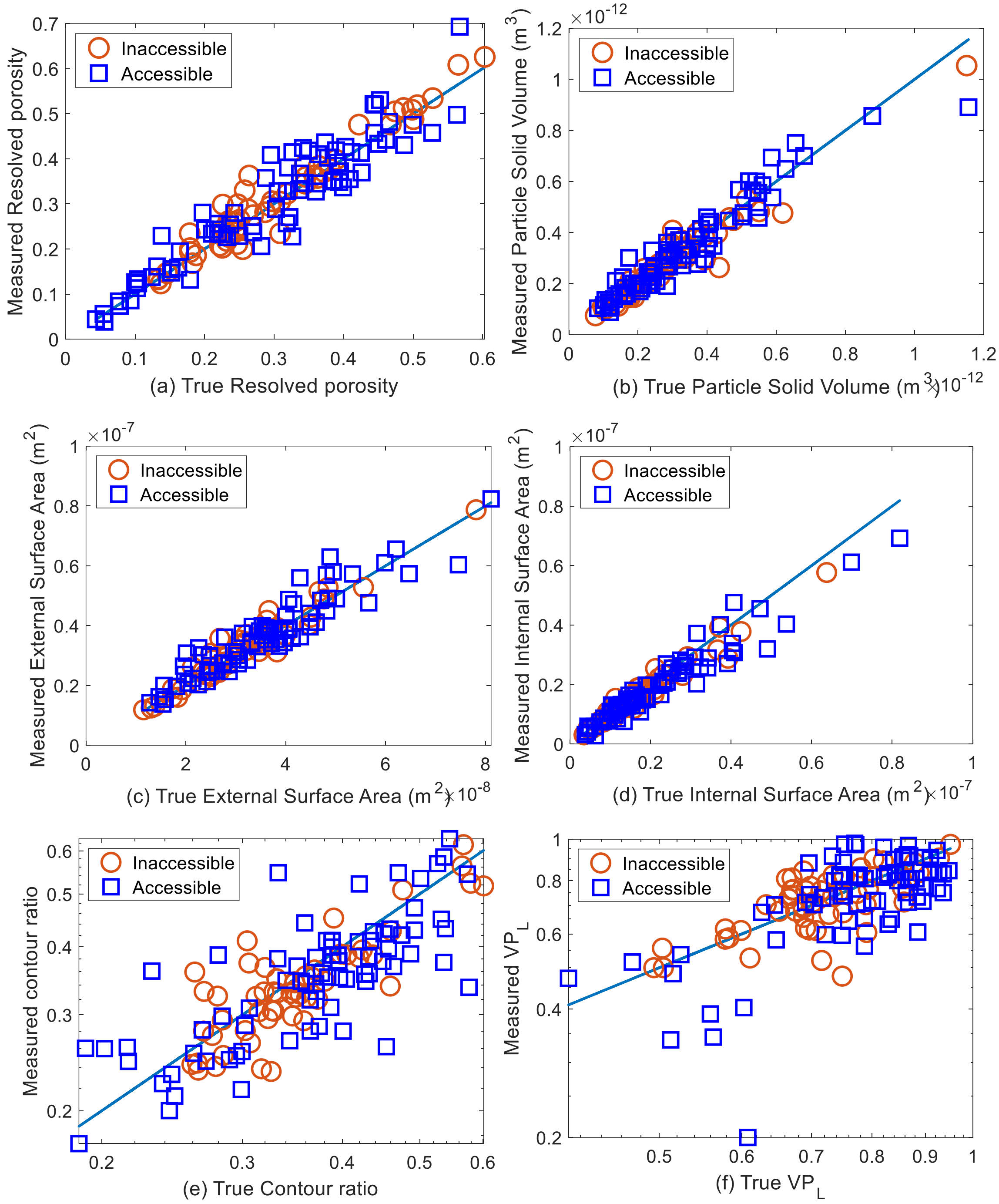

Fig. 6-7 Comparison of automated segmented and measurement with manual segmentation and measurement for (a) resolved porosity, (b) solid volume, (c) external surface area, (d) internal surface area, (e) contour ratio, and (f) VP_L.

The comparisons between automated measurement of resolved porosity, particle solid volume, internal surface area, external surface area, contour ratio, and VP_L and their respective manually measured values are shown in the parity plots of Fig. 6-7, in which the particle classification is also indicated. The average relative errors for automated measurement of resolved porosity, solid volume, external surface, internal surface, contour ratio and VP_Lcompared to their “true” manual measurements are 11.1%, 11.6%, 9.7%, 11.8%, 11.3%, 11.1%, respectively. It is noted that manual segmentation by a skilled operator typically takes at least 30 minutes per particle, while the computational time of automated image analysis is typically between 0.5 and two minutes on a 28-core workstation, depending on the structural complexity and size of the particle and requires no special training.

6.3.1 Assessment of pretrained classifiers using automated parameter measurement

In the proposed workflow, true class labels are assigned using data from the 3-D pore-resolving simulations and classifiers are trained with manually measured morphological data. The *pretrained* classifiers could then be used for other highly porous char particles with morphological data obtained from *automated* image analysis. To test the entire proposed workflow, for 10-fold repeated cross-validation, 120 particles with manually measured data are randomly selected and used to train classifiers and the remaining 30 particles, with automated morphological data measurement, are used to test the classifiers’ performance. After the same repeated cross-validation procedure, the performances of each algorithm are evaluated as shown in Table 6-2 and Table 6-3 respectively.

Table 6-2 Averaged confusion matrix for the SVM classifier using automated data.

		Predicted classes	
		Accessible-type particle	Inaccessible-type particle
Measured classes	Accessible-type particle	TP: 20.1	FN: 0.6
	Inaccessible-type particle	FP: 8.1	TN: 1.2
ACC_{test}		0.710 ± 0.047	
MCC		0.195	

Table 6-3 Averaged confusion matrix for the RF classifier using automated data.

		Predicted classes	
		Accessible-type particle	Inaccessible-type particle
Measured classes	Accessible-type particle	TP: 17.7	FN: 3
	Inaccessible-type particle	FP: 5.5	TN: 3.8
ACC_{test}		0.716 ± 0.058	
MCC		0.291	

The average ACC_{test} for the SVM and RF classifier are 0.710 ± 0.047 and 0.716 ± 0.058, which are slightly lower than the results obtained using manual data. While on the surface it appears that the particles' combustion behavior can be acceptably predicted using automated image analysis data, it is observed from the confusion matrix that the SVM classifier is simply assigning nearly all particles to the larger set (the accessible particle class), leading to a high proportion of correct predictions. The MCC accounts for this behavior in the presence of an unbalanced sample, and the MCC for the SVM with automated morphological data is below 0.2, indicating poorer performance compared to the RF classifier, which has MCC of 0.291 using automated morphological data.

To assess the impact of transitional particles, the MCC of classifiers using both manual and automated morphological measurements as input are calculated with transitional particles eliminated for *AI* ranges of 0.40-0.60, 0.35-0.65, and 0.3-0.7 and shown in Fig.6-8.

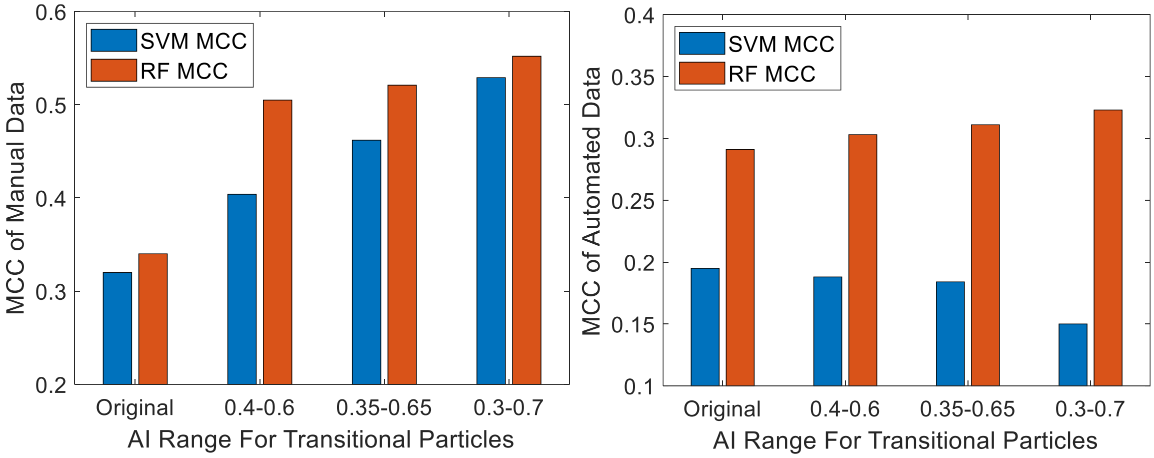

Fig. 6-8 MCC with transitional data removed of (a) manual data (Left) and (b) Automated data (Right).

With increasing numbers of transitional particles removed, the MCC for RF and SVM classifiers increase from 0.34 to 0.552 and 0.32 to 0.529 when using manually measured morphological data as input. For automated morphological data, however, the MCC for RF increases slightly from 0.291 to 0.323 and the MCC for the SVM decreases from 0.195 to 0.150. It thus appears that the transitional particles are not the primary reason for the low classification quality when automated data is employed. Rather, as mentioned above, due to the similarity in attenuation coefficient between the particles and the support material used in the micro-CT imaging, inaccuracies were more likely to occur during the automated image processing than in the manual image processing.

6.3.2 Assessment of proposed workflow for predicting combustion behavior

Based on the data shown in Fig. 5-4 and on Eq. (5-6), $\eta_{overall-3D}$ and *AI* are known for every particle. Knowing the "true" class label for every particle, the "true" analytical model for every particle can be applied to calculate its “true” $\eta_{overall-1D-true}$. The “true” relative error in effectiveness factor when using the most appropriate analytical combustion model (accessible or inaccessible hollow spheres) can then be calculated using

$$\varepsilon_{true\ 1D} = \left|\frac{(\eta_{overall-1D-true} - \eta_{overall-3D})}{\eta_{overall-3D}}\right| \qquad (6-1)$$

This error measures the *physical (1-D) model's* ability to mimic reality (after averaging over all particles tested).

Similarly, for each image analysis/classification combination (manual/SVM, manual/RF, automated/SVM, automated/RF), the “predicted” 1-D model’s overall effectiveness factor, $\eta_{overall-1D-predicted}$, can be compared to $\eta_{overall-3D}$ to calculate the “predicted” relative error

$$\varepsilon_{predicted\ 1D} = \left|\frac{(\eta_{overall-1D-predicted} - \eta_{overall-3D})}{\eta_{overall-3D}}\right| \qquad (6-2)$$

This error measures the *workflow’s* ability to mimic reality when constrained by the choice of physical model (when averaged over all particles tested).

Finally, the ultimate metric for characterizing the proposed workflow's ability to select the most appropriate of the hollow sphere 1-D combustion models is the "performance ratio" $\varepsilon_{true\ 1D} / \varepsilon_{predicted\ 1D}$. A performance ratio of unity indicates that the proposed workflow is doing the best possible implementing the computationally efficient 1-D model, while lower ratios indicate poorer performance.

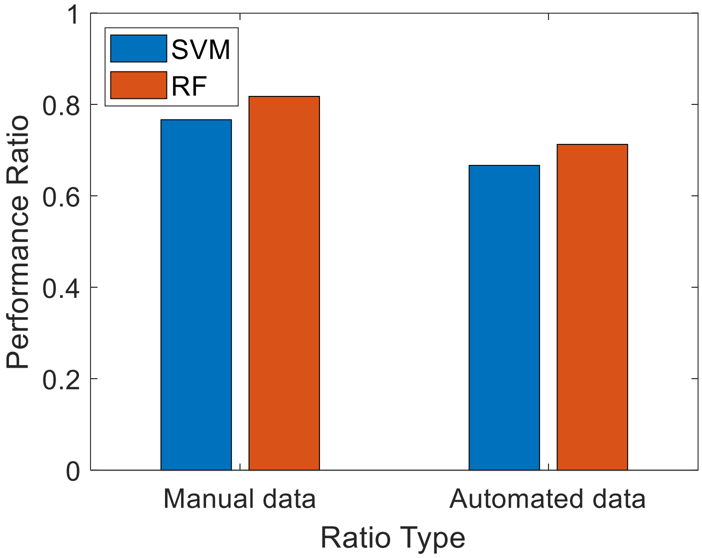

Fig. 6-9 Performance ratio for machine learning algorithms based on the manual and automated data.

The error evaluation procedure was repeated 10 times with 30 randomly selected particles used as test set. Averaging over all particles tested, $\varepsilon_{true\ 1D}$ was 0.099. For SVM and RF with manual measured parameters, $\varepsilon_{predicted\ 1D}$ was 0.129 and 0.121, respectively. For SVM and RF with automated image analysis and measurement, $\varepsilon_{predicted\ 1D}$ was 0.147 and 0.137, respectively. Therefore, the performance ratio for SVM and RF with manual measured parameters are 0.767 and 0.818, while the ratio for SVM and RF with automated measured parameters are 0.673 and 0.723. These performance ratios are shown in Fig. 6-9 for the four combinations of image analysis/classification approaches. The latter value indicates that the entire proposed workflow, with fully automated image analysis and pretrained RF classification based on

3-D pore resolving simulations, can reasonably implement a computationally efficient particle combustion model amenable for incorporation in reactor-scale CFD codes. Nonetheless, as indicated by the confusion matrices and MCC values in Tables 6-2 and 6-3, optimization of the particle mounting in the micro-CT imaging procedure to increase contrast in the attenuation coefficients between the particles and substrate, improvements to the image analysis routine, optimization of the classifiers, and a larger, more balanced sample would likely improve the workflow's performance.

6.4 Conclusions

To facilitate application of pretrained classifiers to other porous char particles, an automated image analysis routine was developed to process and segment individual particles and to measure their 3-D morphological parameters required by the classifier.

The functions from MATLAB's image processing toolbox that can be easily customized for specific problems are employed in this automated image analysis routine. The routine segments individual particles and measures their 3-D morphological parameters required by the classifier and effectiveness factor models calculation. For the six key morphological parameters that were used in the machine learning classification algorithm and analytical effectiveness factor models calculation, the highest average relative error for automated measurement of the key morphological parameters compared to the manual measurements was 11.8%.

The ability of the entire proposed workflow to select a computationally efficient 1-D model using fully automated image analysis and pretrained classifiers was assessed. It is noted that the classification employed for char particles is based on a continuous quantitative metric (*AI*) rather than qualitative differences that can be unambiguously classified. Furthermore, the ultimate metric for assessing the workflow is its accuracy in the selected combustion model. When using the most appropriate analytical model for each particle, as determined by the true *AI* values from 3-D CFD, the average relative error in analytical effectiveness factors compared to the effectiveness factor from the 3-D simulations was 0.099, whereas the average relative error in analytical effectiveness factors predicted by the full workflow was 0.137 for the RF classifier with automated image analysis and measurement. Further work could improve the workflow's accuracy and efficiency, such as automated particles separation, advanced segmentation technology, and larger sample sizes, as discussed in the final chapter.

Chapter 7. Conclusions and Future Work

7.1 Conclusions

Reactor-scale CFD simulation is a useful method for understanding solid fuel combustion and gasification and to enhance its efficiency and reduce its cost. Reactor-scale CFD requires accurate and predictive sub-models describing the behavior of single char particles that are tracked in reactor-scale codes.

Combustion and gasification of pulverized char often occur under zone II conditions, in which the rate of conversion depends on both heterogeneous reaction and gas transport within the particle’s porous structure. The morphology of porous char has a strong influence on intra-particle diffusion, and thus, on the overall conversion rate. Because pulverized coal and biomass char particles are often irregularly shaped and contain pores and voids which can approach the size of the particles themselves, conventional models based on spherical and cylindrical symmetry and coarse-grained, upscaled, effective continuum conservation equations are not applicable or appropriate.

A 3-D, pore-resolving CFD simulation approach based on real char particle geometries obtained from X-ray micro-computed tomography (micro-CT) obviates the need to upscale over large heterogeneities and to make oversimplifying geometric assumptions. Using pore-resolving CFD simulation for real 3-D char particles, the impacts of particle morphology on reactant profiles and the “true” effectiveness factor has been studied. Fundamental insights from this model have been used to evaluate the fidelity of existing effectiveness factor approaches by comparison with the results from 3-D simulation, to determine when existing models can be accurately applied.

For coal char particles, the micro-CT-based pore-resolving approach is employed to study zone II combustion for porous bituminous coal char particles produced at a high heating rate. The large pores often present in char particles enhance reactant transport throughout the particles, even within the micro- and meso-porous carbon surrounding the large pores. This is particularly the case for network-type particle structures, due to the prominence of channels that extend from the particle surface. Cenospherical particles can be reasonably modeled using an effectiveness factor solution for inaccessible hollow spheres. The effectiveness factor of particles with higher connectivity to the outer surface can be predicted well by the accessible hollow sphere model.

Biomass char particle morphology affects combustion behaviors at the particle scale as well. It is also typical for most biomass char particle combustion models to employ coarse-grained, effective-continuum approaches, which treat all porosity at the subgrid-scale. Effective-continuum approaches are not valid or accurate in the presence of large, irregular pores which can approach the size of the particle. The 3-D, pore-resolving CFD simulation approach using real biomass char particle geometries obtained from X-ray micro-computed tomography (micro-CT) is therefore used to examine the impact of morphology on zone II combustion for 30 pulverized, high aspect ratio, pine char particles. These sub-millimeter biomass char particles exhibited significant, localized reactant penetration into the innermost regions of the particles, facilitated by the presence of large pores connected to the external surface as what have been found in coal char particle morphology study. The oxygen mole fraction distributions were governed by the large pore morphology, were non-monotonic with distance from the surface, and achieved minima in thick microporous char regions surrounding the large pores. A comparison between the pore-resolving simulation and an equivalent, spatially resolved, effective-continuum simulation revealed that even in the microporous char, the effective-continuum model underpredicted reactant penetration. A careful comparison was then performed between the 30 pore-resolving particle simulations and several effectiveness factor models that employed particle-specific parameters. Commonly used uniform cylinder models significantly underpredicted effectiveness factors for these real pulverized pine char particles, while accessible hollow cylinder models achieved less than 10% relative error when averaged over all 30 particles.

While reactor-scale CFD codes often employ a distribution of particle sizes, they should also consider a distribution of particle morphologies with a corresponding distribution of effectiveness factor models to improve their predictive capabilities. To facilitate the use of realistic particle morphology distributions in reactor-scale CFD codes, a distribution of char particles formed under realistic heating conditions must be analyzed and classified. An automated workflow is proposed for 3-D morphological parameter quantification and classification to assign appropriate effectiveness factor models for as distribution of coal char particles.

Two different ML algorithms (Support Vector Machine and Random Forest) are employed to classify char particles according to 1-D combustion model (inaccessible or accessible hollow spheres) using 3-D morphology as input and 3-D pore-resolving simulation data for training. The misclassified particles are generally transitional particles which exhibited intermediate zone II combustion behaviors between that of accessible and inaccessible hollow spheres, indicating that a multi-class classifier could improve performance.

To complete the workflow, morphological parameters used as input to the classifiers and required by the 1-D combustion models are automatically measured using a routine developed in MATLAB. The average relative errors for automated measurement of the key morphological parameters compared to the manual measurements are all under 11.8%. The general computation time is between 0.5 and two minutes on a 28-core workstation while the manual measurement typically takes over 30 minutes.

The performance of the entire proposed workflow using automated image analysis and pretrained classifiers was assessed. When using the most appropriate analytical model for each particle, as determined by the true AI values from 3-D CFD, the average relative error in analytical effectiveness factors compared to the effectiveness factor from the 3-D simulations was 0.099, whereas the average relative error in analytical effectiveness factors predicted by the full workflow was 0.137 for the RF classifier with automated image analysis and measurement.

7.2 Future work

7.2.1 New analytical effectiveness factor model

Even though accuracy would increase if the inaccessible/accessible hollow sphere models could be perfectly assigned, it is noted that existing effectiveness factor models cannot deal well with the particles that exhibit transitional behavior. Thus, a new effectiveness factor model should be further investigated to capture transitional particle behavior or even all types of particles, regardless of their pore connectivity to the outer surface. In recent work, we have found that the 1D–GC/VD models (mentioned in Chapter 4) are a possible solution.

In Chapter 4, the accuracy of 1D–GC/VD models, which use entire morphological information (G function), is limited by the restrictive assumption, for high temperature combustion and gasification applications, of uniform reactant concentration along the interface between the microporous solid and external surface/resolved pores. This causes a higher predicted effectiveness factor than the “true” effectiveness factor. However, based on our recent findings, if the uniform interface boundary condition employs the averaged reactant concentration measured at the interface between the microporous solid and external surface/resolved pores (the red/blue and red/green interfaces in Fig. 3-4 in Chapter 3), the 1D–GC/VD model agrees quite well with the 3-D effectiveness factor for both coal and biomass char particles, as shown in Fig. 7-1.

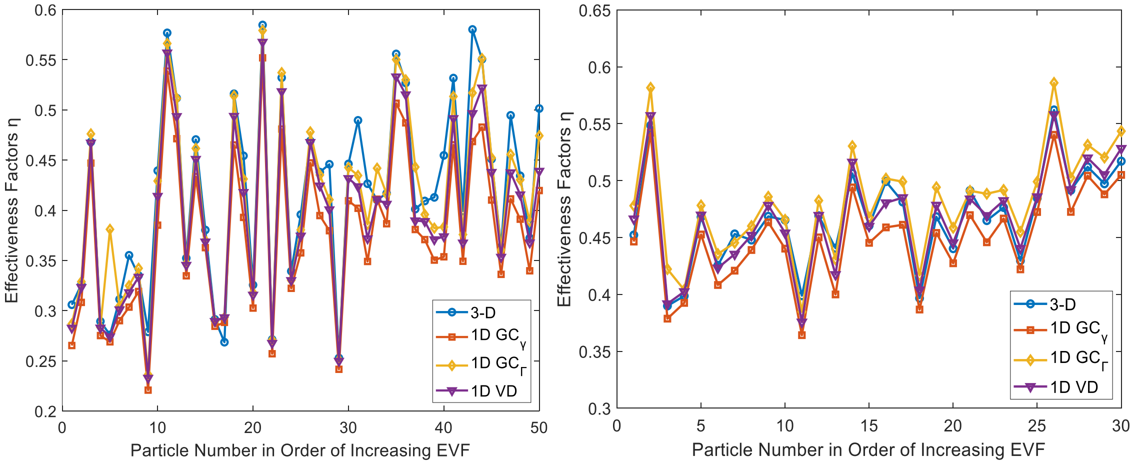

Fig. 7-1 Comparison of effectiveness factors predicted by 1D–GC and 1D–VD models effectiveness factor obtained by volume integration of the 3-D, pore-resolving simulation data for coal (left) and biomass (right).

Therefore, if the correct reactant concentration can be *calculated* at the interfacial boundary (inside and outside), the 1D–GC/VD model would be suitable for all particles irrespective of their structure. The spherical boundary diffusion model [36] that is normally used to calculate reactant partial pressure on the particle surface (see Chapter 5) is a decent starting point for future work but is not sufficiently complex to account for the reduction in reactant concentration that occurs within the resolved pores en route to the red/blue interface of Fig. 3-4.

7.2.2 Automated particle separation

The automated image analysis routine is currently based on manual particle separation as a first step. In future work, this step can be automated using the edge detecting filters (Sobel, Prewitt, etc.) or watershed transformation. A stack of scanned micro-CT images that contain multiple char particle on the support material would first be automatically binarized and flood-filled (if the watershed algorithm is applied). The individual particles would then be masked and separated. The procedure is shown in Fig 7-2.

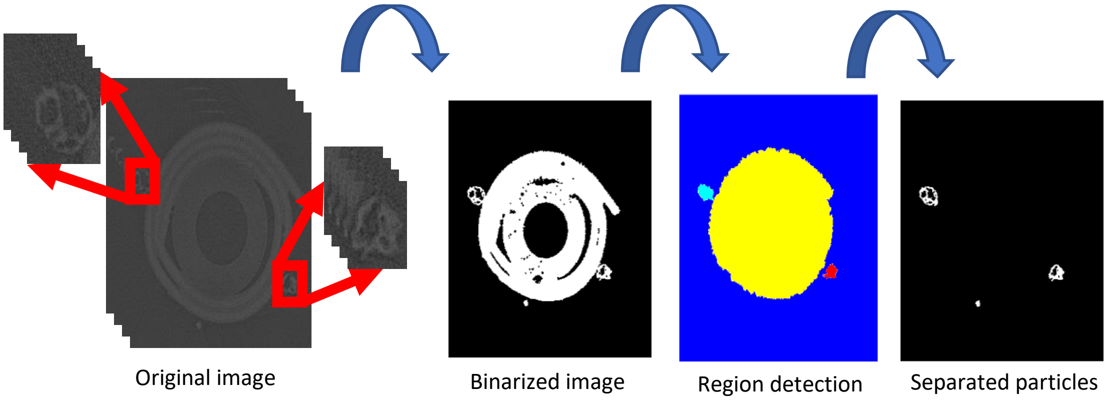

Fig. 7-2 Automated particle separation procedure using watershed transformation.

Beyond that, more advanced methods for segmentation and increased image quality (via a new support material that can be better distinguished from the char particles) would likely improve the accuracy of 3-D structure construction.

7.2.3 Classifier improvement

As already mentioned in Chapter 5, using machine learning method to classify particles based on current measured parameters provides acceptable accuracy with standard hyperparameters applied. Better performance may be achievable by optimizing the hyperparameters, as well as expanding the data set and introducing a multi-level classification system. Machine learning algorithms such as ANNs could also be tested if the data set became large enough.

REFERENCES

[1] BP, Statistical Review of World Energy globally consistent data on world energy markets . and authoritative publications in the field of energy, BP Energy Outlook 2021. 70 (2021) 8–20.

[2] World Energy Council (WEC), World Energy Scenarios 2019 : Exploring Innovation Pathways to 2040, WEC Publications. (2019) 1–152. https://www.worldenergy.org/assets/downloads/2019_Scenarios_Full_Report.pdf.

[3] World Bioenergy Association, GLOBAL BIOENERGY STATISTICS 2021, 2021.

[4] T. Wang, 1 - An overview of IGCC systems, in: T. Wang, G.B.T.-I.G.C.C. (IGCC) T. Stiegel (Eds.), Woodhead Publishing, 2017: pp. 1–80. https://doi.org/https://doi.org/10.1016/B978-0-08-100167-7.00001-9.

[5] J.G. Speight, 9 - Coal gasification processes for synthetic liquid fuel production, in: R. Luque, J.G.B.T.-G. for S.F.P. Speight (Eds.), Woodhead Publishing Series in Energy, Woodhead Publishing, 2015: pp. 201–220. https://doi.org/https://doi.org/10.1016/B978-0-85709-802-3.00009-6.

[6] J. Yu, V. Strezov, J. Lucas, T. Wall, Swelling behaviour of individual coal particles in the single particle reactor, Fuel. 82 (2003) 1977–1987. https://doi.org/10.1016/S0016-2361(03)00159-5.

[7] A. Franco, A.R. Diaz, The future challenges for "clean coal technologies": Joining efficiency increase and pollutant emission control, Energy. 34 (2009) 348–354. https://doi.org/10.1016/j.energy.2008.09.012.

[8] B. Zhang, Z. Shen, J. Sun, H. Zou, K. He, X. Wang, J. Li, S. Cui, N. Zhang, J. Cao, Emission characteristics and formation mechanisms of PM2.5 and gases from different geological maturities coals combustion, Fuel. 315 (2022) 123240. https://doi.org/10.1016/j.fuel.2022.123240.

[9] Y.R. Li, J.M. Gibson, Health and air quality benefits of policies to reduce coal-fired power plant emissions: A case study in North Carolina, Environ Sci Technol. 48 (2014) 10019–10027. https://doi.org/10.1021/es501358a.

[10] IEA, World Energy Outlook 2021 - revised version October 2021, (2021). www.iea.org/weo.

[11] J.G. Speight, Handbook of Gasification Technology: Science, Processes, and Applications, John Wiley & Sons, 2020.

[12] S. Pang, 9 - Fuel flexible gas production: Biomass, coal and bio-solid wastes, in: J.B.T.-F.F.E.G. Oakey (Ed.), Woodhead Publishing, Boston, 2016: pp. 241–269. https://doi.org/https://doi.org/10.1016/B978-1-78242-378-2.00009-2.

[13] A.-G. Collot, Matching gasification technologies to coal properties, Int J Coal Geol. 65 (2006) 191–212. https://doi.org/https://doi.org/10.1016/j.coal.2005.05.003.

[14] M.L. de Souza-Santos, Solid fuels combustion and gasification: modeling, simulation, CRC Press, 2010.

[15] U. Kleinhans, S. Halama, H. Spliethoff, The role of gasification reactions during pulverized solid fuel combustion: A detailed char combustion model based on measurements of char structure and kinetics for coal and pre-treated biomass, Combust Flame. 184 (2017) 117–135. https://doi.org/10.1016/j.combustflame.2017.05.033.

[16] S. Schulze, A. Richter, M. Vascellari, A. Gupta, B. Meyer, P.A. Nikrityuk, Novel intrinsic-based submodel for char particle gasification in entrained-flow gasifiers: Model development, validation and illustration, Appl Energy. 164 (2016) 805–814. https://doi.org/https://doi.org/10.1016/j.apenergy.2015.12.018.

[17] M. Vascellari, R. Arora, C. Hasse, Simulation of entrained flow gasification with advanced coal conversion submodels. Part 2: Char conversion, Fuel. 118 (2014) 369–384. https://doi.org/10.1016/j.fuel.2013.11.004.

[18] P. Rößger, A. Richter, Numerical modeling of a batch fluidized-bed gasifier: Interaction of chemical reaction, particle morphology development and hydrodynamics, Powder Technol. 384 (2021) 148–159. https://doi.org/10.1016/j.powtec.2021.01.072.

[19] X. Cai, S. Shan, Q. Zhang, J. Zhao, Z. Zhou, New WSGG model for gas mixtures of H2O, CO2, and CO in typical coal gasifier conditions, Fuel. 311 (2022) 122541. https://doi.org/10.1016/j.fuel.2021.122541.

[20] M. Wang, Y. Wan, Q. Guo, Y. Bai, G. Yu, Y. Liu, H. Zhang, S. Zhang, J. Wei, Brief review on petroleum coke and biomass/coal co-gasification: Syngas production, reactivity characteristics, and synergy behavior, Fuel. 304 (2021) 121517. https://doi.org/10.1016/j.fuel.2021.121517.

[21] A.M. Eaton, L.D. Smoot, S.C. Hill, C.N. Eatough, Components, formulations, solutions, evaluation, and application of comprehensive combustion models, Prog Energy Combust Sci. 25 (1999) 387–436. https://doi.org/https://doi.org/10.1016/S0360-1285(99)00008-8.

[22] L. Chen, S.Z. Yong, A.F. Ghoniem, Oxy-fuel combustion of pulverized coal: Characterization, fundamentals, stabilization and CFD modeling, Prog Energy Combust Sci. 38 (2012) 156–214. https://doi.org/https://doi.org/10.1016/j.pecs.2011.09.003.

[23] A. Silaen, T. Wang, Effect of turbulence and devolatilization models on coal gasification simulation in an entrained-flow gasifier, Int J Heat Mass Transf. 53

(2010) 2074–2091. https://doi.org/https://doi.org/10.1016/j.ijheatmasstransfer.2009.12.047.

[24] J. Wang, L. Kong, J. Bai, H. Li, Z. Bai, X. Li, W. Li, The role of residual char on ash flow behavior, Part 1: The effect of graphitization degree of residual char on ash fusibility, Fuel. 234 (2018) 1173–1180. https://doi.org/https://doi.org/10.1016/j.fuel.2018.08.011.

[25] R. Beetstra, M.A. van der Hoef, J.A.M. Kuipers, Drag force of intermediate Reynolds number flow past mono- and bidisperse arrays of spheres, AIChE Journal. 53 (2007) 489–501. https://doi.org/https://doi.org/10.1002/aic.11065.

[26] P.A. Nikrityuk, Gasification Processes: Modeling and Simulation Thermo-Fluid, 2014.

[27] B.M. Franchetti, F. Cavallo Marincola, S. Navarro-Martinez, A.M. Kempf, Large Eddy Simulation of a 100 kWth swirling oxy-coal furnace, Fuel. 181 (2016) 491–502. https://doi.org/10.1016/j.fuel.2016.05.015.

[28] S.R. Gubba, L. Ma, M. Pourkashanian, A. Williams, Influence of particle shape and internal thermal gradients of biomass particles on pulverised coal/biomass co-fired flames, Fuel Processing Technology. 92 (2011) 2185–2195. https://doi.org/10.1016/j.fuproc.2011.07.003.

[29] D.-I.S. Halama, I.H. Spliethoff, Computational Modeling (CFD) of Entrained Flow Gasification Kinetics with focus on the Structural Evolution of Char Particles, in: 6th International Freiberg Conference on IGCC & XtL Technologies, 2014.

[30] E. Kumplnsky, N.R. Amundson, Diffusion and Reaction in a Stagnant Boundary Layer about a Carbon Particle. 8a. Effect of the Carbon Dioxide Reduction Reaction, Industrial and Engineering Chemistry Fundamentals. 23 (1984) 34–37. https://doi.org/10.1021/i100013a007.

[31] C.Y. Wen, T.Z. Chaung, Entrained-Bed Coal Gasification Modeling., Coal Processing Technology. 5 (1979) 178–118.

[32] M.M. BAUM, P.J. STREET, Predicting the Combustion Behaviour of Coal Particles, Combustion Science and Technology. 3 (1971) 231–243. https://doi.org/10.1080/00102207108952290.

[33] I.W. Smith, The combustion rates of coal chars: A review, Symposium(International) on Combustion. 19 (1982) 1045–1065.

[34] J.W. Veldsink, R.M.J. van Damme, G.F. Versteeg, W.P.M. van Swaaij, The use of the dusty-gas model for the description of mass transport with chemical reaction in porous media, The Chemical Engineering Journal and the Biochemical Engineering Journal. 57 (1995) 115–125. https://doi.org/https://doi.org/10.1016/0923-0467(94)02929-6.

[35] M. Schmal, J.L.F. Monteiro, J.L. Castellan, Kinetics of coal gasification, Industrial & Engineering Chemistry Process Design and Development. 21 (1982) 256–266.

[36] N.M. Laurendeau, Heterogeneous kinetics of coal char gasification and combustion, Prog Energy Combust Sci. 4 (1978) 221–270. https://doi.org/10.1016/0360-1285(78)90008-4.

[37] M. Weeda, P.J.J. Tromp, B. Van der Linden, J.A. Moulijn, High temperature gasification of coal under severely product inhibited conditions: the potential of catalysis, Fuel. 69 (1990) 846–850.

[38] A. J.-L., Upscaling Heterogeneous Media by Asymptotic Expansions, J Eng Mech. 128 (2002) 817–822. https://doi.org/10.1061/(ASCE)0733-9399(2002)128:8(817).

[39] R. Jovanovic, A. Milewska, B. Swiatkowski, A. Goanta, H. Spliethoff, Sensitivity analysis of different devolatilisation models on predicting ignition point position during pulverized coal combustion in O 2/N 2 and O 2/CO 2 atmospheres, Fuel. 101 (2012) 23–37. https://doi.org/10.1016/j.fuel.2011.02.024.

[40] D.A. Bell, B.F. Towler, M. Fan, Coal gasification and its applications, William Andrew, 2010.

[41] P.A. BEJARANO, Y.A. LEVENDIS, COMBUSTION OF COAL CHARS IN OXYGEN-ENRICHED ATMOSPHERES, Combustion Science and Technology. 179 (2007) 1569–1587. https://doi.org/10.1080/00102200701239272.

[42] P.A. Bejarano, Y.A. Levendis, Single-coal-particle combustion in O2/N2 and O2/CO2 environments, Combust Flame. 153 (2008) 270–287. https://doi.org/https://doi.org/10.1016/j.combustflame.2007.10.022.

[43] U. Kleinhans, S. Halama, H. Spliethoff, Char particle burning behavior: Experimental investigation of char structure evolution during pulverized fuel conversion, Fuel Processing Technology. 171 (2018) 361–373. https://doi.org/https://doi.org/10.1016/j.fuproc.2017.10.022.

[44] G. Fong, S. Jorgensen, S.L. Singer, Pore-Resolving Simulation of Char Particle Gasification Using Micro-CT, Fuel. 224 (2018) 752–763. https://doi.org/10.1016/j.fuel.2018.03.117.

[45] P.W. Selwood, P.B. Weisz, D.D. Eley, Advances in catalysis, Academic Press, 1959.

[46] E.S. Hecht, C.R. Shaddix, A. Molina, B.S. Haynes, Effect of CO2 gasification reaction on oxy-combustion of pulverized coal char, Proceedings of the Combustion Institute. 33 (2011) 1699–1706. https://doi.org/https://doi.org/10.1016/j.proci.2010.07.087.

[47] S.L. Singer, A.F. Ghoniem, Comprehensive gasification modeling of char particles with multi-modal pore structures, Combust Flame. 160 (2013) 120–137. https://doi.org/10.1016/j.combustflame.2012.09.007.

[48] E.M. Hodge, The coal char-CO2 reaction at high temperature and high pressure, (2008) 375.

[49] N.J. Mariani, C. Mocciaro, O.M. Martínez, G.F. Barreto, Estimation of effectiveness factor for arbitrary particle shape and non-linear kinetics, Ind Eng Chem Res. 48 (2009) 1172–1177.

[50] C.N. Satterfield, Mass transfer in heterogeneous catalysis, MIT press, 1970.

[51] S. Dutta, C.Y. Wen, R.J. Belt, Reactivity of Coal and Char. 1. In Carbon Dioxide Atmosphere, Industrial & Engineering Chemistry Process Design and Development. 16 (1977) 20–30. https://doi.org/10.1021/i260061a004.

[52] J. Rouquerol, D. Avnir, C.W. Fairbridge, D.H. Everett, J.M. Haynes, N. Pernicone, J.D.F. Ramsay, K.S.W. Sing, K.K. Unger, Recommendations for the characterization of porous solids (Technical Report), Pure and Applied Chemistry. 66 (1994) 1739–1758.

[53] J. Hong, Modeling char oxidation as a function of pressure using an intrinsic Langmuir rate equation, Brigham Young University, 2000.

[54] R. Jackson, Transport in porous catalysts, Elsevier Science & Technology, 1977.

[55] C. Georgakis, C.W. Chang, J. Szekely, A changing grain size model for gas—solid reactions, Chem Eng Sci. 34 (1979) 1072–1075. https://doi.org/https://doi.org/10.1016/0009-2509(79)80012-3.

[56] S.K. Bhatia, D.D. Perlmutter, A random pore model for fluid-solid reactions: I. Isothermal, kinetic control, AIChE Journal. 26 (1980) 379–386. https://doi.org/https://doi.org/10.1002/aic.690260308.

[57] I.W. SMITH, R.J. TYLER, The Reactivity of a Porous Brown Coal Char to Oxygen between 630 and 1812° K, Combustion Science and Technology. 9 (1974) 87–94. https://doi.org/10.1080/00102207408960342.

[58] E.W. Thiele, Relation between catalytic activity and size of particle, Ind Eng Chem. 31 (1939) 916–920.

[59] C.B. Nguyen, J. Scherer, Q. Guo, S. Kriebitzsch, A. Richter, The shape development of spherical and non-spherical char particles in the flame zone of an entrained-flow gasifier – A numerical study, Int J Heat Mass Transf. 149 (2020) 119220. https://doi.org/10.1016/j.ijheatmasstransfer.2019.119220.

[60] A. Phounglamcheik, M. Bäckebo, R. Robinson, K. Umeki, The significance of intraparticle and interparticle diffusion during CO2 gasification of biomass char in a packed bed, Fuel. 310 (2022). https://doi.org/10.1016/j.fuel.2021.122302.

[61] A.M. Lattanzi, M.B. Pecha, V.S. Bharadwaj, P.N. Ciesielski, Beyond the effectiveness factor: Multi-step reactions with intraparticle diffusion limitations, Chemical Engineering Journal. 380 (2020). https://doi.org/10.1016/j.cej.2019.122507.

[62] A.N. Hayhurst, The mass transfer coefficient for oxygen reacting with a carbon particle in a fluidized or packed bed, Combust Flame. 121 (2000) 679–688. https://doi.org/10.1016/S0010-2180(99)00178-9.

[63] K. Malek, M.O. Coppens, Knudsen self- and Fickian diffusion in rough nanoporous media, Journal of Chemical Physics. 119 (2003) 2801–2811. https://doi.org/10.1063/1.1584652.

[64] E.M. Hodge, D.G. Roberts, D.J. Harris, J.F. Stubington, The significance of char morphology to the analysis of high-temperature char-CO2 reaction rates, Energy and Fuels. 24 (2010) 100–107. https://doi.org/10.1021/ef900503x.

[65] S.S. Hla, D.G. Roberts, D.J. Harris, A numerical model for understanding the behaviour of coals in an entrained-flow gasifier, Fuel Processing Technology. 134 (2015) 424–440. https://doi.org/10.1016/j.fuproc.2014.12.053.

[66] H. Fatehi, X.S. Bai, Effect of Pore Size on the Gasification of Biomass Char, Energy Procedia. 75 (2015) 779–785. https://doi.org/10.1016/j.egypro.2015.07.514.

[67] H. Fatehi, X.S. Bai, Structural evolution of biomass char and its effect on the gasification rate, Appl Energy. 185 (2017) 998–1006. https://doi.org/10.1016/j.apenergy.2015.12.093.

[68] R. Datta, S.W.K. Leung, Shape Generalized Isothermal Effectiveness Factor for First-Order Kinetics, Chem Eng Commun. 39 (1985) 155–173. https://doi.org/10.1080/00986448508911668.

[69] N.J. Mariani, M.J. Taulamet, S.D. Keegan, O.M. Martínez, G.F. Barreto, Prediction of effectiveness factor using one-dimensional approximations for complex pellet shapes and abnormal kinetics expressions, Ind Eng Chem Res. 52 (2013) 15321–15329. https://doi.org/10.1021/ie4005805.

[70] T. Doğfu, Diffusion and reaction in catalyst pellets with bidisperse pore size distribution, Ind Eng Chem Res. 37 (1998) 2158–2171. https://doi.org/10.1021/ie970613t.

[71] S. Whitaker, Diffusion and dispersion in porous media, AIChE Journal. 13 (1967) 420–427. https://doi.org/https://doi.org/10.1002/aic.690130308.

[72] S. Wu, Surface reaction rates of coarse bituminous char particles in the temperature range 600 to 1340 K, 72 (1993) 1429–1433.

[73] L. Ma, R. Mitchell, Modeling char oxidation behavior under Zone II burning conditions at elevated pressures, Combust Flame. 156 (2009) 37–50. https://doi.org/https://doi.org/10.1016/j.combustflame.2008.06.015.

[74] S. Schulze, P. Nikrityuk, Z. Abosteif, S. Guhl, A. Richter, B. Meyer, Heat and mass transfer within thermogravimetric analyser: From simulation to improved estimation of kinetic data for char gasification, Fuel. 187 (2017) 338–348. https://doi.org/https://doi.org/10.1016/j.fuel.2016.09.048.

[75] Y. Bachmat, J. Bear, Macroscopic modelling of transport phenomena in porous media. 1: The continuum approach, Transp Porous Media. 1 (1986) 213–240. https://doi.org/10.1007/BF00238181.

[76] R. Sahu, R.C. Flagan, G.R. Gavalas, Discrete simulation of cenospheric coal-char combustion, Combust Flame. 77 (1989) 337–346. https://doi.org/https://doi.org/10.1016/0010-2180(89)90139-9.

[77] S. Whitaker, The method of volume averaging, Springer Science & Business Media, 2013.

[78] M. Sahimi, G.R. Gavalas, T.T. Tsotsis, Statistical and continuum models of fluid-solid reactions in porous media, Chem Eng Sci. 45 (1990) 1443–1502. https://doi.org/https://doi.org/10.1016/0009-2509(90)80001-U.

[79] A.M. Beckmann, J. Bibrzycki, M. Mancini, A. Szlęk, R. Weber, Mathematical modeling of reactants' transport and chemistry during oxidation of a millimeter-sized coal-char particle in a hot air stream, Combust Flame. 180 (2017) 2–9. https://doi.org/https://doi.org/10.1016/j.combustflame.2017.02.026.

[80] C.B. Nguyen, J. Scherer, M. Hartwich, A. Richter, The morphology evolution of char particles during conversion processes, Combust Flame. 226 (2021) 117–128. https://doi.org/10.1016/j.combustflame.2020.11.038.

[81] Y. Cai, K. Zygourakis, A multiscale transient model for combustion of highly porous chars, Ind Eng Chem Res. 42 (2003) 2746–2755. https://doi.org/10.1021/ie0205391.

[82] F. Boso, I. Battiato, Homogenizability conditions for multicomponent reactive transport, Adv Water Resour. 62 (2013) 254–265. https://doi.org/https://doi.org/10.1016/j.advwatres.2013.07.014.

[83] E.M. Ryan, A.M. Tartakovsky, C. Amon, Pore-scale modeling of competitive adsorption in porous media., J Contam Hydrol. 120–121 (2011) 56–78. https://doi.org/10.1016/j.jconhyd.2010.06.008.

[84] M. Sahraoui, M. Kaviany, Direct simulation vs volume-averaged treatment of adiabatic, premixed flame in a porous medium, Int J Heat Mass Transf. 37 (1994) 2817–2834. https://doi.org/https://doi.org/10.1016/0017-9310(94)90338-7.

[85] Y. Du, C. Wang, D. Che, J.P. Mathews, The influence of char particle morphology on char burnout behavior by atomistic simulation, Fuel. 314 (2022) 123129. https://doi.org/10.1016/j.fuel.2022.123129.

[86] R. Jovanović, E. Marek, S. Maletić, D. Cvetinović, Z. Marković, Lattice Monte Carlo simulation of single coal char particle combustion under oxy–fuel conditions, Fuel. 151 (2015) 172–181. https://doi.org/https://doi.org/10.1016/j.fuel.2015.02.104.

[87] H. Xin, C. Wang, E. Louw, D. Wang, J.P. Mathews, Atomistic simulation of coal char isothermal oxy-fuel combustion: Char reactivity and behavior, Fuel. 182 (2016) 935–943. https://doi.org/https://doi.org/10.1016/j.fuel.2016.05.103.

[88] C. Wang, J.K. Watson, E. Louw, J.P. Mathews, Construction Strategy for Atomistic Models of Coal Chars Capturing Stacking Diversity and Pore Size Distribution, Energy and Fuels. 29 (2015) 4814–4826. https://doi.org/10.1021/acs.energyfuels.5b00816.

[89] A. Richter, P.A. Nikrityuk, B. Meyer, Three-dimensional calculation of a chemically reacting porous particle moving in a hot O2/CO2 atmosphere, Int J Heat Mass Transf. 83 (2015) 244–258. https://doi.org/10.1016/j.ijheatmasstransfer.2014.11.090.

[90] Z. Xue, Q. Guo, Y. Gong, J. Xu, G. Yu, Numerical study of a reacting single coal char particle with different pore structures moving in a hot O2/CO2 atmosphere, Fuel. 206 (2017) 381–389. https://doi.org/https://doi.org/10.1016/j.fuel.2017.06.035.

[91] K. Wittig, P.A. Nikrityuk, S. Schulze, A. Richter, Three-dimensional modeling of porosity development during the gasification of a char particle, AIChE Journal. 63 (2017) 1638–1647. https://doi.org/10.1002/aic.15526.

[92] K. Wittig, P.A. Nikrityuk, A. Richter, B. Meyer, Modelling of pore growth in char particles by an octree-based 3D PLIC method, AIP Conf Proc. 1648 (2015) 1–5. https://doi.org/10.1063/1.4912353.

[93] A.G. Dixon, M.E. Taskin, M. Nijemeisland, E.H. Stitt, CFD Method To Couple Three-Dimensional Transport and Reaction inside Catalyst Particles to the Fixed Bed Flow Field, Ind Eng Chem Res. 49 (2010) 9012–9025. https://doi.org/10.1021/ie100298q.

[94] M. Behnam, A.G. Dixon, M. Nijemeisland, E.H. Stitt, Catalyst deactivation in 3D CFD resolved particle simulations of propane dehydrogenation, Ind Eng Chem Res. 49 (2010) 10641–10650.

[95] P.N. Ciesielski, M.F. Crowley, M.R. Nimlos, A.W. Sanders, G.M. Wiggins, D. Robichaud, B.S. Donohoe, T.D. Foust, Biomass particle models with realistic morphology and resolved microstructure for simulations of intraparticle transport phenomena, Energy and Fuels. 29 (2015) 242–254. https://doi.org/10.1021/ef502204v.

[96] P.N. Ciesielski, M.B. Pecha, N.E. Thornburg, M.F. Crowley, X. Gao, O. Oyedeji, H. Sitaraman, N. Brunhart-Lupo, Bridging Scales in Bioenergy and Catalysis: A Review of Mesoscale Modeling Applications, Methods, and Future Directions, Energy and Fuels. 35 (2021) 14382–14440. https://doi.org/10.1021/acs.energyfuels.1c02163.

[97] M. Cloke, E. Lester, W. Gibb, Characterization of coal with respect to carbon burnout in p.f.-fired boilers, Fuel. 76 (1997) 1257–1267. https://doi.org/https://doi.org/10.1016/S0016-2361(97)00016-1.

[98] R. Gupta, Advanced coal characterization: A review, Energy and Fuels. 21 (2007) 451–460. https://doi.org/10.1021/ef060411m.

[99] D. Alvarez, A.G. Borrego, R. Menéndez, Unbiased methods for the morphological description of char structures, Fuel. 76 (1997) 1241–1248. https://doi.org/https://doi.org/10.1016/S0016-2361(97)00065-3.

[100] S. Jorgensen, S. Singer, Micro-CT-Based Approaches for Quantifying the Morphology of Pulverized Char Particles, Energy and Fuels. 33 (2019) 4826–4834. https://doi.org/10.1021/acs.energyfuels.9b00437.

[101] M. Cloke, T. Wu, R. Barranco, E. Lester, Char characterisation and its application in a coal burnout model☆, Fuel. 82 (2003) 1989–2000. https://doi.org/https://doi.org/10.1016/S0016-2361(03)00155-8.

[102] T. Wu, E. Lester, M. Cloke, A burnout prediction model based around char morphology, Energy and Fuels. 20 (2006) 1175–1183. https://doi.org/10.1021/ef050101o.

[103] L. Ma, R. Mitchell, Modeling char oxidation behavior under Zone II burning conditions at elevated pressures, Combust Flame. 156 (2009) 37–50. https://doi.org/10.1016/j.combustflame.2008.06.015.

[104] T. Wu, E. Lester, M. Cloke, Advanced Automated Char Image Analysis Techniques, Energy & Fuels. 20 (2006) 1211–1219. https://doi.org/10.1021/ef050360d.

[105] E. Lester, M. Cloke, M. Allen, Char characterization using image analysis techniques, Energy and Fuels. 10 (1996) 696–703. https://doi.org/10.1021/ef9501713.

[106] J. Perkins, O. Williams, T. Wu, E. Lester, Automated image analysis techniques to characterise pulverised coal particles and predict combustion char morphology, Fuel. 259 (2020) 116022. https://doi.org/10.1016/j.fuel.2019.116022.

[107] D. Chaves, E. Trucco, J. Barraza, M. Trujillo, An image processing system for char combustion reactivity characterisation, Comput Ind. 106 (2019) 60–70. https://doi.org/10.1016/j.compind.2018.12.014.

[108] J.G. Bailey, A. Tate, C.F.K. Diessel, T.F. Wall, A char morphology system with applications to coal combustion, Fuel. 69 (1990) 225–239. https://doi.org/10.1016/0016-2361(90)90179-T.

[109] E. Lester, D. Alvarez, A.G. Borrego, B. Valentim, D. Flores, D.A. Clift, P. Rosenberg, B. Kwiecinska, R. Barranco, H.I. Petersen, M. Mastalerz, K.S. Milenkova, C. Panaitescu, M.M. Marques, A. Thompson, D. Watts, S. Hanson, G. Predeanu, M. Misz, T. Wu, The procedure used to develop a coal char classification-Commission III Combustion Working Group of the International Committee for Coal and Organic Petrology, Int J Coal Geol. 81 (2010) 333–342. https://doi.org/10.1016/j.coal.2009.10.015.

[110] K.E. Benfell, G.S. Liu, D.G. Roberts, D.J. Harris, J.A. Lucas, J.G. Bailey, T.F. Wall, Modeling char combustion: The influence of parent coal petrography and pyrolysis pressure on the structure and intrinsic reactivity of its char, Proceedings of the Combustion Institute. 28 (2000) 2233–2241. https://doi.org/10.1016/s0082-0784(00)80633-5.

[111] A.G. Borrego, L. Garavaglia, W.D. Kalkreuth, Characteristics of high heating rate biomass chars prepared under N2 and CO2 atmospheres, Int J Coal Geol. 77 (2009) 409–415. https://doi.org/10.1016/j.coal.2008.06.004.

[112] C.H. Pang, E. Lester, T. Wu, Influence of lignocellulose and plant cell walls on biomass char morphology and combustion reactivity, Biomass Bioenergy. 119 (2018) 480–491. https://doi.org/10.1016/j.biombioe.2018.10.011.

[113] E. Lester, C. Avila, C.H. Pang, O. Williams, J. Perkins, S. Gaddipatti, G. Tucker, J.M. Barraza, M.P. Trujillo-Uribe, T. Wu, A proposed biomass char classification system, Fuel. 232 (2018) 845–854. https://doi.org/10.1016/j.fuel.2018.05.153.

[114] A. Panahi, N. Vorobiev, M. Schiemann, M. Tarakcioglu, M. Delichatsios, Y.A. Levendis, Combustion details of raw and torrefied biomass fuel particles with individually-observed size, shape and mass, Combust Flame. 207 (2019) 327–341. https://doi.org/10.1016/j.combustflame.2019.06.009.

[115] H. Watanabe, X-ray Computed Tomography Visualization of the Woody Char Intraparticle Pore Structure and Its Role on Anisotropic Evolution during Char Gasification, Energy and Fuels. 32 (2018) 4248–4254. https://doi.org/10.1021/acs.energyfuels.7b03227.

[116] J.P. Mathews, Q.P. Campbell, H. Xu, P. Halleck, A review of the application of X-ray computed tomography to the study of coal, Fuel. 209 (2017) 10–24. https://doi.org/10.1016/j.fuel.2017.07.079.

[117] J. Han, W. Liu, S. Wang, D. Du, F. Xu, W. Li, G. de Schutter, Effects of crack and ITZ and aggregate on carbonation penetration based on 3D micro X-ray CT microstructure evolution, Constr Build Mater. 128 (2016) 256–271. https://doi.org/10.1016/j.conbuildmat.2016.10.062.

[118] A. Golab, C.R. Ward, A. Permana, P. Lennox, P. Botha, High-resolution three-dimensional imaging of coal using microfocus X-ray computed tomography, with special reference to modes of mineral occurrence, Int J Coal Geol. 113 (2013) 97–108. https://doi.org/10.1016/j.coal.2012.04.011.

[119] N. Sarunac, E.K. Levy, M. Ness, C.W. Bullinger, J.P. Mathews, P.M. Halleck, A novel fluidized bed drying and density segregation process for upgrading low-rank coals, International Journal of Coal Preparation and Utilization. 29 (2009) 317–332. https://doi.org/10.1080/19392691003666387.

[120] S. Coetzee, H.W.J.P. Neomagus, J.R. Bunt, C.A. Strydom, H.H. Schobert, The transient swelling behaviour of large (-20 + 16 mm) South African coal particles during low-temperature devolatilisation, Fuel. 136 (2014) 79–88. https://doi.org/10.1016/j.fuel.2014.07.021.

[121] C.Ö. Karacan, G.D. Mitchell, Behavior and effect of different coal microlithotypes during gas transport for carbon dioxide sequestration into coal seams, Int J Coal Geol. 53 (2003) 201–217. https://doi.org/10.1016/S0166-5162(03)00030-2.

[122] D. Liang, S. Singer, Pore-resolving simulations to study the impacts of char morphology on zone II combustion and effectiveness factor models, Combust Flame. 229 (2021) 111405. https://doi.org/https://doi.org/10.1016/j.combustflame.2021.111405.

[123] E. Boigné, N.R. Bennett, A. Wang, K. Mohri, M. Ihme, Simultaneous in-situ measurements of gas temperature and pyrolysis of biomass smoldering via X-ray computed tomography, Proceedings of the Combustion Institute. 38 (2021) 3899–3907. https://doi.org/10.1016/j.proci.2020.06.070.

[124] E. Boigné, N.R. Bennett, A. Wang, M. Ihme, Structural analysis of biomass pyrolysis and oxidation using in-situ X-ray computed tomography, Combust Flame. 235 (2022). https://doi.org/10.1016/j.combustflame.2021.111737.

[125] X. Ni, J. Miao, R. Lv, X. Lin, Quantitative 3D spatial characterization and flow simulation of coal macropores based on MCT technology, Fuel. 200 (2017) 199–207. https://doi.org/10.1016/j.fuel.2017.03.068.

[126] S. Hjärtstam, K. Andersson, F. Johnsson, B. Leckner, Combustion characteristics of lignite-fired oxy-fuel flames, Fuel. 88 (2009) 2216–2224. https://doi.org/https://doi.org/10.1016/j.fuel.2009.05.011.

[127] A. Fluent, Ansys Fluent 12.0 Theory Guide, ANSYS Inc., Canonsburg, PA. (2009).

[128] S. Singer, L. Chen, A.F. Ghoniem, The influence of gasification reactions on char consumption under oxy-combustion conditions: Effects of particle trajectory and conversion, Proceedings of the Combustion Institute. 34 (2013) 3471–3478. https://doi.org/10.1016/j.proci.2012.07.042.

[129] D.J. Harris, I.W. Smith, Intrinsic reactivity of petroleum coke and brown coal char to carbon dioxide, steam and oxygen, Symposium (International) on Combustion. 23 (1991) 1185–1190. https://doi.org/https://doi.org/10.1016/S0082-0784(06)80379-6.

[130] C. di Blasi, Combustion and gasification rates of lignocellulosic chars, Prog Energy Combust Sci. 35 (2009) 121–140. https://doi.org/10.1016/j.pecs.2008.08.001.

[131] R.C. Reid, J.M. Prausnitz, B.E. Poling, The properties of gases and liquids, (1987).

[132] K.B. Bischoff, Accuracy of the pseudo steady state approximation for moving boundary diffusion problems, Chem Eng Sci. 18 (1963) 711–713.

[133] D. Luss, On the pseudo steady state approximation for gas solid reactions, Can J Chem Eng. 46 (1968) 154–156.

[134] E. Boigné, N.R. Bennett, A. Wang, K. Mohri, M. Ihme, Simultaneous in-situ measurements of gas temperature and pyrolysis of biomass smoldering via X-ray computed tomography, Proceedings of the Combustion Institute. 38 (2021) 3899–3907. https://doi.org/10.1016/j.proci.2020.06.070.

[135] E. Boigné, N.R. Bennett, A. Wang, M. Ihme, Structural analysis of biomass pyrolysis and oxidation using in-situ X-ray computed tomography, Combust Flame. 235 (2022) 111737. https://doi.org/10.1016/j.combustflame.2021.111737.

[136] P.N. Ciesielski, M.B. Pecha, A.M. Lattanzi, V.S. Bharadwaj, M.F. Crowley, L. Bu, J. v. Vermaas, K.X. Steirer, M.F. Crowley, Advances in Multiscale Modeling of Lignocellulosic Biomass, ACS Sustain Chem Eng. 8 (2020) 3512–3531. https://doi.org/10.1021/acssuschemeng.9b07415.

[137] E.W. Thiele, Relation between Catalytic Activity and Size of Particle, Ind Eng Chem. 31 (1939) 916–920. https://doi.org/10.1021/ie50355a027.

[138] J.B. Wang, A. Varma, Effectiveness factors for pellet with step-distribution of catalyst, Chem Eng Sci. 33 (1978) 1549–1552. https://doi.org/https://doi.org/10.1016/0009-2509(78)85207-5.

[139] B.A. Buffham, Design relations for hollow catalyst pellets, Chemical Engineering Research and Design. 78 (2000) 269–282. https://doi.org/10.1205/026387600527130.

[140] C. Mocciaro, N.J. Mariani, O.M. Martínez, G.F. Barreto, A three-parameter one-dimensional model to predict the effectiveness factor for an arbitrary pellet shape, Ind Eng Chem Res. 50 (2011) 2746–2754. https://doi.org/10.1021/ie101296d.

[141] R. Aris, Communication. Normalization for the Thiele Modulus, Industrial & Engineering Chemistry Fundamentals. 4 (1965) 227–229. https://doi.org/10.1021/i160014a024.

[142] S.D. Keegan, N.J. Mariani, O.M. Martínez, G.F. Barreto, Behavior of catalytic pellets at high reaction rates. The effect of edges, Ind Eng Chem Res. 45 (2006) 85–97. https://doi.org/10.1021/ie050740m.

[143] M. Asif, Efficient expressions for effectiveness factor for a finite cylinder, Chemical Engineering Research and Design. 82 (2004) 605–610. https://doi.org/10.1205/026387604323142658.

[144] D.J. Gunn, Diffusion and chemical reaction in catalysis and absorption, Chem Eng Sci. 22 (1967) 1439–1455.

[145] D. Chaves, E. Trucco, J. Barraza, M. Trujillo, An image processing system for char combustion reactivity characterisation, Comput Ind. 106 (2019) 60–70. https://doi.org/https://doi.org/10.1016/j.compind.2018.12.014.

[146] T.M. Mitchell, Machine learning, (1997).

[147] B.P. Woolf, Building intelligent interactive tutors: Student-centered strategies for revolutionizing e-learning, Morgan Kaufmann, 2010.

[148] S. Ascher, I. Watson, S. You, Machine learning methods for modelling the gasification and pyrolysis of biomass and waste, Renewable and Sustainable Energy Reviews. 155 (2022). https://doi.org/10.1016/j.rser.2021.111902.

[149] V. Vapnik, The nature of statistical learning theory, Springer science & business media, 1999.

[150] T. Hastie, R. Tibshirani, G. James, D. Witten, An Introduction to Statistical Learning, Springer Texts, 2006.

[151] H. Sun, G. Lv, J. Mo, X. Lv, G. Du, Y. Liu, Application of KPCA combined with SVM in Raman spectral discrimination, Optik (Stuttg). 184 (2019) 214–219. https://doi.org/10.1016/j.ijleo.2019.02.126.

[152] L. Breiman, Random forests, Mach Learn. 45 (2001) 5–32.

[153] J. Luan, C. Zhang, B. Xu, Y. Xue, Y. Ren, The predictive performances of random forest models with limited sample size and different species traits, Fish Res. 227 (2020) 105534. https://doi.org/10.1016/j.fishres.2020.105534.

[154] M. Meng, C. Zhao, Application of Support Vector Machines to a Small-Sample Prediction, Advances in Petroleum Exploration and Development. 10 (2015) 72–75. https://doi.org/10.3968/7830.

[155] A. Calvelo, R.E. Cunningham, Overall effectiveness factor for gas-solid reactions, J Catal. 16 (1970) 397–403. https://doi.org/https://doi.org/10.1016/0021-9517(70)90238-1.

[156] G.S. Liu, S. Niksa, Coal conversion submodels for design applications at elevated pressures. Part II. Char gasification, Prog Energy Combust Sci. 30 (2004) 679–717. https://doi.org/10.1016/j.pecs.2004.08.001.

[157] U. Kleinhans, S. Halama, H. Spliethoff, The role of gasification reactions during pulverized solid fuel combustion: A detailed char combustion model based on measurements of char structure and kinetics for coal and pre-treated biomass, Combust Flame. 184 (2017) 117–135. https://doi.org/https://doi.org/10.1016/j.combustflame.2017.05.033.

[158] S. Samarasinghe, Neural networks for applied sciences and engineering: from fundamentals to complex pattern recognition, Auerbach publications, 2016.

[159] R. Kohavi, G.H. John, Wrappers for feature subset selection, Artif Intell. 97 (1997) 273–324. https://doi.org/https://doi.org/10.1016/S0004-3702(97)00043-X.

[160] B.W. Matthews, Comparison of the predicted and observed secondary structure of T4 phage lysozyme, Biochimica et Biophysica Acta (BBA) - Protein Structure. 405 (1975) 442–451. https://doi.org/https://doi.org/10.1016/0005-2795(75)90109-9.

[161] X. Zhu, C. Vondrick, C.C. Fowlkes, D. Ramanan, Do We Need More Training Data?, Int J Comput Vis. 119 (2016) 76–92. https://doi.org/10.1007/s11263-015-0812-2.

[162] G. Wang, J. Shen, S. Liu, C. Jiang, X. Qin, Three-dimensional modeling and analysis of macro-pore structure of coal using combined X-ray CT imaging and fractal theory, International Journal of Rock Mechanics and Mining Sciences. 123 (2019) 104082. https://doi.org/10.1016/j.ijrmms.2019.104082.

[163] X. Wang, J. Pan, K. Wang, T. Ge, J. Wei, W. Wu, Characterizing the shape, size, and distribution heterogeneity of pore-fractures in high rank coal based on X-ray CT image analysis and mercury intrusion porosimetry, Fuel. 282 (2020) 118754. https://doi.org/10.1016/j.fuel.2020.118754.

[164] Q. Sun, Y. Xia, J. Klinger, R. Seifert, J. Kane, V. Thompson, Q. Chen, X-ray computed tomography-based porosity analysis: Algorithms and application for porous woody biomass, Powder Technol. 388 (2021) 496–504. https://doi.org/10.1016/j.powtec.2021.05.006.

[165] L. Tlig, M. Sayadi, F. Fnaiech, A new fuzzy segmentation approach based on S-FCM type 2 using LBP-GCO features, Signal Process Image Commun. 27 (2012) 694–708. https://doi.org/https://doi.org/10.1016/j.image.2012.03.001.

[166] D. Mart, ANALYSIS OF IMAGE THRESHOLDING METHODS FOR THEIR APPLICATION TO AUGMENTED REALITY ENVIRONMENTS Autorización de difusión, (2012) 1–63. https://eprints.ucm.es/16932/1/Tesis_Master_Daniel_Martin_Carabias.pdf.

[167] D. Gómez, J. Yáñez, C. Guada, J.T. Rodríguez, J. Montero, E. Zarrazola, Fuzzy image segmentation based upon hierarchical clustering, Knowl Based Syst. 87 (2015) 26–37.

[168] S. Dai, K. Lu, J. Dong, Y. Zhang, Y. Chen, A novel approach of lung segmentation on chest CT images using graph cuts, Neurocomputing. 168 (2015) 799–807.

[169] R. Jin, J. Yin, W. Zhou, J. Yang, Level set segmentation algorithm for high-resolution polarimetric SAR images based on a heterogeneous clutter model, IEEE J Sel Top Appl Earth Obs Remote Sens. 10 (2017) 4565–4579.

[170] Z. Wang, B. Ma, Y. Zhu, Review of Level Set in Image Segmentation, Archives of Computational Methods in Engineering. 28 (2021) 2429–2446. https://doi.org/10.1007/s11831-020-09463-9.

[171] K. Zuiderveld, Contrast Limited Adaptive Histogram Equalization, Graphics Gems. IV (1994) 474–485.

[172] C.A. Schneider, W.S. Rasband, K.W. Eliceiri, NIH Image to ImageJ: 25 years of image analysis, Nat Methods. 9 (2012) 671–675.

[173] P. Sthitpattanapongsa, T. Srinark, An equivalent 3d otsu's thresholding method, in: Pacific-Rim Symposium on Image and Video Technology, Springer, 2011: pp. 358–369.

[174] N. Zhu, G. Wang, G. Yang, W. Dai, A fast 2D otsu thresholding algorithm based on improved histogram, Proceedings of the 2009 Chinese Conference on Pattern Recognition, CCPR 2009, and the 1st CJK Joint Workshop on Pattern Recognition, CJKPR. (2009) 319–323. https://doi.org/10.1109/CCPR.2009.5344078.

[175] T.F. Chan, L.A. Vese, Active contours without edges, IEEE Transactions on Image Processing. 10 (2001) 266–277. https://doi.org/10.1109/83.902291.

[176] C. Li, C. Xu, C. Gui, M.D. Fox, Distance regularized level set evolution and its application to image segmentation, IEEE Transactions on Image Processing. 19 (2010) 3243–3254.

[177] H. Min, W. Jia, Y. Zhao, W. Zuo, H. Ling, Y. Luo, LATE: A level-set method based on local approximation of Taylor expansion for segmenting intensity inhomogeneous images, IEEE Transactions on Image Processing. 27 (2018) 5016–5031.

[178] G. Lehmann, D. Legland, Efficient N-dimensional surface estimation using Crofton formula and run-length encoding, Efficient N-Dimensional Surface Estimation Using Crofton Formula and Run-Length Encoding. (2012).

Appendix: Supplementary Material

Coal char particles:

Table S1 Measured morphological parameters from volume and surface integration of 3-D geometries obtained from micro-CT imaging.

Particle	V_{mps} (m^3)	$S_{mps,interface}$ (m^2)	$S_{ext,void}$ (m^2)	$S_{ext,total}$ (m^2)	EVF
1	4.25E-13	4.93E-08	0.00E+00	3.77E-08	0.0000
2	4.28E-13	5.19E-08	0.00E+00	3.98E-08	0.0000
3	4.01E-13	5.53E-08	0.00E+00	3.85E-08	0.0000
4	4.09E-13	5.05E-08	0.00E+00	3.94E-08	0.0000
5	2.59E-13	5.33E-08	0.00E+00	3.31E-08	0.0000
6	4.03E-13	5.27E-08	8.61E-12	3.56E-08	0.0002
7	4.40E-13	5.77E-08	7.66E-11	3.51E-08	0.0022
8	4.03E-13	5.73E-08	1.42E-10	3.67E-08	0.0039
9	4.72E-13	4.74E-08	2.52E-10	3.96E-08	0.0064
10	3.00E-13	5.64E-08	2.55E-10	3.73E-08	0.0068
11	2.27E-13	6.07E-08	2.65E-10	3.50E-08	0.0076
12	2.67E-13	5.96E-08	2.74E-10	3.37E-08	0.0081
13	3.42E-13	5.13E-08	3.36E-10	3.62E-08	0.0093
14	2.74E-13	5.65E-08	3.40E-10	3.59E-08	0.0095
15	3.34E-13	5.41E-08	3.74E-10	3.70E-08	0.0101
16	3.89E-13	4.82E-08	3.90E-10	3.48E-08	0.0112
17	4.03E-13	5.06E-08	4.68E-10	3.83E-08	0.0122
18	2.58E-13	5.96E-08	4.68E-10	3.65E-08	0.0128
19	2.86E-13	5.60E-08	5.26E-10	3.68E-08	0.0143
20	3.87E-13	5.30E-08	6.11E-10	4.06E-08	0.0151
21	2.06E-13	5.59E-08	5.39E-10	3.31E-08	0.0163
22	4.55E-13	5.19E-08	6.85E-10	4.00E-08	0.0171
23	2.26E-13	5.59E-08	5.97E-10	3.33E-08	0.0179
24	3.43E-13	4.98E-08	6.31E-10	3.50E-08	0.0180
25	3.08E-13	5.34E-08	6.54E-10	3.61E-08	0.0181
26	2.62E-13	5.50E-08	7.34E-10	3.43E-08	0.0214
27	2.79E-13	5.44E-08	8.47E-10	3.77E-08	0.0225
28	3.09E-13	5.57E-08	8.92E-10	3.84E-08	0.0233
29	4.61E-13	4.90E-08	1.07E-09	3.81E-08	0.0280
30	3.12E-13	6.32E-08	1.06E-09	3.70E-08	0.0286
31	2.85E-13	5.52E-08	1.08E-09	3.54E-08	0.0304
32	3.55E-13	6.07E-08	1.23E-09	4.02E-08	0.0306
33	3.07E-13	5.92E-08	1.07E-09	3.44E-08	0.0311

34	3.15E-13	5.80E-08	1.30E-09	3.76E-08	0.0345
35	2.18E-13	5.65E-08	1.23E-09	3.56E-08	0.0346
36	2.43E-13	5.82E-08	1.76E-09	3.91E-08	0.0450
37	3.48E-13	6.95E-08	1.81E-09	3.61E-08	0.0502
38	2.94E-13	5.22E-08	1.75E-09	3.45E-08	0.0507
39	3.35E-13	5.71E-08	2.01E-09	3.74E-08	0.0539
40	3.21E-13	5.60E-08	1.87E-09	3.47E-08	0.0540
41	2.68E-13	6.71E-08	2.08E-09	3.80E-08	0.0546
42	3.62E-13	5.98E-08	2.13E-09	3.91E-08	0.0546
43	2.49E-13	6.31E-08	2.72E-09	3.74E-08	0.0727
44	2.14E-13	5.74E-08	2.92E-09	3.31E-08	0.0881
45	2.88E-13	5.84E-08	3.47E-09	3.74E-08	0.0929
46	3.39E-13	5.61E-08	3.76E-09	3.72E-08	0.1010
47	2.80E-13	6.05E-08	3.59E-09	3.54E-08	0.1016
48	3.24E-13	6.55E-08	4.09E-09	3.55E-08	0.1153
49	3.63E-13	6.50E-08	4.87E-09	3.76E-08	0.1294
50	2.94E-13	6.60E-08	5.41E-09	4.04E-08	0.1340

Table S2 Derived morphological parameters used in the flat plate, hollow sphere, 1D-GC and 1D-VD effectiveness factor models.

No.	L (μm)	θ_{void}	R_{in} (μm)	l (μm)	σ (low φ)	γ	σ (high φ)	Γ	β
1	21.37	0.1877	28.63	8.61	0.3066	0.3951	0.1229	0.1094	0.2087
2	21.32	0.1887	28.68	8.25	0.4234	0.4158	0.1176	0.1052	0.2403
3	19.18	0.2341	30.82	7.25	0.5975	0.4441	0.0040	0.0039	0.2936
4	19.16	0.2347	30.84	8.09	1.6563	0.5705	0.1137	0.1021	0.5888
5	10.16	0.5060	39.84	4.86	0.4581	0.4216	0.0278	0.0270	0.2804
6	19.34	0.2306	30.66	7.65	0.4583	0.4217	0.0196	0.0192	0.2502
7	21.85	0.1785	28.15	7.62	0.2079	0.3765	-0.1801	-0.2197	0.1996
8	18.63	0.2469	31.37	7.04	0.9212	0.4899	-0.0538	-0.0569	0.4136
9	25.40	0.1191	24.60	9.97	2.1660	0.6129	0.1425	0.1247	0.6438

10	12.50	0.4220	37.50	5.32	1.3005	0.5349	0.0499	0.0475	0.5222
11	8.72	0.5629	41.28	3.73	0.3925	0.4105	0.0586	0.0553	0.2633
12	10.68	0.4863	39.32	4.48	0.5813	0.4415	-0.0003	-0.0003	0.3024
13	14.91	0.3455	35.09	6.66	0.3778	0.4079	0.0870	0.0800	0.2363
14	11.19	0.4678	38.81	4.86	0.4745	0.4244	0.0362	0.0349	0.2629
15	14.43	0.3600	35.57	6.17	0.2027	0.3755	0.0739	0.0688	0.1824
16	18.30	0.2548	31.70	8.06	0.2626	0.3870	0.1104	0.0994	0.1979
17	19.54	0.2260	30.46	7.96	0.2542	0.3854	0.1032	0.0936	0.1947
18	10.35	0.4985	39.65	4.33	0.8395	0.4791	0.0090	0.0089	0.3931
19	12.41	0.4248	37.59	5.11	1.0865	0.5106	0.0889	0.0816	0.4430
20	18.19	0.2576	31.81	7.31	0.6049	0.4452	0.0940	0.0859	0.2995
21	7.76	0.6030	42.24	3.69	0.3442	0.4020	0.0335	0.0324	0.2388
22	24.55	0.1318	25.45	8.76	0.7163	0.4618	0.0667	0.0625	0.3110
23	8.67	0.5650	41.33	4.04	1.0925	0.5113	0.0353	0.0341	0.5479
24	15.05	0.3415	34.95	6.88	0.3269	0.3988	0.1118	0.1006	0.2188
25	13.59	0.3862	36.41	5.78	0.7747	0.4702	0.1384	0.1215	0.3384
26	10.30	0.5006	39.70	4.76	0.5060	0.4295	0.0343	0.0332	0.2887
27	11.62	0.4524	38.38	5.12	1.1474	0.5178	0.0801	0.0741	0.5177
28	13.18	0.3992	36.82	5.54	0.7485	0.4665	0.0504	0.0480	0.3443
29	25.07	0.1240	24.93	9.41	0.5624	0.4386	0.0865	0.0796	0.2742
30	13.08	0.4025	36.92	4.93	0.6279	0.4487	0.0233	0.0227	0.3237
31	11.88	0.4430	38.12	5.17	0.6850	0.4573	0.0409	0.0393	0.3305
32	15.58	0.3261	34.42	5.85	1.2061	0.5245	0.0337	0.0326	0.4562

33	14.51	0.3576	35.49	5.19	1.9846	0.5988	0.0388	0.0374	0.5988
34	13.35	0.3937	36.65	5.43	0.6384	0.4503	0.0381	0.0367	0.3108
35	8.62	0.5669	41.38	3.86	0.7609	0.4682	0.0731	0.0681	0.3727
36	9.58	0.5282	40.42	4.18	0.7138	0.4615	0.0436	0.0417	0.3761
37	15.58	0.3263	34.42	5.01	3.0464	0.6692	0.0259	0.0252	0.6851
38	12.38	0.4258	37.62	5.63	0.7134	0.4614	0.1036	0.0939	0.3287
39	14.77	0.3498	35.23	5.87	0.9909	0.4989	0.0549	0.0521	0.3970
40	14.00	0.3732	36.00	5.74	0.8777	0.4842	0.0598	0.0564	0.3716
41	11.25	0.4655	38.75	3.99	1.0678	0.5083	0.0890	0.0817	0.4302
42	16.43	0.3027	33.57	6.05	0.6576	0.4532	0.0190	0.0187	0.3145
43	10.34	0.4992	39.66	3.95	1.0504	0.5062	0.0939	0.0858	0.4422
44	8.41	0.5754	41.59	3.72	2.1313	0.6102	0.1213	0.1082	0.7841
45	11.83	0.4450	38.17	4.93	1.0145	0.5018	0.0534	0.0507	0.4445
46	14.97	0.3437	35.03	6.05	1.0711	0.5087	0.1677	0.1436	0.4082
47	11.69	0.4499	38.31	4.62	1.2371	0.5280	0.0892	0.0819	0.4733
48	13.87	0.3772	36.13	4.94	1.1559	0.5188	0.0907	0.0832	0.4504
49	16.34	0.3051	33.66	5.58	3.1157	0.6730	0.0498	0.0474	0.8743
50	12.82	0.4111	37.18	4.45	1.5887	0.5641	0.0600	0.0566	0.4958

Biomass char particles

Table S3 Measured morphological parameters from volume and surface integration of 3-D geometries obtained from micro-CT imaging and from bounding box measurements.

No.	V_{mps} (m^3)	θ_{void}	$S_{mps,interface}$ (m^2)	$S_{ext,void}$ (m^2)	$S_{ext,total}$ (m^2)	EVF	β

1	4.74E-13	0.0945	1.26E-08	2.25E-10	5.16E-08	0.0044	7.3755
2	4.35E-13	0.1698	2.07E-08	5.00E-10	5.38E-08	0.0093	13.6144
3	4.91E-13	0.0631	9.32E-09	5.31E-10	5.01E-08	0.0106	3.1631
4	4.82E-13	0.0801	9.00E-09	1.37E-09	4.85E-08	0.0283	5.9731
5	4.51E-13	0.1389	1.37E-08	1.52E-09	5.21E-08	0.0292	8.2942
6	4.73E-13	0.0976	1.04E-08	1.69E-09	5.42E-08	0.0313	6.3648
7	4.76E-13	0.0915	1.39E-08	2.04E-09	5.67E-08	0.0360	8.9806
8	4.64E-13	0.1141	1.41E-08	2.00E-09	4.99E-08	0.0402	8.2517
9	4.46E-13	0.1488	1.50E-08	2.17E-09	5.26E-08	0.0413	6.6916
10	4.36E-13	0.1672	1.85E-08	2.10E-09	4.78E-08	0.0440	5.6761
11	4.84E-13	0.0751	1.26E-08	2.21E-09	4.95E-08	0.0446	4.5565
12	4.07E-13	0.2230	1.87E-08	1.95E-09	4.22E-08	0.0461	4.4279
13	4.69E-13	0.1042	1.39E-08	3.19E-09	5.96E-08	0.0535	5.9491
14	4.28E-13	0.1829	1.74E-08	3.13E-09	5.73E-08	0.0546	7.1461
15	4.43E-13	0.1534	1.48E-08	2.74E-09	4.98E-08	0.0550	4.8395
16	4.19E-13	0.2003	2.34E-08	2.65E-09	4.64E-08	0.0571	5.3428
17	4.43E-13	0.1530	1.66E-08	3.38E-09	5.53E-08	0.0611	6.8096
18	4.74E-13	0.0951	1.16E-08	3.07E-09	4.90E-08	0.0627	5.0458
19	4.56E-13	0.1290	1.74E-08	3.56E-09	5.65E-08	0.0631	7.1052
20	4.46E-13	0.1490	1.45E-08	3.20E-09	4.97E-08	0.0643	4.9269
21	4.34E-13	0.1703	1.61E-08	4.10E-09	5.93E-08	0.0691	5.9109
22	4.45E-13	0.1500	2.07E-08	4.01E-09	5.21E-08	0.0769	6.0298
23	3.97E-13	0.2424	1.79E-08	3.64E-09	4.48E-08	0.0814	5.6105

24	4.36E-13	0.1667	1.74E-08	4.24E-09	4.71E-08	0.0899	5.5613
25	4.16E-13	0.2062	2.23E-08	5.52E-09	5.09E-08	0.1086	4.2939
26	4.02E-13	0.2318	2.32E-08	7.61E-09	6.86E-08	0.1109	6.8528
27	4.23E-13	0.1926	1.99E-08	6.44E-09	5.69E-08	0.1132	6.8855
28	4.01E-13	0.2337	1.92E-08	7.17E-09	5.63E-08	0.1273	5.8814
29	4.16E-13	0.2046	1.93E-08	9.19E-09	6.13E-08	0.1500	5.1509
30	3.79E-13	0.2752	2.84E-08	8.52E-09	5.20E-08	0.1639	4.6730

Table S4 Derived geometrical parameters used in the UFC, UIC, AHFC, AHIC, and IHIC effectiveness factor models.

Particle	*L* (μm)	R_{in} (μm)	R, R_{out} (μm)
1	208.57	8.69	28.28
2	313.85	9.50	23.05
3	118.61	9.42	37.50
4	181.21	8.59	30.34
5	225.55	10.14	27.19
6	189.05	9.28	29.70
7	237.83	8.01	26.48
8	224.78	9.20	27.24
9	195.47	11.27	29.21
10	175.16	12.62	30.86
11	151.29	9.10	33.20
12	148.43	15.83	33.52
13	180.73	9.81	30.38
14	204.22	12.22	28.58
15	157.49	12.74	32.54
16	168.23	14.09	31.49
17	197.76	11.36	29.04
18	161.94	9.90	32.09
19	203.44	10.28	28.63
20	159.38	12.49	32.35
21	179.95	12.56	30.44
22	182.36	11.71	30.24
23	173.80	15.25	30.98

24	172.79	12.69	31.07
25	145.42	15.38	33.87
26	198.60	13.95	28.98
27	199.23	12.70	28.93
28	179.36	14.74	30.50
29	164.18	14.42	31.87
30	153.86	17.27	32.93